



저작자표시-비영리-변경금지 2.0 대한민국

이용자는 아래의 조건을 따르는 경우에 한하여 자유롭게

- 이 저작물을 복제, 배포, 전송, 전시, 공연 및 방송할 수 있습니다.

다음과 같은 조건을 따라야 합니다:



저작자표시. 귀하는 원저작자를 표시하여야 합니다.



비영리. 귀하는 이 저작물을 영리 목적으로 이용할 수 없습니다.



변경금지. 귀하는 이 저작물을 개작, 변형 또는 가공할 수 없습니다.

- 귀하는, 이 저작물의 재이용이나 배포의 경우, 이 저작물에 적용된 이용허락조건을 명확하게 나타내어야 합니다.
- 저작권자로부터 별도의 허가를 받으면 이러한 조건들은 적용되지 않습니다.

저작권법에 따른 이용자의 권리는 위의 내용에 의하여 영향을 받지 않습니다.

이것은 [이용허락규약\(Legal Code\)](#)을 이해하기 쉽게 요약한 것입니다.

[Disclaimer](#)

공학박사학위논문

Structural Design of
Transition Metal Compounds based
Electrocatalysts for Water Splitting

물분해 적용을 위한 전이 금속 화합물 기반
전기 촉매의 구조 설계에 관한 연구

2020년 8월

서울대학교 대학원

재료공학부

안 인 경

ABSTRACT

Structural Design of Transition Metal Compounds based Electrocatalysts for Water Splitting

In-Kyoung Ahn

Department of Materials Science and Engineering

The Graduate School

Seoul National University

The earth-abundant transition metal based compounds have been intensively investigated as one of the most promising electrode of electrochemical catalyst and device systems, e.g., water splitting, carbon dioxide reduction, nitrogen reduction, Li air batteries, and electrochemical capacitors, due to their low-cost and affordable electrochemical performance, compared with noble metals. However, transition metal compounds based electrocatalysts still require further improvement of their catalytic performances for large-scale application. In particular, the oxygen evolution reaction (OER) is the main key in water splitting system for hydrogen energy production, although it is currently obstructed by the sluggish kinetic of OER compared with hydrogen evolution reaction (HER). Limited charge transport of transition metal compounds based electrocatalysts under water oxidation conditions leads to a relatively inefficient OER performances. In addition, catalytic performance is highly dependent on controlling the exposure or modification of the active sites.

The objective of this thesis is thermodynamically optimal transition metal compounds based electrocatalysts of highly efficient water splitting and to provide guidelines for

electrocatalysts design with the respect to the precisely controlled phase and structure of catalysts.

First, nanostructured designed nickel iron layered double hydroxide (NiFe LDH) electrocatalysts for water oxidation were developed using hydrothermal method followed by gaseous boronization for boron doping and by thermodynamically programmed electrochemical oxidation to enhance OER performance. The purpose of boron doping in NiFe LDH is catalytic activity to overcome the relatively poor charge transfer and intrinsic conductivity of NiFe LDH that result in a low potential of commercialization. Until now, the boronization about boron doping or formation of borides has been limited to the high boiling point of boron, which has resulted in high temperature for boronization. The gaseous boronization with boron source, boron precursor not boron, make it easy to obtain the boron doped NiFe LDH at relatively low temperature to could be reached high OER performance due to improved charge transfer resistance. Furthermore, the activated boron doped NiFe LDH was successfully synthesized through its electrochemical oxidation, which consisted of the surface of boron doped NiFe LDH converted to oxyhydroxide. The boron doped NiFe LDH with electrochemical oxidation brings the improvement of the active site due to the doped boron species as the activation, electrochemical oxidation, step. The electrochemical oxidized boron doped NiFe LDH required an excellent OER performance 229 mV to reach 10 mA cm^{-2} of current density, which confirmed that it was approximately 140 mV lower than Ir, noble metal, and about 86 mV lower than pristine NiFe LDH under the same conditions.

The second focus is to control the phase in cobalt sulfide, e.g., Co, Co_9S_8 , and CoS_2 , and to develop hierarchically porous structure of electrocatalyst for efficient overall water splitting, which contains evolution reaction in both electrodes, OER and HER.

While cobalt sulfides have various phase, it was successfully controlled cobalt sulfide phase according to the sulfur ratio through predicted synthesis based on thermodynamic. A highly porous CoS₂ nanoparticles for exposure of active sites was directly synthesized by controlling the ratio of sulfur and cobalt Prussian blue analogues (Co₃[Co(CN)₆]₂), one of the metal organic frameworks (MOFs). The newly-designed MOF-driven CoS₂ electrocatalysts show high catalytic activity in HER, OER, and overall water splitting and the CoS₂ in this work shows a highly porous and uniform particle size. The synthesized MOF-driven CoS₂ has approximately 30 nm with ~ 4 nm pores, resulting in a large surface area of 915.6 m² g⁻¹. The synthesized catalysts achieved a catalytic current density of 10 mA cm⁻² at overpotential as low as 300, -200 mV from OER, HER, respectively. Furthermore, it has outstanding long-term stability at 10 mA cm⁻² despite of vigorously evolved gas. These excellent activity leads to outstanding performance of full-cell system of overall water splitting for a practical two-electrode system, which exhibited an overpotential of 1.65 V at 10 mA cm⁻².

This study could provide useful information for understanding the methodology to thermodynamically precisely control the phase and structure of transition metal compound and suggested versatile design that how to enhance the performance of transition metal compound based electrocatalysts for water splitting.

Keywords: water splitting, transition metal compounds, nickel iron layered double hydroxides, metal-organic frameworks, cobalt sulfide, thermodynamic calculation, phase control

Student Number: 2014-22522

Table of Contents

Abstract.....	i
Table of Contents.....	iv
List of Tables.....	viii
List of Figures.....	ix

Chapter 1. Introduction

1.1. Materials for electrocatalysts of water splitting	1
1.2. Charge transfer and phase issues in water splitting catalyst	7
1.2.1. NiFe LDH based electrocatalysts for water oxidation	7
1.2.2. CoS ₂ based electrocatalysts for overall water splitting	13
1.3. Objective of the thesis	17
1.4. Organization of the thesis	21

Chapter 2. Theoretical Background

2.1. Fundamentals of electrochemical water splitting	22
2.1.1. Thermodynamics of water splitting reactions	22
2.1.2. Electrocatalytic kinetics and related parameters	26
2.1.3. Charge and mass transfer	37
2.2. Electrochemical oxygen evolution reaction (OER)	39

2.2.1. Theory of electrochemical OER	41
2.2.2. Summary of OER electrocatalysts and performances	47
2.3. Electrochemical hydrogen evolution reaction (HER)	53
2.3.1. Theory of electrochemical HER	54
2.3.2. Summary of HER electrocatalysts and performances	57
2.4. Electrochemical oxidation methods	60
2.4.1. Cyclic voltammetry method	61
2.4.2. Galvanostatic method	62
2.5. Water splitting cell configuration	63

Chapter 3. Experimental Procedures

3.1. Sample preparation	66
3.1.1. Fabrication of NiFe LDH based electrocatalysts	66
3.1.2. Fabrication of CoS ₂ based electrocatalysts	68
3.2. Thermodynamic calculation	70
3.3. Electrochemical analysis	71
3.4. Morphological and phase analysis	72
3.5. Physical and chemical analysis	72

Chapter 4. Fabrication of B doped NiFe LDH with Galvanostatic Oxidation

4.1. Introduction	73
4.2. Fabrication of boron doped NiFe LDH	73
4.2.1. Optimization of boron sources for boronization	73
4.3. Electrochemical oxidation of boron doped NiFe LDH	80

4.3.1. Optimization of electrochemical oxidation	80
4.3.2. Reaction step of electrochemical oxidation	86
4.4. Characterization of NiFe LDH based electrocatalysts	88
4.5. Summary	100

Chapter 5. Electrochemical Performance of NiFe LDH based catalysts

5.1. Introduction	101
5.2. Electrochemical performances	102
5.2.1. Effects of boron doping in NiFe LDH	113
5.2.2. Effects of electrochemical oxidation	116
5.3. Summary	123

Chapter 6. Design and Fabrication of Porous CoS₂ electrocatalysts

6.1. Introduction	124
6.2. Fabrication of MOF-driven CoS ₂ nanoparticles	125
6.2.1. Thermodynamic calculation	125
6.2.2. Design of the sulfurization	129
6.3. Characterization of MOF-driven CoS ₂ nanoparticles	132
6.4. Summary	143

Chapter 7. Electrochemical Performance of Porous CoS₂ electrocatalysts

7.1. Introduction	144
7.2. Electrochemical performances	145
7.2.1. Effects of nanopores in electrocatalysts	156

7.2.2. Effects of phase control in cobalt sulfide	162
7.3. Summary	170

Chapter 8. Conclusion

8.1. Summary of results	171
8.2. Future works and suggested research	174
References	179
Abstract (In Korean)	201
Curriculum Vitae	204

LIST OF TABLES

- Table 1.1** Boiling point and melting point of boron and boric acid.
- Table 2.1** Comparison of OER catalytic activity with previous reports of transition metal compounds.
- Table 2.2** Comparison of HER catalytic activity with previous reports of transition metal compounds.
- Table 2.3** Comparison of overall water splitting performances with previous reports.
- Table 4.1** ICP-AES analysis for verification of chemical composition of pristine NiFe LDH and B:NiFe LDH.
- Table 5.1** Calculation of ECSA of NiFe LDH and galox-B:NiFe LDH.
- Table 6.1** ICP-AES analysis for verification of chemical composition of MOF-driven cobalt compound.
- Table 7.1** Calculation of ECSA of commercial CoS₂, MOF-driven Co, Co₉S₈, and CoS₂.

LIST OF FIGURES

- Figure 1.1** (a) Schematic for electrochemical cell that performs the electrochemical water splitting under alkaline condition, whose anode and cathode occur OER and HER, respectively. (b) Graph of cost and efficiency for various solar-driven hydrogen production methods including electrocatalysts, photoelectrocatalysts.
- Figure 1.2** (a) Price of electrocatalysts candidates for water splitting including OER, HER. (b,c) The volcano plot, electrocatalytic activity, of (b) OER [27] and (c) HER [28].
- Figure 1.3** Schematic for electrochemical cell: each case is CO₂ reduction [44], water splitting, N₂ reduction [45], and metal-air batteries [46], respectively.
- Figure 1.4** (a) OER performance of comparison between spinel type nickel iron oxides and nickel iron double hydroxides [27]. (b) Crystal structure of NiFe LDH [31]. (c) Volcano plot of OER activity about various transition metal oxides [27]. (d) Volcano plot of OER activity depending on LDHs of Ni & other transition metal alloying [27].

- Figure 1.5** (a) The phase diagram of Ni-Fe [57]. (b) The conductivity data depending on Ni:Fe ratio [21]. (c) The oxygen evolution activity under 0.1 M KOH depending on Ni:Fe ratio [58].
- Figure 1.6** The effect of boron doping. (a) Results of boronized Ni on formation of NiOOH [59]. (b) Effects of boronized Ni on charge transfer resistance and OER performance [60].
- Figure 1.7** (a) O 1s for XPS analysis of Ni base electrocatalysts [61]. (b) Pourbaix diagram of Ni [62].
- Figure 1.8** Schematic illustration of the synthesis of electrochemical oxidized B:NiFe LDH through gas-solid reaction with furnace and activation.
- Figure 1.9** Schematic and examples of metal-organic frameworks. (a) composition of metal-organic frameworks. (b) Various type of metal-organic frameworks [68].
- Figure 1.10** Phase diagram of cobalt-sulfur system [69].
- Figure 1.11** Schematic of the synthesis of MOF-driven CoS₂ through gas-solid sulfurization with thermodynamic calculations.
- Figure 1.12** Strategies of electrocatalysts for enhanced water splitting.

- Figure 2.1** Schematic of the electrochemical alkaline water splitting [74].
- Figure 2.2** Schematic of the simplest case of an electrochemical reaction.
- Figure 2.3** Polarization curves for OER in anode marked in red line and HER in cathode marked in blue line.
- Figure 2.4** i_{net} , as a function of potential determined by the Butler-Volmer equation.
- Figure 2.5** i_{net} change with overpotential in electrochemical reaction that satisfies the Butler-Volmer equation.
- Figure 2.6** Tafel plot in electrochemical reaction.
- Figure 2.7** Determine of current according to the mass transfer in large overpotential condition.
- Figure 2.8** Polarization curves for water oxidation electrodes.
- Figure 2.9** Schematic of OER mechanism in acid (blue line) and alkaline (red line) electrolyte. The black line shows that oxygen evolution involves the intermediates. The green line shows another path in OER [9].

- Figure 2.10** Plot of thermodynamically calculated Gibbs free energy of intermediates during OER according to the reaction coordinate. Dashed line indicate the energetics at the electrode potential where all the thermochemical barriers disappear [74, 78].
- Figure 2.11** Schematic of format of the simple volcano plot. The descriptor, such as difference of Gibbs free energy between intermediates, versus the activity.
- Figure 2.12** The volcano plots for heterogeneous electrocatalysts for water oxidation [32, 87].
- Figure 2.13** Polarization curves for hydrogen evolution in cathode.
- Figure 2.14** Schematic of mechanism of hydrogen evolution in acidic (left) and alkaline (right) electrolyte [103].
- Figure 2.15** (a) Relationship between $\log j_0$ and ΔG_{H^*} under the Langmuir adsorption model [105]. (b) The volcano plots for heterogeneous electrocatalysts for HER of water splitting [28].
- Figure 2.16** The Pourbaix diagrams for (a) Mn, (b) Fe, (c) HCO_2^- , (d) Ni, (e) Cu, (f) P, (g) S, (h) Se, and (i) Te species under 298 K [62, 169].

- Figure 2.17** Schematic profiles of (a) cyclic voltammetry and (b) galvanostatic methods.
- Figure 2.18** Image and schematic diagram of two-electrode full-cell system [33].
- Figure 2.19** Schematics of (a) industrial alkaline water electrolysis, (b) proton exchange membrane (PEM), and (c) anion exchange membrane (AEM) electrolysis [74, 117].
- Figure 3.1** Schematic illustration of the fabrication process, including the hydrothermal, boronization, and electrochemical oxidation, of NiFe LDH based electrocatalysts.
- Figure 3.2** Image of sealed glass ampoule. Co-PBAs and sulfur powder were inserted, and the pressure inside was maintained 0.1 Torr.
- Figure 3.3** Schematic illustration of the fabrication process, including the sulfurization, of MOF-driven cobalt sulfide electrocatalysts.
- Figure 4.1** Schematic of synthesis of first step, boronization except for gray box, of electrocatalysts for efficient water oxidation.
- Figure 4.2** Phase diagram of Ni-B system [170].

- Figure 4.3** Schematic of synthesis of second step, electrochemical oxidation except for gray box, of electrocatalysts for efficient water oxidation.
- Figure 4.4** Pourbaix diagram of nickel system according to the pH. Redraw the ref [62].
- Figure 4.5** The potential profile of the galox-B:NiFe LDH during galvanostatic oxidation at 0.1 and 1.0 mA cm⁻² over 12 hours.
- Figure 4.6** Field-emission scanning electron microscopy (FE-SEM) images of NiFe LDH based electrocatalyst under each condition.
- Figure 4.7** Morphological characterization of B:NiFe LDH. (a) Energy dispersive X-ray spectrometry (EDS) spectrum. (b) EDS scanning image. (c-f) EDS elemental mapping images of B:NiFe LDH. (c) Ni. (d) Fe. (e) B, and (f) O.
- Figure 4.8** Morphological characterization of boron doped NiFe LDH (B:NiFe LDH) and B:NiFe LDH with galvanostatic oxidation (galox-B:NiFe LDH) electrocatalyst. Transmission electron microscopy (TEM) analysis (top of each row) and selected area electron diffraction (SAED) pattern (bottom of each row) of NiFe LDH based electrocatalysts under each condition.

Figure 4.9 High resolution-transmission electron microscopy (HR-TEM) and fast Fourier transformation (FFT) analysis (inset) of (a) NiFe LDH, (b) B:NiFe LDH, (c) B:NiFe LDH after OER test, and (d) galox-B:NiFe LDH.

Figure 4.10 EDS of TEM through STEM analysis of B:NiFe LDH. (a) STEM image. (b) Mixed EDS image of STEM, Ni (green), Fe (yellow), B (red), and O (blue) chemical composition.

Figure 4.11 EDS of TEM through STEM analysis of B:NiFe LDH. EDS mapping of TEM images of the B:NiFe LDH composition (Ni: green, Fe: yellow, B: red, O: blue).

Figure 4.12 Phase characterization and chemical spectra analysis to confirm boronization and electrochemical oxidation inducement. (a) X-ray diffraction (XRD) analysis for confirmation of boronization and electrochemical oxidation. (b) Raman spectroscopy analysis for the NiFe LDH based electrocatalysts. (c) Fourier transformation infrared (FT-IR) analysis to confirm boron doping in NiFe LDH (top of (c): enlargement of FT-IR result).

Figure 4.13 X-ray absorption fine structure (XAFS) results of NiFe LDH based electrocatalysts. (a) X-ray absorption near-edge structure (XANES) and (b) Extended X-ray absorption fine structure (EXAFS).

- Figure 5.1** Electrochemical characterization of the electrodes of NiFe LDH based electrocatalyst for water oxidation in 1.0 M KOH. The OER polarization curves through linear sweep voltammetry (LSV) of different electrodes with a scan rate 1.0 mV s^{-1} .
- Figure 5.2** Electrochemical characterization of electrodes of NiFe LDH based electrocatalyst for OER in 1.0 M KOH. Top: overpotential of each electrode at 10 mA cm^{-2} current density. Bottom: current density of each electrode at overpotential of 250 mV.
- Figure 5.3** Electrochemical characterization of the electrodes of NiFe LDH based electrocatalyst for water oxidation in 1.0 M KOH. The Tafel plot for calculation of Tafel slope of each electrode corresponding to the OER polarization curves.
- Figure 5.4** OER mechanism step through calculation of Tafel slope in typical transition metal LDH.
- Figure 5.5** Electrochemical characterization of the electrodes of galox-B:NiFe LDH electrocatalyst for water oxidation in 1.0 M KOH. Chronopotentiometric durability test at 10 mA cm^{-2} .
- Figure 5.6** Electrochemical characterization of the electrodes of NiFe LDH, B:NiFe LDH electrocatalyst for water oxidation in 1.0 M KOH. Chronopotentiometric durability test at 10 mA cm^{-2} .

- Figure 5.7** Electrochemical characterization of the electrodes of galox-B:NiFe LDH electrocatalyst for water oxidation in 1.0 M KOH. Faradaic efficiency and amount of oxygen and hydrogen during stability test of water splitting at 10 mA cm⁻².
- Figure 5.8** Images of equipment, gas chromatography, of evolved gas analysis during stability test of water splitting.
- Figure 5.9** Electrochemical characterization of the electrodes of NiFe LDH based electrocatalyst for water oxidation in 1.0 M KOH. Nyquist plots through EIS at (a) 350 mV (vs. RHE) (b) 400 mV (c) 450 mV, and (d) OCP state (inset: magnification of low area) for different electrode.
- Figure 5.10** Equivalent circuit model and schematic diagram of the possibility of charge transfer in B doped NiFe LDH.
- Figure 5.11** Chemical composition characterization for verification of enhanced OER electrocatalytic activity. The X-ray photoelectron spectroscopy (XPS) analysis for observation of chemical composition. (a) O 1s, (b) B 1s, (c) Ni 2p, and (d) Fe 2p of NiFe LDH based electrocatalysts under each condition.

Figure 5.12 Specific surface area characterization for verification of enhanced catalytic activity. Brunauer-Emmett-Teller analysis of (a) isothermal plot with N₂ adsorption/desorption, (b) comparison of BET surface area under each condition, and (c) pore distribution.

Figure 5.13 Specific surface area characterization for verification of enhanced catalytic activity. Electrochemical surface area (ECSA) of NiFe LDH based electrocatalyst. The linear slope is related to the double layer capacitance.

Figure 5.14 Cyclic voltammogram for measurement of ECSA of (a) NiFe LDH and (b) galox-B:NiFe LDH.

Figure 5.15 Structural and morphological characterization of galox-B:NiFe LDH electrode after OER durability test. (a) XRD analysis of galox-B:NiFe LDH after 100 hours durability test. (b) FE-SEM image of low magnification (top) and high magnification (bottom) of the galox-B:NiFe LDH electrode.

- Figure 6.1** Thermodynamics calculations in certain condition. (a) Ternary phase diagram at 500 °C for predicting the required composition to form the target phase. (b) The expected products depending on the amount of sulfur through thermodynamic calculated condition. (c) Sulfurization of Co-PBA related gaseous decomposition products at 500 °C. Other products were completely vaporized except for the cobalt sulfide.
- Figure 6.2** Schematic diagram of the fabrication of MOF-driven porous CoS₂.
- Figure 6.3** Image of sealed glass ampoule. Co-PBA and sulfur powder were inserted. The pressure of ampoule was maintained 0.1 Torr.
- Figure 6.4** Characterization of Co-PBA nanoparticles. (a) FE-SEM and (b) TEM images after synthesis of Co-based MOF using simple precipitation method.
- Figure 6.5** Characterization of Co-PBA nanoparticles. XRD analysis for verification of Co-PBA.
- Figure 6.6** Structural characterization for phase analysis of sulfurized Co-PBAs. (a) Annealing for only Co-PBAs, (b) sulfurization of Co-PBAs with 3 mg sulfur, and (c) sulfurization of Co-PBAs with 15 mg sulfur.

- Figure 6.7** XRD analysis of annealed Co-PBAs in 500 °C, air.
- Figure 6.8** Microstructural characterizations, including SEM and TEM, of sulfurized Co-PBAs (MOF-driven Co, Co₉S₈) and commercial CoS₂. (a-c) FE-SEM images and (d-f) TEM images of each cobalt compound, (a), (d) MOF-driven Co, (b), (e) MOF-driven Co₉S₈, and (c), (f) commercial CoS₂.
- Figure 6.9** Microstructural characterizations, including SEM and STEM, of MOF-driven CoS₂. (a) FE-SEM image. (b) STEM image and EDS elemental mapping images (Co: red, S: green in inset).
- Figure 6.10** Microstructural characterization of MOF-driven CoS₂ nanoparticles. (a) TEM image and (b) HR-TEM image and FFT analysis (inset).
- Figure 6.11** The electron energy loss spectroscopy (EELS) spectrum analysis of Co L₂₃ edge for verification of sulfurization from MOF-driven Co, Co₉S₈, and CoS₂ (S/Co-PBAs weight ratio: 0, 0.1, and 0.5).
- Figure 6.12** Chemical characterization of MOF-driven CoS₂ nanoparticles. (a) The broad scan of MOF-driven CoS₂ nanoparticles. (b) O 1s for XPS. (c) Co 2p spectrum. (d) S 2p spectrum of MOF-driven CoS₂.

- Figure 7.1** Electrochemical characterization of each electrode for water oxidation in 1.0 M KOH. The OER polarization curves through linear sweep voltammetry (LSV) of different electrode with a scan rate 1.0 mV s^{-1} .
- Figure 7.2** Electrochemical characterization of each electrode for water oxidation in 1.0 M KOH. Tafel slopes of polarization curves in OER.
- Figure 7.3** Electrochemical characterization of Ir foil, nickel foam, and Pt electrode. (a) OER polarization curves. (b) Tafel slopes of polarization curves in OER.
- Figure 7.4** Electrochemical characterization of MOF-driven CoS_2 electrode. The stability test through chronoamperometric method of fabricated MOF-driven CoS_2 at constant voltage.
- Figure 7.5** Electrochemical characterization of MOF-driven porous CoS_2 nanoparticles in 1.0 M KOH. HER polarization curves of electrode with a scan rate 5 mV s^{-1} .
- Figure 7.6** Electrochemical characterization of MOF-driven porous CoS_2 nanoparticles in 1.0 M KOH. Tafel slopes of polarization curves in HER.

- Figure 7.7** Electrochemical characterization of Ir foil and nickel foam. (a) HER polarization curves. (b) Tafel slopes of polarization curves in HER.
- Figure 7.8** Electrochemical characterization of MOF-driven CoS₂ electrode. The stability test through chronoamperometry of fabricated CoS₂ at constant voltage.
- Figure 7.9** Overall water splitting performance of MOF-driven CoS₂ nanoparticles through polarization curve using symmetric full-cell.
- Figure 7.10** Overall water splitting performance of MOF-driven CoS₂ nanoparticles through chronoamperometric durability test of symmetric full-cell.
- Figure 7.11** Physical adsorption characterization of MOF-driven cobalt compound and commercial CoS₂ electrocatalysts. BET analysis of isothermal plot with N₂ adsorption/desorption.
- Figure 7.12** Physical adsorption characterization of MOF-driven Co₃O₄ electrocatalysts. BET analysis of isothermal plot with N₂ adsorption/desorption.
- Figure 7.13** Physical adsorption characterization of MOF-driven cobalt compound and commercial CoS₂ electrocatalysts. Pore diameter distribution of MOF-driven Co, Co₉S₈, CoS₂ and commercial CoS₂ (inset: magnification of the small pore diameter area).

Figure 7.14 ECSA of commercial CoS₂, MOF-driven Co, Co₉S₈, and CoS₂ (S/Co-PBAs weight ratio: 0, 0.1, and 0.5). The linear slope is related to the double layer capacitance.

Figure 7.15 Nyquist plots at 300 mV (vs. RHE) for commercial CoS₂, MOF-driven Co, Co₉S₈, and CoS₂ (S/Co-PBAs weight ratio: 0, 0.1, and 0.5) electrodes. Inset is equivalent circuit model.

Figure 7.16 Morphological characterization of MOF-driven CoS₂ electrode after stability test. (a) FE-SEM image of the bare nickel foam. (b) FE-SEM (inset: low magnification), (c) TEM, and (d,e) HR-TEM (inset: FFT analysis) image of MOF-driven CoS₂ electrode after OER stability at 1.53 V (vs. RHE). (f) FE-SEM (inset: low magnification), (g) TEM, and (h) HR-TEM (inset: FFT analysis) image of MOF-driven CoS₂ electrode after HER stability at -0.2 V (vs. RHE).

Figure 7.17 XRD analysis for observation of phase change of MOF-driven CoS₂ after 20 hours OER and HER stability test.

Figure 7.18 Chemical composition and electronic state change of MOF-driven CoS₂ after 20 hours OER stability test at 1.53 V (vs. RHE). (a) STEM image and EDS elemental mapping images in inset (cobalt: red, oxygen: yellow, sulfur: green). XPS analysis of MOF-driven CoS₂ after OER stability test. (b) Cobalt 2p, (c) sulfur 2p, and (d) oxygen 1s spectrum, respectively.

Figure 7.19 Chemical composition and electronic state change of MOF-driven CoS₂ after 20 hours HER stability test at -0.2 V (vs. RHE). (a) STEM image and EDS elemental mapping images in inset (cobalt: red, oxygen: yellow, sulfur: green). XPS analysis of MOF-driven CoS₂ after HER stability test. (b) Cobalt 2p, (c) sulfur 2p, and (d) oxygen 1s spectrum, respectively.

Figure 8.1 Schematic diagram of sulfur vacancy induced cobalt disulfide.

Figure 8.2 XRD analysis of sulfur vacancy induced MOF-driven CoS₂ depending on the reaction temperature, CO concentration, and time.

Figure 8.3 XRD analysis of sulfur vacancy induced CoS₂ nanoplates, sulfurized cobalt based nanostructure, depending on the reaction time.

Figure 8.4 FE-SEM and XRD analysis of CoS₂ nanoplates. The CoS₂ nanoplates from thermally sulfurized cobalt hydroxycarbonates through hydrothermal.

Figure 8.5 Electrochemical characterization of sulfur vacancy induced MOF-driven CoS₂ for water oxidation in 1.0 M KOH. The OER polarization curves through LSV of different CO annealing conditions with a scan rate 5.0 mV s⁻¹.

CHAPTER 1

Introduction

1.1. Materials for electrocatalysts of water splitting

With a growing demand of environmentally-friendly and sustainable energy sources, developing highly active and stable non-precious catalysts materials has been strongly urged [1-10]. Among alternative energy methodologies, hydrogen based energy source is one of the most promising candidate due to its high energy conversion efficiency, outstanding energy density, and environmental friendliness [1-10]. Though there are a variety of technologies for production of hydrogen based energy, electrochemical water splitting is the most promising technology in terms of commercial aspects and prospects [11-16]. Furthermore, electrochemical water splitting using electrocatalysts can produce solar-driven hydrogen through combination with a solar cell [17-19].

Figure 1.1(a) shows the schematic for conventional electrochemical cell that performs the electrochemical water splitting under alkaline condition through electrocatalysts. At an anode, oxygen is produced from water oxidation. This reaction is preceded by supplement of electron from external circuit, and by supplement of OH^- from alkaline electrolyte [2, 7, 20-23]. Meanwhile, at a cathode, water is reduced to hydrogen, energy

Chapter 1: Introduction

source, which is the counter reaction of oxygen evolution reaction (OER) [24, 25]. Like the OER, this hydrogen evolution reaction (HER) is also supplied from an external circuit and electrolyte [9, 13, 26].

As shown in Figure 1.1(b), the solar photovoltaics-electrochemical water splitting through electrocatalyst (PV-EC) shows the best energy efficiency among other candidates, such as, photocatalysts, photocatalysts-electrolysis. However, PV-EC has the disadvantage of high cost due to precious metals commonly used for commercialization through electrocatalysts. It is necessary to reduce the cost of the electrocatalysts.

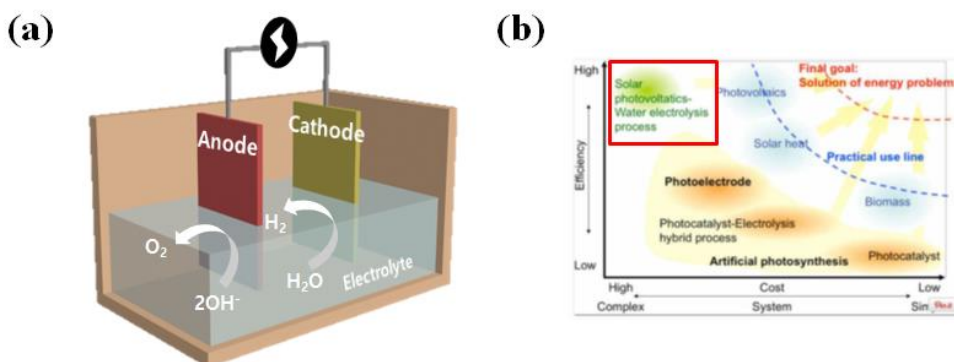


Figure 1.1 (a) Schematic for electrochemical cell that performs the electrochemical water splitting under alkaline condition, whose anode and cathode occur OER and HER, respectively. (b) Graph of cost and efficiency for various solar-driven hydrogen production methods including electrocatalysts, photoelectrocatalysts.

Chapter 1: Introduction

In Figure 1.2(a), the price of materials candidates of electrocatalysts for the water splitting is displayed. Currently used precious metal based electrocatalysts are marked in red and are highly expensive. Thus, recently, the earth-abundant transition metal based electrocatalysts (marked in blue) have been previously reported [7, 21, 24, 27-34]. As shown in Figure 1.2(b, c), rather, it has been reported that it shows better OER (Figure 1.2(b)) and HER (Figure 1.2(c)) catalytic activity than noble metals [35-40]. Nevertheless, for the commercialization of transition metal based electrocatalysts, it is necessary to show better catalytic performance and to supplement for drawbacks, such as charge transfer, active site, and intrinsic conductivity [41-43].

(a) ❖ Price of catalysts candidates

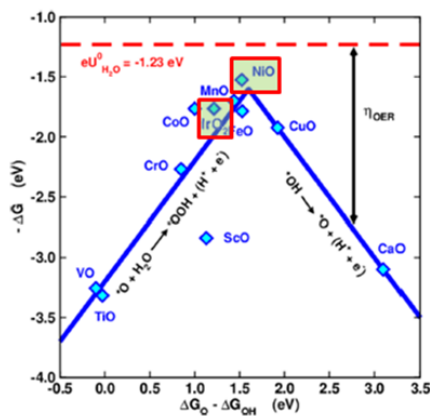
£5-£10 per kilogram £1000-£5000 per kilogram
 £10-£100 per kilogram >£5000 per kilogram
 £100-£1000 per kilogram Price unknown

Note: element prices can vary significantly with quantity and purity

Sc	Ti	V	Cr	Mn	Fe	Co	Ni	Cu	Zn
SCANDIUM	TITANIUM	VANADIUM	CHROMIUM	MANGANESE	IRON	COBALT	NICKEL	COPPER	ZINC
£11508	£2.89	£17.34	£5.86	£1.58	£0.06	£45.65	£7.05	£4.53	£2.17
Y	Zr	Nb	Mo	Tc	Ru	Rh	Pd	Ag	Cd
YTTRIUM	ZIRCONIUM	NIOBIUM	MOLYBDENUM	TECHNETIUM	RUTHENIUM	RHODIUM	PALLADIUM	SILVER	CADMIUM
£26.85	£17.75	£32.22	£12.28	No data	£2343	£58952	£26393	£355	£1.52
La-Lu	Hf	Ta	W	Re	Os	Ir	Pt	Au	Hg
	HAFNIUM	TANTALUM	TUNGSTEN	RHENIUM	OSMIUM	IRIDIUM	PLATINUM	GOLD	MERCURY
	£1085	£183	£19.58	£1255	£9866	£23926	£20325	£29298	£29.49

Andy Brunning/Compound interest 2019

(b)



(c)

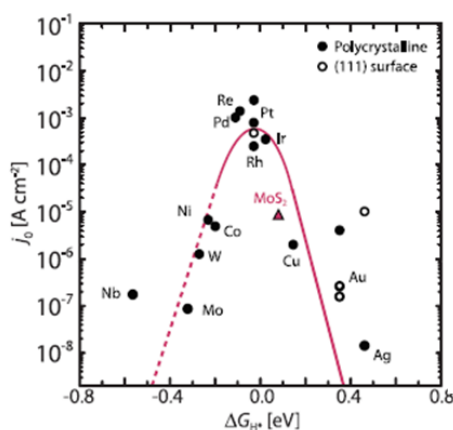


Figure 1.2 (a) Price of electrocatalysts candidates for water splitting including OER, HER. (b,c) The volcano plot, electrocatalytic activity, of (b) OER [27] and (c) HER [28].

Chapter 1: Introduction

As described above, the electrocatalysts candidates for water splitting can be roughly divided into a precious metal and non-precious metal. Although non-precious metal based electrocatalysts is continuously being reported, several problems must be solved for application to mass production of hydrogen. The electrolyzer of electrochemical water splitting consists of anode (OER), cathode (HER), external circuit, and electrolyte. However, both electrodes are generally unbalanced in terms of overpotential [7, 9]. The OER is relatively kinetically hindered reaction compared to HER, because the four electrons are involved in the breaking and formation of bonding [7, 9]. In particular, as shown in Figure 1.3, the OER is essentially accompanied by water splitting as well as a counterpart reaction of various electrochemical reactions. The OER occurs as a counterpart of an electrode where products of CO₂ reduction [44], N₂ reduction [45], and metal-air batteries [46] are reacted. Thus, the total performance of electrocatalysts could be changed depending on the efficiency of OER [7, 17]. Along with the importance of the OER, studies on layer structure type oxides and transition metal chalcogenides among earth-abundant electrocatalysts have been reported as promising candidates [3, 6-8, 11, 24, 31, 47-52].

Furthermore, importance of bifunctional electrocatalysts is also emphasized due to necessity of same electrolyte in one electrolytic cell for low-cost practical applications [12]. Particularly, for bifunctional electrocatalysts, it should show excellent OER performance with outstanding HER performance, and transition metal chalcogenides are one of the representative materials.

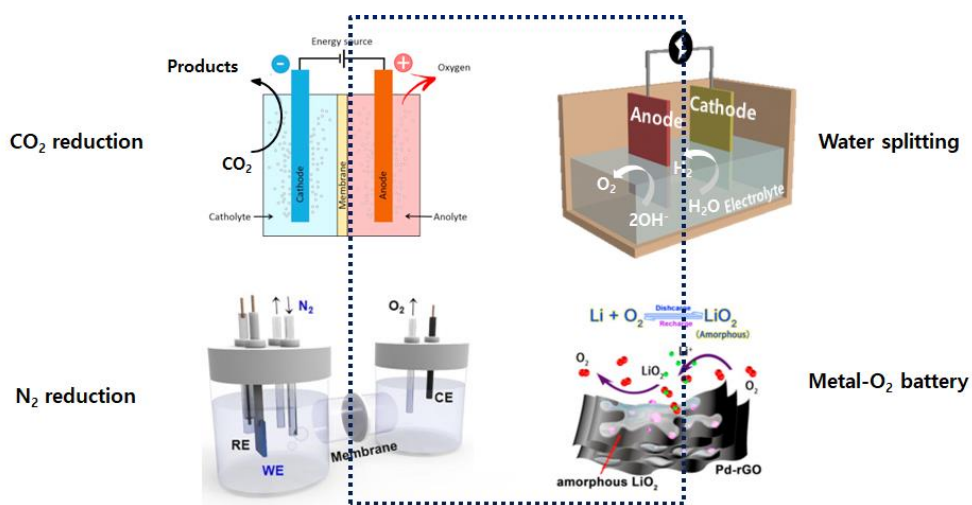


Figure 1.3 Schematic for electrochemical cell: each case is CO₂ reduction [44], water splitting, N₂ reduction [45], and metal-air batteries [46], respectively.

1.2. Charge transfer and phase issues in water splitting catalyst

1.2.1. NiFe LDH based electrocatalysts for water oxidation

Transition metal oxides are typically used as electrocatalysts for water oxidation, however, its intrinsic conductivity is relatively poor. The transition metal oxides for electrocatalysts of water oxidation have various type structures such as spinel, perovskite type, etc [9]. Among them, the layer structure type, such as layered double hydroxides (LDHs), is one of the most promising candidates for water oxidation (Figure 1.4(a)) [27]. The general layer structure type includes transition metal hydroxides ($M(OH)_2$) and oxyhydroxides ($M-OOH$), which are categorized as LDHs [9]. As shown in Figure 1.4(b), the crystal structure of LDHs consists of a layered structure such as graphene and MoS_2 . The anion and hydroxide ligands are located between the interlayer of LDHs [31]. Also, each layer of LDHs consists of edge sharing octahedral structure (MO_6), which is known to act as an active site of OER [53-55].

In transition metal oxides and LDHs, nickel is well-known to have one of the best catalytic activity of water oxidation (Figure 1.4(c)) [27]. Additionally, as shown in Figure 1.4(d), it has been reported through density functional theory (DFT) calculation results that the OER activity is improved when nickel and other transition metals are alloyed [27]. The alloying with various transition metal, such as, Fe, Mn, Cr, etc., affects intrinsic conductivity of LDHs, which shows enhanced activity [24, 56].

Chapter 1: Introduction

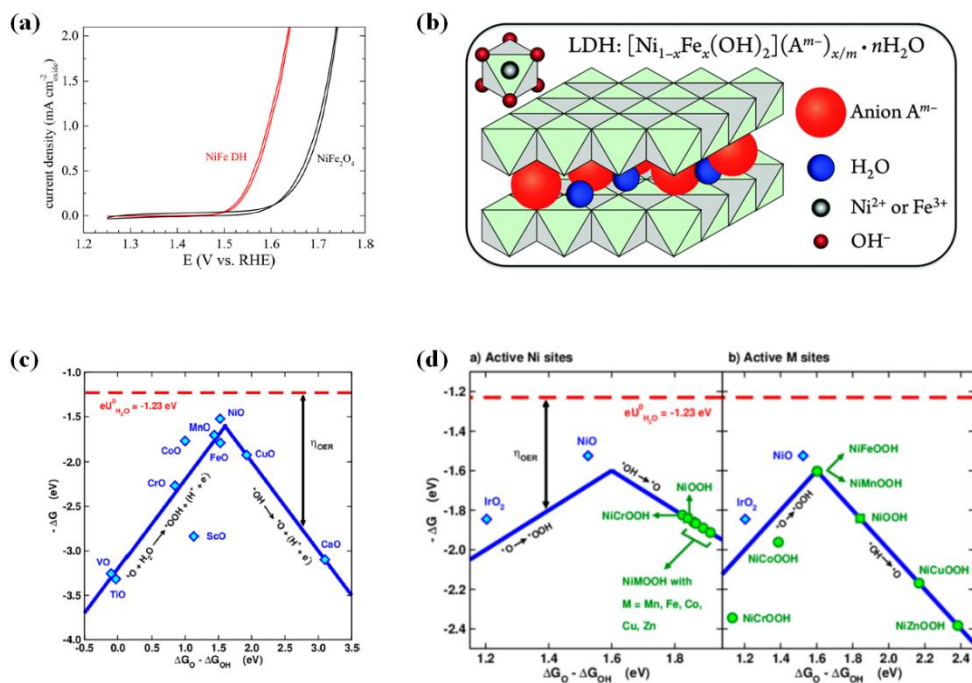


Figure 1.4 (a) OER performance of comparison between spinel type nickel iron oxides and nickel iron double hydroxides [27]. (b) Crystal structure of NiFe LDH [31]. (c) Volcano plot of OER activity about various transition metal oxides [27]. (d) Volcano plot of OER activity depending on LDHs of Ni & other transition metal alloying [27].

Chapter 1: Introduction

In particular, Fe is known to show a positive synergy in OER performance when NiFe LDH in combination with Ni. Fe has the advantage that Ni and Fe are easily alloyed at all Ni:Fe ratio, as shown in the Ni-Fe phase diagram of the Figure 1.5(a) [57]. Figure 1.5(b) shows the conductivity when Fe is alloyed with Ni [21]. When alloying with Ni at the optimal ratio of Fe, it can be seen that conductivity is highly improved compared to pristine Ni, and this change in conductivity also affects OER activity for water oxidation. Figure 1.5(c) displays the OER activity according to the ratio of Fe. The blue line shows the OER overpotential at a current density of 10 mA cm^{-2} , and the red line shows the current density at a potential of 300 mV [58]. In this results, when the ratio of Fe and Ni is between about 20 and 40 at%, the optimal OER performance is exhibited.

Nevertheless, better electrocatalytic activity is required for commercialization of water splitting electrocatalysts through large-scale application. However, since metal alloying beyond ternary is generally difficult, a novel methodology should be required to improve active sites and to enhance charge transfer through improvement of conductivity.

Therefore, in this work, it solved as heteroatoms, such as boron, were doped into NiFe LDH. According to previous study, it was known that when boron was doped with Ni metal, it had more effect on formation of NiOOH, which showed improved OER activity (Figure 1.6(a)) [59]. In addition, in other studies on boron doping, boron doped Ni showed improved conductivity, because charge transfer resistance was improved (Figure 1.6(b)) [60].

Chapter 1: Introduction

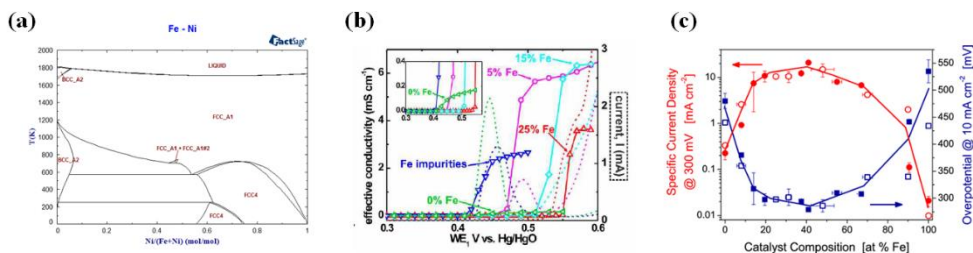


Figure 1.5 (a) The phase diagram of Ni-Fe [57]. (b) The conductivity data depending on Ni:Fe ratio [21]. (c) The oxygen evolution activity under 0.1 M KOH depending on Ni:Fe ratio [58].

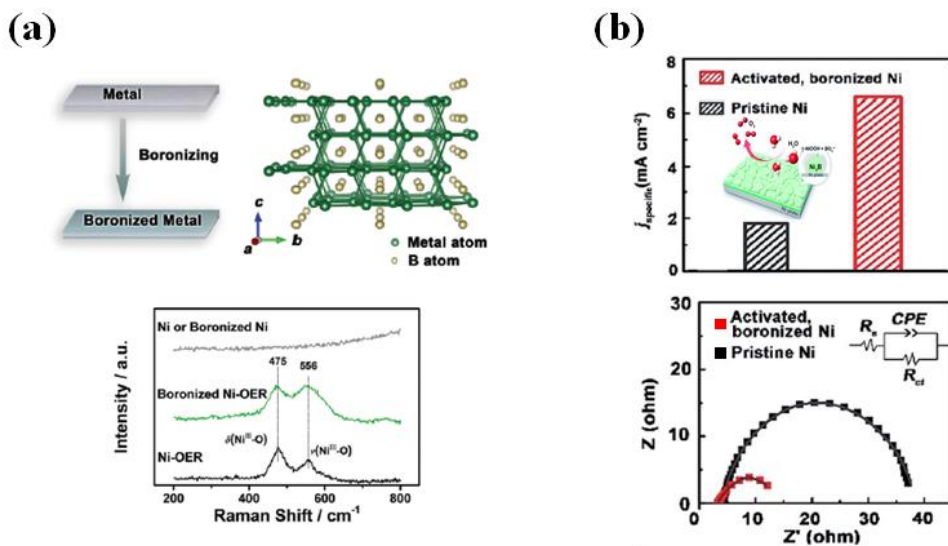


Figure 1.6 The effect of boron doping. (a) Results of boronized Ni on formation of NiOOH [59]. (b) Effects of boronized Ni on charge transfer resistance and OER performance [60].

Chapter 1: Introduction

However, boron doping generally requires high temperature due to its high boiling point and melting point, as indicated in Table 1.1. Thus, a new method of boronization is required.

Additionally, the OER activity of boron doped NiFe LDH (B:NiFe LDH) prepared through a new boronization method was further improved by electrochemical oxidation. As shown in Figure 1.7(a), when the ratio of M-OOH increases, the electrocatalyst is relatively activated, which positively affects the OER electrocatalysts [61]. For activation step, the conditions of electrochemical oxidation were set through the Pourbaix diagram of Ni in Figure 1.7(b) and the ratio of NiOOH was increased [62].

Therefore, boronization was conducted through a boron source instead of boron. As shown in Figure 1.8, the improved OER electrocatalyst was proposed through the advantages of boron doping and NiFe LDH. In addition, the activation of B:NiFe LDH through the setting of the conditions of electrochemical oxidation based on the Pourbaix diagram was suggested.

Table 1.1 Boiling point and melting point of boron and boric acid.

Materials	Boiling point	Melting point
Boron (B)	4,200 K	2,349 K
Boric acid (H ₃ BO ₃)	573 K	443.9 K

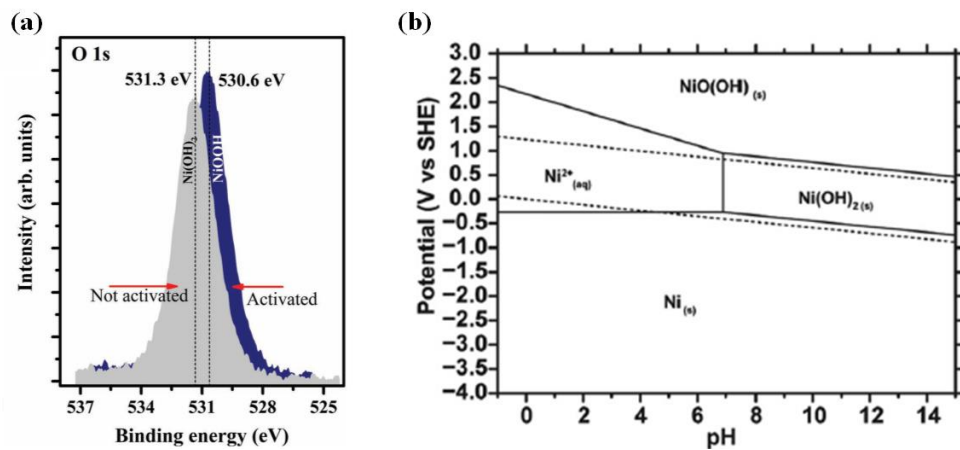


Figure 1.7 (a) O 1s for XPS analysis of Ni base electrocatalysts [61]. (b) Pourbaix diagram of Ni [62].

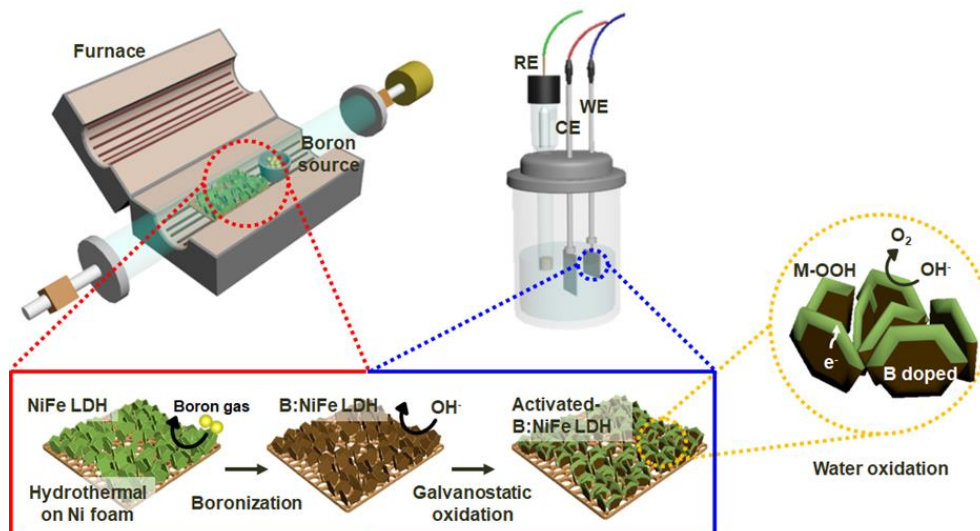


Figure 1.8 Schematic illustration of the synthesis of electrochemical oxidized B:NiFe LDH through gas-solid reaction with furnace and activation.

1.2.2. CoS₂ based electrocatalysts for overall water splitting

In order to apply as a bifunctional electrocatalysts, it should show outstanding performance in both OER and HER catalytic activity. The cost issue is one of the reasons why the bifunctional electrocatalysts was proposed. Thus, bifunctional electrocatalysts have been extensively reported for finding suitable materials through earth-abundant transition metals like the OER in chapter 1.1 [7]. In the anode where OER occurs under alkaline conditions, electrocatalysts, such as transition metal layered double hydroxides [6, 8, 30, 31, 63], selenides [11, 64], and sulfides [65], have been reported to replace precious metal, such as Ir, Ru. Meanwhile, transition metal phosphides [13], carbides [66], and sulfides [14, 67] comparable to performance of Pt have been reported as HER electrocatalysts under acidic condition. Among them, transition metal sulfides were suggested as the most suitable candidates as bifunctional electrocatalysts, because sulfides are relatively stable under alkaline conditions used in bifunctional electrocatalysts, and has outstanding OER and HER catalytic activity [12, 16, 23].

Furthermore, in order to be applied to mass production of bifunctional electrocatalysts for overall water splitting, the manufacturing method of the electrocatalysts should be simple. As the composition of material increases, the synthesis method of catalysts becomes inevitably complicated. For large scale applicable high efficiency electrocatalyst, the methodology should be simple, and the essential factors such as high activity, high conductivity, and large surface area must be satisfied.

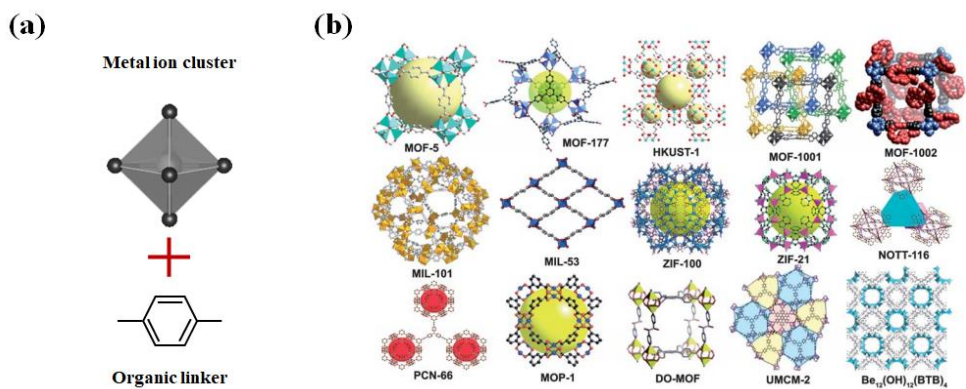


Figure 1.9 Schematic and examples of metal-organic frameworks. (a) composition of metal-organic frameworks. (b) Various type of metal-organic frameworks [68].

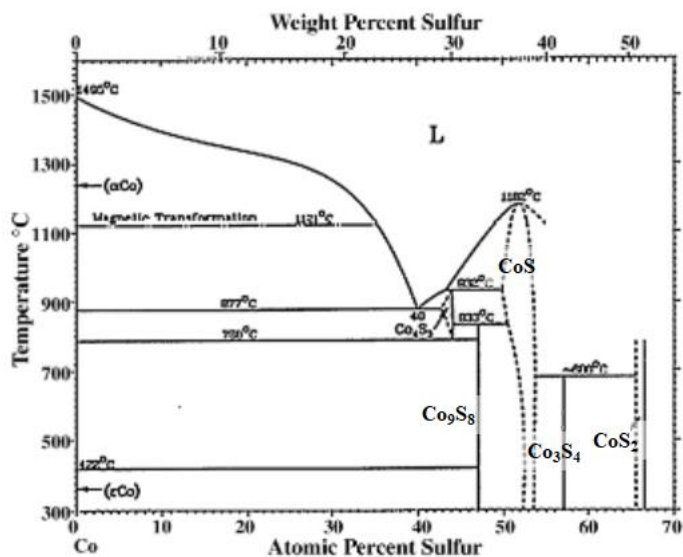


Figure 1.10 Phase diagram of cobalt-sulfur system [69].

Chapter 1: Introduction

As shown in Figure 1.9, the metal-organic frameworks (MOFs) consist of metal ion cluster and organic linker (Figure 1.9(a)), whose combination can produce a variety of MOFs (Figure 1.9(b)) [68]. While MOF has the advantage of high porosity, it has the disadvantage of low conductivity due to the organic linker. Based on these advantages of MOFs, transition metal compounds synthesized using MOF as a template can be outstanding electrocatalysts with a large surface area as exposure of active sites.

The cubic pyrite-phase transition metal dichalcogenides, such as FeS_2 [48, 70], NiS_2 [65, 71], and CoS_2 [7, 65], have been proposed as bifunctional electrocatalysts in spite of simple transition metal compounds due to high activity of OER and HER [23, 67, 70, 72]. In particular, CoS_2 exhibits high electrical conductivity compared to other cubic pyrite-phase [48], and outstanding activity for both reactions [3, 67, 73]. Previous studies on Co based MOFs were nearly synthesized by sulfurization through solution process [67, 73]. Although MOF derived Co compounds through solution process can synthesize hierarchical nanostructure, it is relatively difficult to form nanopores.

Furthermore, as shown in Figure 1.10, cobalt sulfide has a variety of phase, such as CoS , Co_3S_4 , Co_9S_8 , CoS_2 . The catalytic activity of OER and HER could be different depending on phase, S/Co ratio, of cobalt sulfide. Therefore, precise fabrication of mono-phase without impurity requires prediction of synthesis conditions by analysis through thermodynamic calculation such as phase diagram. Additionally, gas phase reaction with sulfur source through furnace was conducted because it is possible to formation of nanopores and it can be more easily applied to mass production.

Chapter 1: Introduction

In this work, as shown in Figure 1.11, the gaseous sulfurization was performed through Prussian blue analogues (PBAs), one of the types of MOFs. In this procedure, cobalt sulfide according to S/Co ratio was synthesized through thermodynamic calculation, and their catalytic activity and porosity were compared.

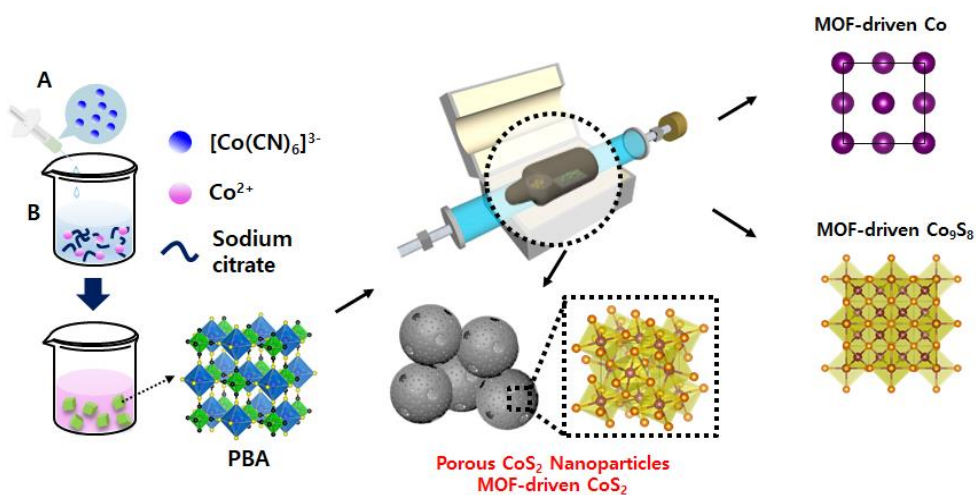


Figure 1.11 Schematic of the synthesis of MOF-driven CoS_2 through gas-solid sulfurization with thermodynamic calculations.

1.3. Objective of the thesis

The electrochemical water splitting is one of the optimal method of energy production for next generation energy source due to their advantages, such as high efficiency, outstanding energy density, and environmental friendliness. Compared with other method for production of hydrogen, the electrochemical water splitting is most future-oriented choices.

Considering the intrinsic conductivity, catalytic activity, and earth abundancy, NiFe LDH and CoS₂ are selected as the anode for electrocatalysts of water oxidation and both electrodes for electrocatalysts of overall water splitting, including OER and HER, respectively. However, selected electrocatalysts have some problems to be solved for efficient water splitting, as described in the previous section. By solving the described issues, it can be approached to large-scale application for commercialization.

To improve the electrochemical performance for water splitting, control of the conductivity of transition metal based compounds was essential because the improved conductivity affects facile charge transfer in electrocatalysts. In the same context, control of active sites of electrocatalysts was also essential. The improved active sites and exposure of active sites affects catalytic activity. However, previously reported studies to solve this problem is a solution that is relatively difficult to apply a large-scale. Moreover, most studies set experimental parameters through trial and error rather than setting parameters through prediction.

The objective of this thesis is to provide the new direction of structural design of electrocatalysts of transition metal compounds for electrochemical water splitting based on a simple gas-solid reaction and thermodynamic calculation, and this methodology affect enhanced electrochemical performances.

Chapter 1: Introduction

The first focus is designing the electrochemical oxidized NiFe LDH with gaseous boronization of hierarchical structure for electrochemical water oxidation. The nickel iron layered double hydroxide was synthesized using the simple hydrothermal, which method is simple and can exclude electrochemically inactive materials since it does not require a polymer binder. Next, boron doped NiFe LDH (B:NiFe LDH) was fabricated through boronization step, which was conducted through annealing of NiFe LDH and boron source. In this procedure, a boron source other than original boron was used due to high boiling point and melting point of boron. Furthermore, through the thermochemical database program, we found a boron source capable of boron doping in NiFe LDH without formation of NiFe boride. Finally, activation of B:NiFe LDH was performed through electrochemical oxidation, which step improves performance of water oxidation by increasing the ratio of oxyhydroxide (M-OOH) in LDH. Like the second step, parameter of electrochemical oxidation was configured in this procedure based on the thermodynamic database, such as Pourbaix diagram. As the electrochemical oxidation method, galvanostatic oxidation was performed by applying a constant current density, because electrochemical oxidation through cyclic voltammetry can cause dissolution and precipitation during negative sweep. It was verified that the galox-B:NiFe LDH designed in above procedures was successfully doped and oxidized through various characterization. In particular, the electrochemical performance, one of the most important indicators, of synthesized electrocatalyst was shown to be superior to Ir, precious metal. The synthesized electrocatalyst achieved an overpotential of 229 mV at 10 mA cm⁻², which confirmed that it was approximately 140 mV lower than Ir under the same conditions. In addition, it shows comparable excellent performance when compared with previous studies.

Chapter 1: Introduction

The second focus is fabricating the highly porous CoS₂ electrocatalyst for overall water splitting, including OER and HER, and controlling its phase and porosity. The electrocatalyst of mono-phase to increase the performance and electrocatalyst to increase the exposure of the active site were synthesized. The cobalt disulfides were synthesized through three steps including the thermodynamic calculation, which was used to implement precise phase control and to verify which phases are fabricated according to loading amount. First, Co-PBAs (Co₃[Co(CN)₆]₂), one of the MOFs, was used as a starting material for synthesis of porous CoS₂. The Co-PBAs was fabricated through simple precipitation. Next, for sulfurization, the loading amounts of Co-PBAs and sulfur were set by thermodynamic calculation. Oxygen was controlled through a vacuum pump because Co-PBAs formed cobalt oxide more easily than sulfide. In addition, when the amount of Co-PBAs is fixed, only the amount of sulfur is a parameter. Thus, the amount of sulfur can be adjusted to predict the cobalt sulfide phase to be synthesized. We demonstrated that highly porous structures were effective at enhancing the OER and HER electrocatalytic activities of the CoS₂ nanoparticles. Tens of nanometer size CoS₂ nanoparticles through PBAs, one of the MOFs categories, were successfully synthesized through gas phase sulfurization using furnace. Synthesized CoS₂ exhibited highly uniform particle size, high porosity, and crystallinity.

In particular, the OER performance, one of the most important indicators, of synthesized electrocatalyst was shown to be superior to IrO₂. The synthesized electrocatalyst achieved an overpotential of 298 mV at 10 mA cm⁻², which confirmed that it was approximately 75 mV lower than commercial IrO₂ under the same conditions. Additionally, the bifunctional electrocatalytic performance showed 1.65 V in a full cell composed of two electrodes closest to the real system.

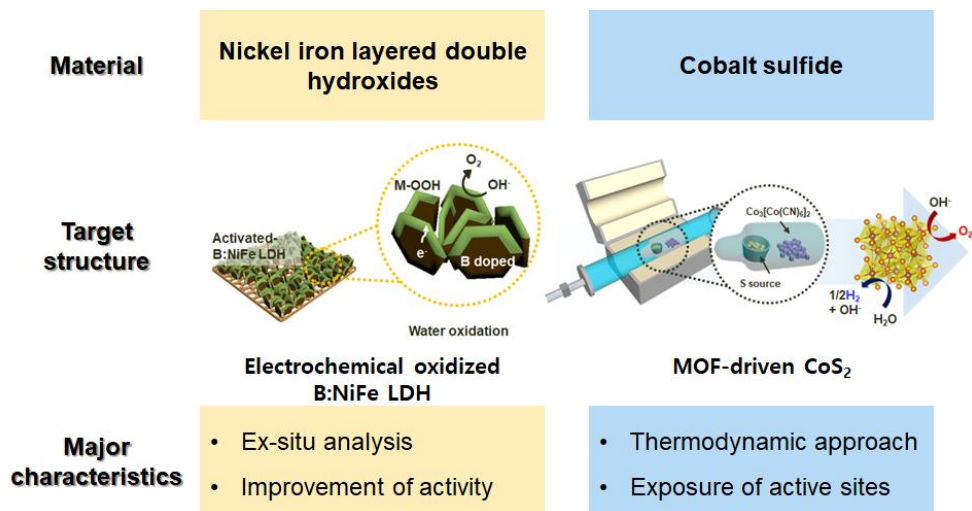


Figure 1.12 Strategies of electrocatalysts for enhanced water splitting.

1.4. Organization of the thesis

This thesis consists of eight chapters. In Chapter 2, the mechanisms of electrochemical water splitting and evaluation of performance of electrocatalysts for water splitting are reviewed. Chapter 3 describes the experimental procedures, including the fabrication of electrocatalysts and the methods used for the various investigations, such as electrochemical, morphological, chemical, and physical characterization. The fabrication of electrochemical oxidized NiFe LDH with gaseous boronization is described in Chapter 4. These procedures were discussed from boronization for boron doping into NiFe LDH to galvanostatic oxidation for activation of boron doped NiFe LDH. Also, characterizations for verification were discussed. In Chapter 5, the effects of boron doping and galvanostatic oxidation on electrochemical performance were described. Chapter 6 describes the design and fabrication of porous CoS₂ electrocatalysts. In particular, Chapter 6 includes parameters setting through thermodynamic calculation. In Chapter 7, the effects of nanopores and phase control of cobalt sulfide on electrochemical performance were discussed. Finally, Chapter 8 summarizes this thesis and suggests further study of sulfur vacancy of CoS₂ for efficient water oxidation and a novel structure composed of nickel boride and oxyhydroxide for the water oxidation.

CHAPTER 2

Theoretical Background

2.1. Fundamentals of electrochemical water splitting

The various factors are used to evaluate the performance of electrocatalysts of water splitting, which are determined through factors of electrocatalytic kinetics.

In this section and following subsections, it is described that how these factors are used and how they are derived in electrochemistry. Furthermore, the fundamentals of components, including thermodynamics, kinetics parameters, of electrochemical water splitting are reviewed.

2.1.1. Thermodynamics of water splitting reactions

Figure 2.1 depicts the electrochemical alkaline water splitting, which broadens the range of electrocatalysts to earth-abundant materials compared with acidic water electrolysis [74]. Two reactions in both electrodes of electrochemical water splitting have been described.

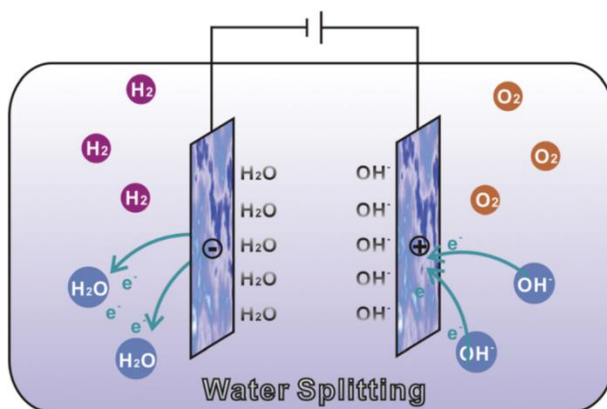
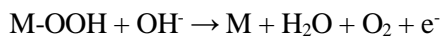
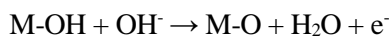
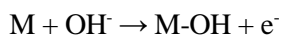


Figure 2.1 Schematic of the electrochemical alkaline water splitting [74].

In OER electrode, anode, side, as described above, the OER process consists of four steps. In the typical known OER step occurs as four steps progress, each step occurs as hydroxide anion (OH^-) is continuously bound to the active site. The OER mechanism is briefly described as follows, and a more detailed mechanism is described in a later section [9].

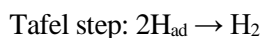
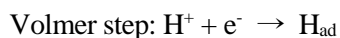


Oxygen is produced as a final product according to the steps described above. Firstly, OH^- is adsorbed to M, the active site of electrocatalyst, to form M-OH. Next, M-OH again combines with OH^- to form M-O, yielding H_2O and e^- . After this formation of M-O step, it is divided into two processes. In the first case, oxygen is generated directly

Chapter 2: Theoretical Background

from M-O. In the second case, M-OOH is formed by combination with M-O and OH⁻, which step releases an electron. Then, M-OOH recombines with OH⁻ to return to active site (M), producing water molecule and oxygen [75, 76]. In order to improve the overall OER catalytic activity, it is necessary to understand in detail the interaction between the active site of catalysts surface and the OER intermediate [77]. Through the Gibbs free energy of each step, the rate determining step (RDS) of the entire OER reaction can be identified, and if it is controlled, OER performance can be improved. Therefore, the corresponding RDS is known as the reaction step with the highest free energy [78]. In particular, recent advances in density functional theory (DFT) calculations have made it relatively simple to model electrochemical reactions thermodynamically.

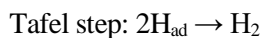
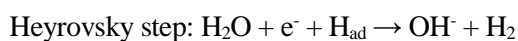
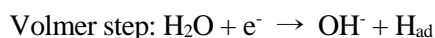
In HER, as described above, there is an advantage of alkaline electrolyte of water splitting, but the activity of HER is relatively low, which have been reported that almost ~2-3 orders of magnitude lower than that in acidic media. Additionally, the HER is relatively sensitive to surface structures of electrocatalysts [74]. For this reason, the generally reported steps that occur in the HER change. According to the theoretical studies revealed, HER activity is known to be related to hydrogen adsorption (H_{ad}) in acidic conditions, which was composed of Volmer, Heyrovsky, Tafel step, as shown below [79, 80].



It shows the behavior of Volmer/Heyrovsky step or Volmer/Tafel step depending on the electrocatalysts.

Chapter 2: Theoretical Background

However, in the water electrolysis of alkaline conditions, the H_{ad} should be considered as being converted to hydroxyl adsorption (OH_{ad}). Accordingly, H^+ of the step described above should be considered as H_2O [81, 82]. Thus, in the alkaline condition, the steps should be changed as follows.



Therefore, it is most essential to break the strong covalent H-O-H bond in order to proceed with efficient HER in alkaline electrolyte. That is, an electrocatalysts with the ability to decompose water molecules and bond hydrogen is needed. It has been reported that the four major factors might influence the alkaline HER performance. Based on the reaction pathway involved in the Volmer and Heyrovsky steps, water adsorption on active sites, water dissociation ability, hydrogen binding energy, and adsorption strength of aqueous OH^- [74]. Particularly, water adsorption, the first step in HER of alkaline condition, is much weaker than H_3O^+ adsorption, the first step in HER of acid condition. Therefore, improving metal- H_2O binding has a positive effect on the HER performance that will occur after step.

2.1.2. Electrocatalytic kinetics and related parameters

(*This section cited reference [166])

The electrocatalysts are a material that facilitates the electrochemical reaction, which are oxidation and reduction reactions caused by charge transfer, such as eqn (2.1). As shown in Figure 2.2, it considers the simplest case of an electrochemical reaction, where O and R are the materials that are oxidized and reduced, respectively. The electrocatalyst could act as electrodes or act on the surface of electrodes. The electrocatalyst, such as catalysts of water splitting, CO₂ reduction, fuel cell, used to adsorb reactant on the surface of electrodes. Then, the facile charge transfer between the electrode and reactant was performed through adsorbed intermediates [9].

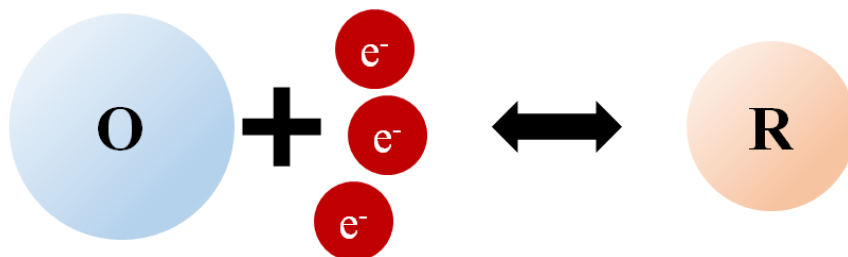


Figure 2.2 Schematic of the simplest case of an electrochemical reaction.

There are many parameters related to kinetics for evaluating electrocatalysts [83]. Typically, these parameters include overpotential (η), exchange current density (j_0), Tafel slope, and turnover frequency, etc., through which useful information can be

Chapter 2: Theoretical Background

obtained. Furthermore, the mechanism analysis related to electrochemistry can be performed with the information obtained through these parameters, which will be explained in more detail in the following.

First, **overpotential** (η) is the most representative and most commonly used evaluation index of electrocatalysts, which is one of the most intuitive kinetics parameter. As shown in the Figure 2.3, it is depicted that the real applied potential (E) and the potential at equilibrium (E_{eq}) are different. In an ideal case, E_{eq} and applied potential should be the same, but in most practical case, the applied potential is inevitably high due to kinetic problems at the electrode and electrocatalyst. Particularly, it is also the reason why the overpotential of the OER is generally greater than that of the HER, which is why OER is called a kinetically hindered process. The overpotential (η) as expressed in eqn (2.2), is a difference between the E and E_{eq} , where E is applied potential and E_{eq} is equilibrium potential. The applied potential (E) is expressed as eqn (2.3) according to the Nernst equation [167]. In the Nernst equation, E is applied potential. E^0 is standard electrode potential, which is a figure that shows how well the redox reaction takes place at a standard pressure of 25 °C and 1 atm. R , T , and F are gas constant, absolute temperature, and Faradaic constant. The n is the number of electrons participating in the electrochemical reaction, and C_O and C_R are the concentrations of oxidized and reduced reagents, respectively.

$$\eta = E - E_{eq} \quad (2.2)$$

$$E = E^0 + \frac{RT}{nF} \ln \frac{C_O}{C_R} \quad (2.3)$$

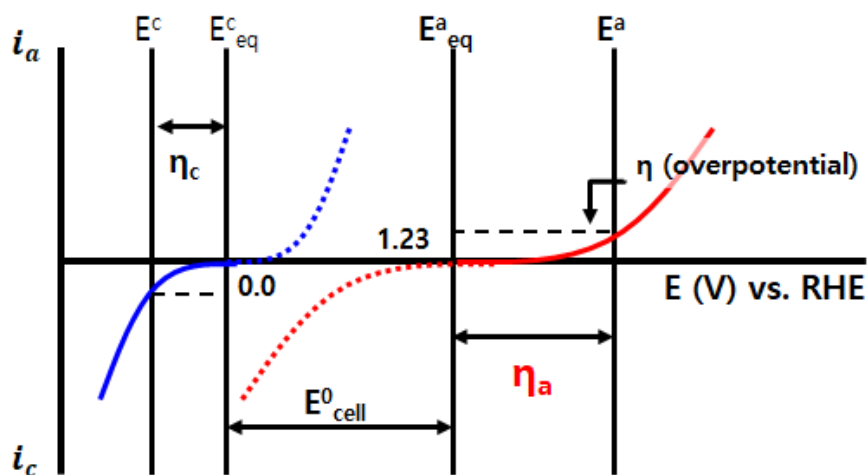


Figure 2.3 Polarization curves for OER in anode marked in red line and HER in cathode marked in blue line.

Generally, the overpotential means the potential value at certain current density, which is typically based on 10 mA cm^{-2} . Therefore, the smaller the overpotential value, the closer it is to the ideal case, which means that it is a better electrocatalysts.

Next, **exchange current density** (j_0) is introduced. In commonly chemical reaction, the forward and backward reaction are expressed as eqn (2.4). In eqn (2.4), k_f and k_b are forward reaction and backward reaction of reaction rate constant, which is related by activated complex theory in eqn (2.5) [166].

$$v_f = k_f C_A, v_b = k_b C_B, v_{net} = k_f C_A - k_b C_B, v_{net} = 0 \text{ (equilibrium)} \quad (2.4)$$

$$k_f = A_f \exp(-\Delta G_f/RT), k_b = A_b \exp(-\Delta G_b/RT) \quad (2.5)$$

In electrochemical reaction, such as eqn (2.1), if charge transfer step determines

Chapter 2: Theoretical Background

overall reaction rate, v_f , v_b , and i_{net} is expressed as eqn (2.6). In eqn (2.6), $C_O(0,t)$ and $C_R(0,t)$ are concentration of O and R on surface of electrode, because only O and R at the surface of electrode participate in the charge transfer step. Thus, reaction rate constant of forward and backward reaction in electrochemical reaction are expressed as eqn (2.7), where A , k_0 , and α are surface area, standard rate constant, and symmetry factor.

$$v_f = k_f C_O(0,t) = i_c/nFA, v_b = k_b C_R(0,t) = i_a/nFA, v_{net} = v_f - v_b = i_{net}/nFA \quad (2.6)$$

$$i_{net} = i_c - i_a = nFA[k_f C_O(0,t) - k_b C_R(0,t)]$$

$$k_f = k^0 \exp(-\alpha nF(E-E^0)/RT), k_b = k^0 \exp((1-\alpha)nF(E-E^0)/RT) \quad (2.7)$$

$$i_{net} = i_c - i_a \quad (2.8)$$

$$= nFAk^0 [C_O(0,t) \exp(-\alpha nF(E-E^0)/RT) - C_R(0,t) \exp((1-\alpha)nF(E-E^0)/RT)]$$

As shown in eqn (2.8), the first term on the right refers to the reduction current and the second term refers to the oxidation current. In equilibrium state, there are $i_{net} = 0$ and $i_c = |i_a|$, which called exchange current, i_0 . Thus, as shown in eqn (2.9), exchange current (i_0), $i_0 = i_c$, deduced from eqn (2.8), where $E = E_{eq}$. Additionally, since the concentration of surface and bulk is the same, eqn (2.10) is validated. Thus, eqn (2.12) is derived from eqn (2.9).

$$i_0 = i_c = nFAk^0 C_O^* \exp(-\alpha nF(E_{eq}-E^0)/RT) \quad (2.9)$$

$$C_O(0,t) = C_O^*, C_R(0,t) = C_R^* \quad (2.10)$$

$$E_{eq} = E^0 + \frac{RT}{nF} \ln \frac{C_O^*}{C_R^*} \quad (2.11)$$

$$C_O^*/C_R^* = \exp(nF(E_{eq}-E^0)/RT), (C_O^*/C_R^*)^{-\alpha} = \exp(-\alpha nF(E_{eq}-E^0)/RT)$$

Chapter 2: Theoretical Background

$$i_0 = nFAk^0 C_O^{*(1-\alpha)} C_R^{*\alpha} \quad (2.12)$$

Thus, exchange current is derived as eqn (2.12), and exchange current density (j_0) is exchange current (i_0) divided by surface area (A). The magnitude of the j_0 means the intrinsic bonding/charge transferring interaction between the electrocatalysts and the reactants. That is, high j_0 is usually corresponding to good electrocatalysts for the electrochemical reaction. However, measurement of j_0 is difficult due to only acquisition of overall current density in real data. Thus, the Tafel equation should be used to calculate the exchange current density (j_0) [9]. Additionally, k^0 , standard rate constant, is intrinsic value of the electrochemical reaction regardless of potential, as shown in eqn (2.5). If this k^0 value is large, ΔG_0 is small. An electrocatalyst is used to further lower ΔG_0 . However, even when an electrocatalyst is used, the magnitude of current can be adjusted by changing the applied potential. From eqn (2.8) and eqn (2.12), it can be expressed as eqn (2.13) using overpotential ($\eta = E - E_{eq}$).

$$i_{net} = i_0 [(C_O(0,t)/C_O^* \exp(-\alpha nF(E-E_{eq})/RT) - C_R(0,t)/C_R^* \exp((1-\alpha)nF(E-E_{eq})/RT)] \quad (2.13)$$

The upper term refers to the reduction current of O, the lower term refers to the oxidation current of R, the ratio of concentration means the mass transfer rate, and the term expressed as an exponential function means the charge transfer rate. As mentioned earlier, the contents related to charge transfer and mass transfer will be covered in the next chapter.

As mentioned in the exchange current density (j_0), the importance of the **Tafel equation** is emphasized. The Butler-Volmer equation should be derived to draw a

Chapter 2: Theoretical Background

Tafel plot through the Tafel equation. When the mass transfer rate is large in an electrochemical reaction, the overall RDS becomes a charge transfer. In this case, $C_O(0,t)/C_O^* = C_R(0,t)/C_R^* = 1$ is established at eqn (2.13), can be summarized as eqn (2.14).

$$i_{net} = i_0[\exp(-\alpha nF\eta/RT) - \exp((1-\alpha)nF\eta/RT)] \quad (2.14)$$

The eqn (2.14) is called the Butler-Volmer equation, which shows the change in current according to the applied potential when the charge transfer is RDS. When a potential is applied as a negative value, the reduction current increases exponentially and the oxidation current decreases exponentially, such as HER. As shown in Figure 2.4, it is a schematic diagram of the Butler-Volmer equation. It can be seen that $i_{net} = 0$ in the equilibrium state, and the reduction current or the oxidation current increases or decreases depending on the applied potential.

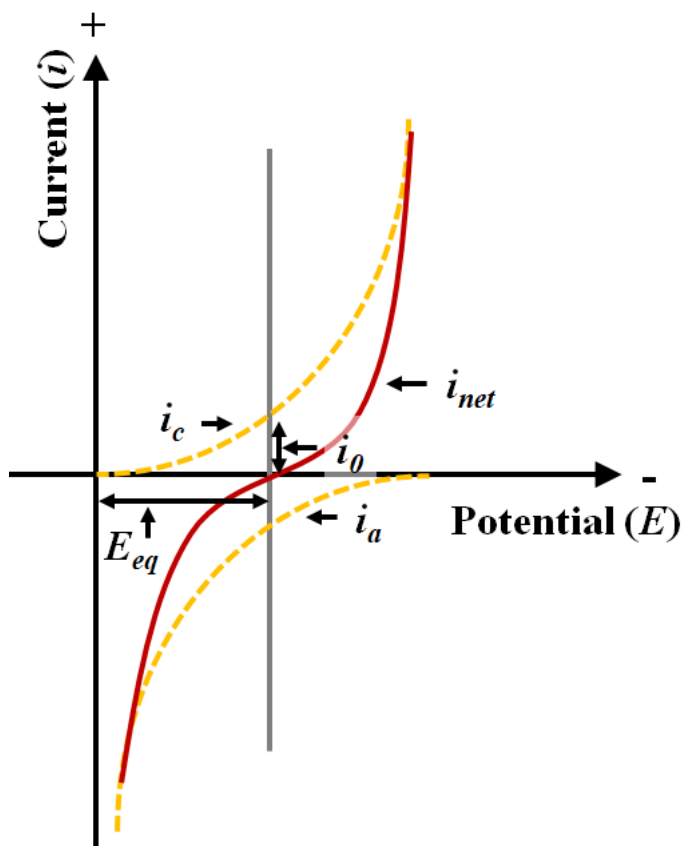


Figure 2.4 i_{net} , as a function of potential determined by the Butler-Volmet equation.

Chapter 2: Theoretical Background

As shown in Figure 2.4, the i_{net} measured in a region with a small overpotential in the potential region that satisfies the Butler-Volmer equation is linearly proportional to the potential. Thus, if absolute value of overpotential is under the approximately $(118/n)$ mV, eqn (2.14) is converted to eqn (2.16) due to eqn (2.15). In eqn (2.16), current and overpotential are directly proportional.

$$\exp(x) = 1 + x + x^2/2 + x^3/6 + \dots, \exp(x) \approx 1 + x \quad (2.15)$$

$$i = i_0 n F (-\eta) / RT \quad (2.16)$$

Additionally, slope of Butler-Volmer equation in small overpotential region is $i_0 n F / RT$ from eqn (2.16). In this region, as indicated in eqn (2.17), resistance is charge transfer resistance because RDS is charge transfer. As shown in Figure 2.5, if R_{ct} is large, the slope decreases. As can be inferred from Figure 2.4, as the slope decreases, the overpotential increases at a constant current. Thus, as R_{ct} increase, the overpotential increases.

$$R_{ct} = RT / i_0 n F \quad (2.16)$$

As shown in Figure 2.5, in the potential range that satisfies the Butler-Volmer equation, $i \approx i_a$ or $i \approx i_c$ in a region where the overpotential is large. If $\eta \ll 0$, the Butler-Volmer equation is changed to eqn (2.17), and eqn (2.18) is derived. In the opposite case, eqn (2.19) is derived.

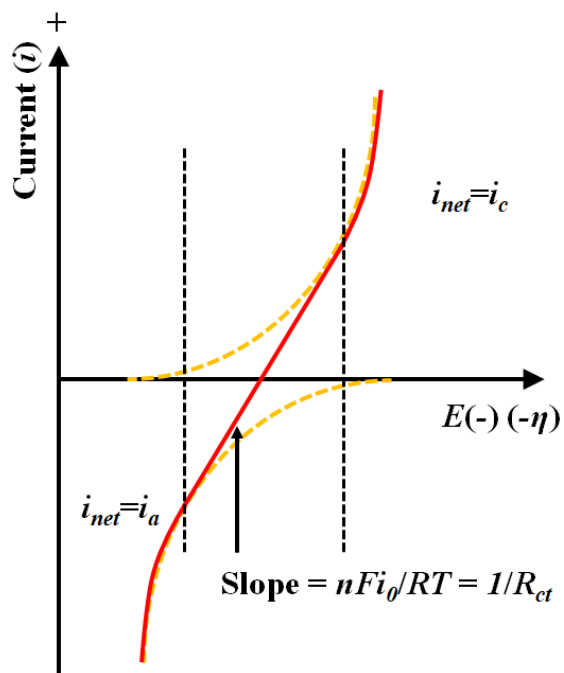


Figure 2.5 i_{net} change with overpotential in electrochemical reaction that satisfies the Butler-Volmer equation.

$$i_{net} \approx i_c = i_0 \exp(-anF\eta/RT) \quad (2.17)$$

$$\log |i_{net}| = \log i_0 - anF\eta / 2.303RT \quad (2.18)$$

$$\log |i_{net}| = \log i_0 + (1-\alpha)nF\eta / 2.303RT \quad (2.19)$$

Chapter 2: Theoretical Background

In Figure 2.6, the logarithm of the current is plotted against overpotential, which is called Tafel plot. As inferred from eqn (2.18) and eqn (2.19), $\log |i_{net}|$ is linearly proportional to the overpotential (η), which is called the Tafel behavior. Also this region is called a Tafel region. In the Tafel plot, i_0 can be calculated from the intercept. Additionally, k^0 , R_{ct} can be calculated from i_0 . Furthermore, α can be obtained from the slope.

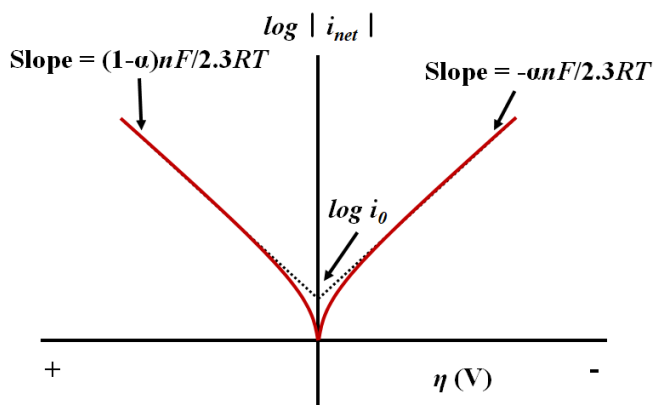


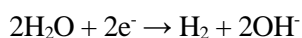
Figure 2.6 Tafel plot in electrochemical reaction.

Chapter 2: Theoretical Background

In an electrochemical reaction, Faraday efficiency (FE) is the efficiency of electrochemical reaction for a specific product, such as oxygen, hydrogen, is expressed in terms of electron transfer. The Faraday efficiency is expressed as eqn (2.20).

$$FE (\%) = ZnF / Q \quad (2.20)$$

The Z, n, F, and Q are number of electrons for 1 mol gas, number of moles, Faraday constant (96,500 C mol⁻¹), and passed charge. In water splitting, since the following chemical reaction formula is followed, Z is 4 in FE of oxygen and Z is 2 in FE of hydrogen.



The turnover frequency (TOF) is generally a factor for evaluating the intrinsic catalytic activity to each catalytic active site. The TOF is expressed as eqn (2.21), where j is the current density at a certain overpotential, A is reaction area of electrocatalysts, n is the number of the moles of the electrocatalysts. Although TOF cannot be accurate due to the different catalytic activity for each atom corresponding to each electrocatalysts, it is still one of the important evaluation factors [84].

$$TOF (s^{-1}) = jA / 4Fn \quad (2.20)$$

2.1.3. Charge and mass transfer

(*This section cited reference [166])

The Butler-Volmer equation mentioned above describes the change in current with potential when the charge transfer rate is slower than the mass transfer rate. That is, it means that the overall reaction rate is determined due to the slow mass transfer rate. In this conditions, as in eqn (2.14), the charge transfer rate (current) increases with the exponential function of overpotential. However, in the actual electrochemical reaction, the current does not increase indefinitely linearly as the overpotential increases. When the charge transfer rate increases linearly till certain condition, the charge transfer rate reaches a region that exceeds the mass transfer rate. Subsequently, mass transfer determines the overall reaction rate. As shown in Figure 2.7, it shows the current change according to the overpotential closer to the actual electrochemical reaction. If the mass transfer rate is constant, in the region where the overpotential is small, the charge transfer determines the overall reaction rate, and the current changes by the Butler-Volmer equation, but in the region where the overpotential is large, the overall reaction rate and current are determined by the mass transfer rate.

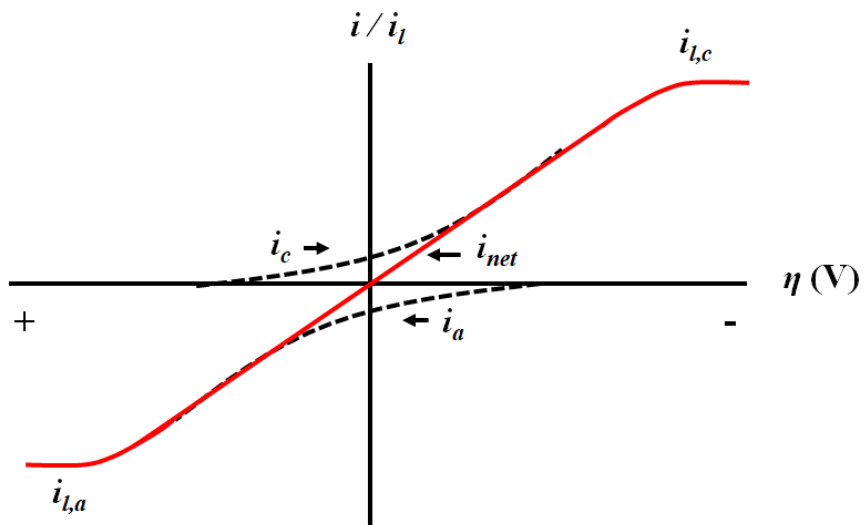


Figure 2.7 Determine of current according to the mass transfer in large overpotential condition.

2.2. Electrochemical oxygen evolution reaction (OER)

The OER of water splitting was conducted in anode, which is oxidation electrode. The oxidation of water is a counter reaction of HER of water splitting. In other words, the OER is the half reaction of the water splitting. Unlike the other electrochemical reactions, such as CO₂ reduction, N₂ reduction, the water splitting does not need to consider competitive reactions because water splitting is only one product. Thus, in water splitting, lowering the overpotential is one of the best ways to increase efficiency. In particular, because OER is a kinetically hindered process, the overpotential is still high. In addition, OER involving multiple steps is also effective in improving efficiency by lowering the ΔG of each step. Thus, DFT calculation was introduced for lowering the ΔG of each step.

As shown in Figure 2.8, this graph displays a basic OER performance curves in white box. In ideal case, the electrochemical water splitting occurs at 1.23 V (vs. reversible hydrogen electrode (RHE)), which is defined as E_{eq} . Because of kinetics, the OER generated at the anode should be applied with a potential greater than 1.23 V. If this is replaced with the overpotential which is the performance factor of OER, it is $\eta = E_a - E_{eq}$, and as previously mentioned, the overpotential at 10 mA cm⁻² is typically used.

In this section, the detailed mechanism and theory for the water oxidation are reviewed. Furthermore, the trends and performances in electrocatalytic activity of OER for water splitting according to the suggested descriptors are described.

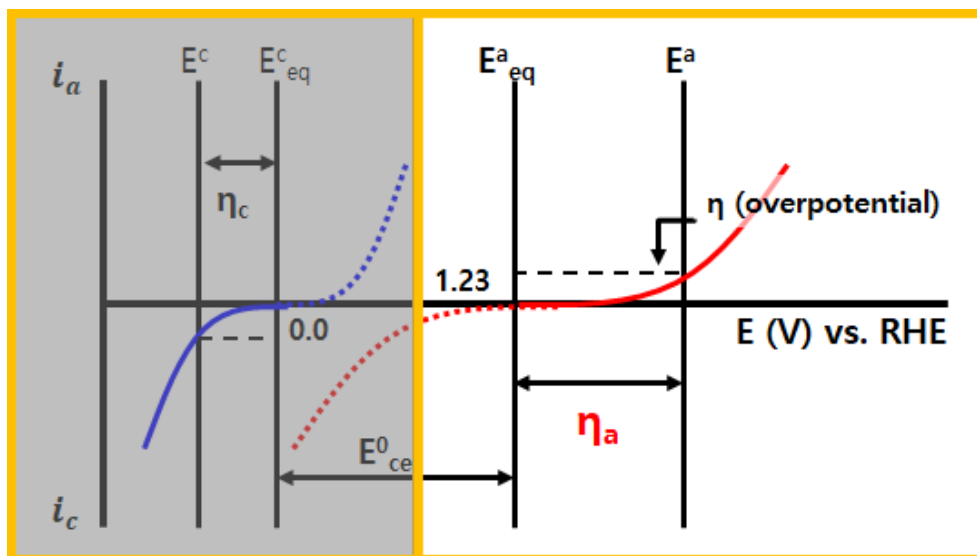
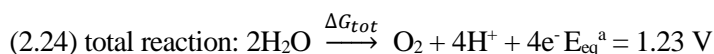
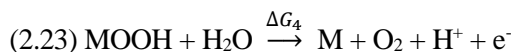
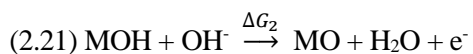
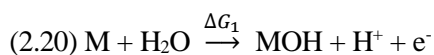


Figure 2.8 Polarization curves for water oxidation electrodes.

2.2.1. Theory of electrochemical OER

In terms of a mechanistic analysis of the OER for water splitting, whose major obstacle is the multiple steps involving the transfer of four electrons. In addition, as briefly mentioned above, the mechanism of water splitting varies depending on the conditions of the electrolyte, such as neutral, acidic, alkaline conditions.

Over the past few decades, many research groups have suggested possible mechanism of OER for water oxidation in acidic or alkaline condition. The mechanism most likely to proposed is the one shown in Figure 2.9 [9]. Under the both conditions, alkaline and acidic conditions, MO, MOH, and MOOH are commonly produced as intermediates. The eqn (2.20) to eqn (2.24) represent the mechanism in acidic conditions.

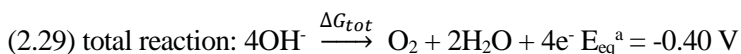
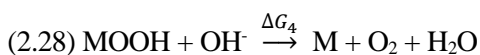
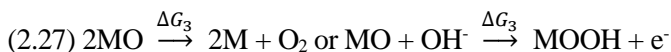


As shown in the blue line of Figure 2.9, first, when H₂O molecule is absorbed at the active site M of the surface, one MOH, an electron, and one proton are generated. The formed MOH meets OH⁻ to form MO, H₂O, and one electron. Next, it is divided into two paths. In first case, MO directly generates O₂, and the MO back to M. In second case, MO react with H₂O to make one MOOH, electron, and proton, respectively. Finally, MOOH meets H₂O again and returns to M, generating O₂ and releasing one proton and electron. Totally, water oxidation in acidic conditions produces oxygen from

Chapter 2: Theoretical Background

2H₂O.

The eqn (2.25) to eqn (2.29) represent the mechanism in alkaline conditions.



Oxygen is produced as a final product according to the steps described above. Firstly, OH⁻ is adsorbed to M, the active site of electrocatalyst, to form MOH. Next, the formed MOH again combines with OH⁻ to form MO, yielding H₂O and e⁻. After this formation of MO step, it is divided into two paths. In the first case, oxygen is generated directly from MO. In the second case, MOOH is formed by combination with MO and OH⁻, which step releases an electron. Then, MOOH recombines with OH⁻ to return to active site (M), producing water molecule and oxygen [75, 76]. Totally, water oxidation in alkaline conditions produces oxygen from 4OH⁻. In order to improve the overall OER catalytic activity, it is necessary to understand in detail the interaction between the active site of catalysts surface and the OER intermediate [77].

Where ΔG_i is the Gibbs free energy of reaction step i . Each reaction step involves the transfer of one electron implying that the change in free energy at each step depends on the potential.

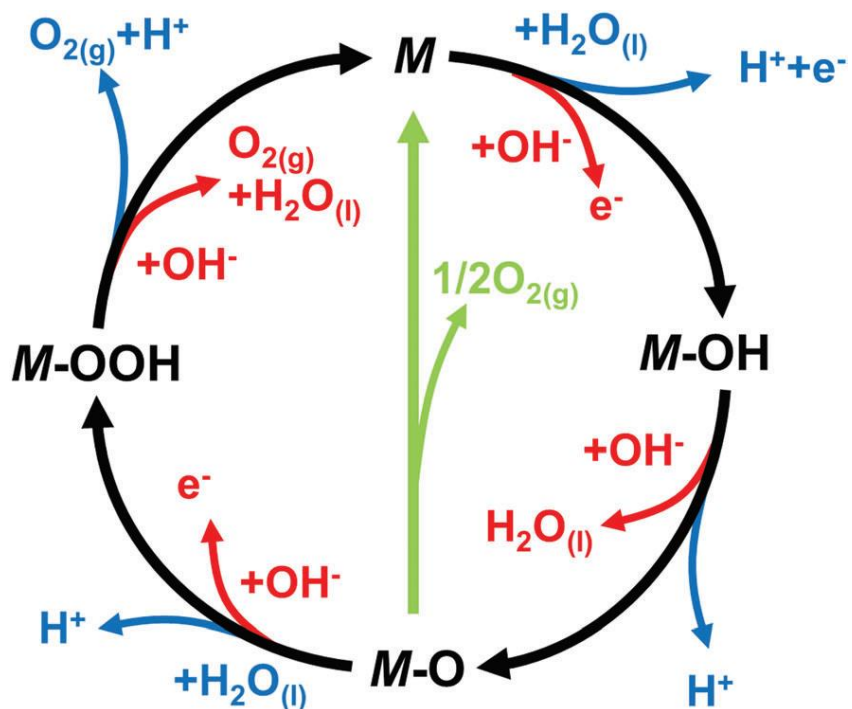


Figure 2.9 Schematic of OER mechanism in acid (blue line) and alkaline (red line) electrolyte. The black line shows that oxygen evolution involves the intermediates. The green line shows another path in OER [9].

Chapter 2: Theoretical Background

Additionally, although each mechanism is described under both conditions, such as acidic, alkaline conditions, of OER for water oxidation, thermodynamic or DFT calculation is usually reported under acidic conditions due to the simplicity of proton. However, these calculation methods are independent of pH because the free energy estimated by changes in the same way as pH [85]. In this theoretical reaction step, the Gibbs free energy of each elementary step, surface intermediates, are calculated as a function of potential, such as Nernst equation. The reaction energy of each reaction step was derived by the difference of ΔG_i of intermediates before and after reaction [74, 86]. As shown in Figure 2.10, the schematic diagram of reaction free energy diagrams is plotted for determine of thermodynamically spontaneous step [74]. The vertical axis shows Gibbs free energy, and the horizontal axis indicates reaction species and intermediates of OER, whose reaction coordinate moves from free water on the left to free oxygen on the right. For a general electrocatalysts, the Gibbs free energy of each reaction step could differ since there are irregular factors in the adsorption energy of each intermediate species, such as M, MO, MOH, and MOOH [78]. Every related step of OER must be thermodynamically unfavorable at below the reversible potential due to $E_l - E^0 = \eta < 0$, with $\Delta G_i > 0$. If the applied potential is increased, the Gibbs free energy of the intermediates shifts toward negative value. At the same time, the corresponding reaction step is thermodynamically favorable reaction due to $E_{2,3} - E^0 = \eta \geq 0$, with $\Delta G_i \leq 0$. Additionally, the corresponding RDS, overall Gibbs free energy of the OER, is known as the reaction step with the highest free energy, which is expressed as eqn (2.30) [78].

$$\Delta G_{OER} = \max [\Delta G_1, \Delta G_2, \Delta G_3, \Delta G_4] \quad (2.30)$$

Chapter 2: Theoretical Background

In this context, the overpotential in terms of thermodynamics is an additional potential applied by the rate determining step, which is expressed by eqn (2.31).

$$\eta_{OER} = \Delta G_{OER} / q - E_{eq} \quad (2.30)$$

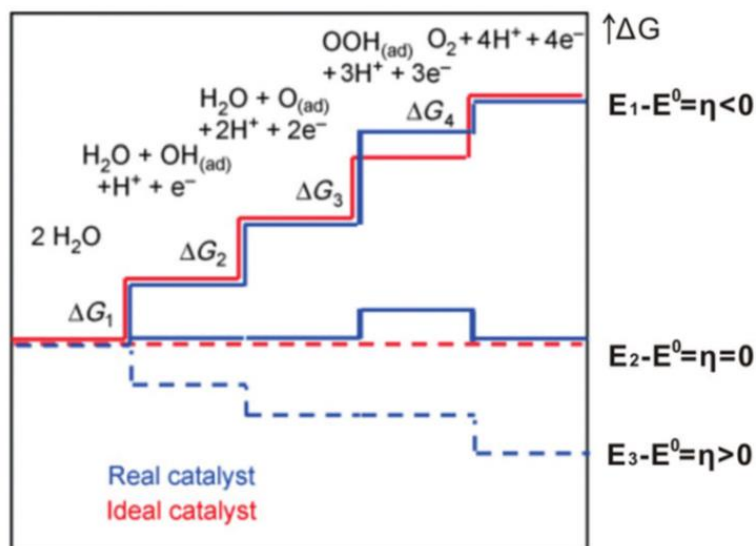


Figure 2.10 Plot of thermodynamically calculated Gibbs free energy of intermediates during OER according to the reaction coordinate. Dashed line indicate the energetics at the electrode potential where all the thermochemical barriers disappear [74, 78].

2.2.2. Summary of OER electrocatalysts and performances

Over the past decades, many researches have been conducted from the kinetics and mechanistic perspectives to overcome the limitation of kinetically hindered process, OER. Various rational designed electrocatalysts have been reported, such as changing the RDS by controlling the Gibbs free energy of each step introduced above. Despite these efforts, accurate classification was difficult until DFT calculation was applied through physicochemical property of descriptor. In particular, the volcano plot is one of the most representative heterogeneous electrocatalysis categories [168]. As shown in Figure 2.11, representative format of volcano plot is presented. The most successful descriptors typically describe the interaction between the intermediate of the main reaction and the surface of catalyst. In Figure 2.11, it represents the overpotential change according to the descriptors. For most catalysts, including electrocatalysts, reactants and products should not be too adsorbed or desorbed too well, because the catalyst fails to activate the reactants or the products fail to dissociate. Thus, as depicted in Figure 2.11, when there is proper interaction, it shows the best catalytic activity. The volcano plot can be drawn through the difference of Gibbs free energy as shown in Figure 2.10. By combining Gibbs free energy corresponding to descriptors of candidates of heterogeneous electrocatalysts for OER of water splitting and overpotential corresponding to activity, it is possible to fit a volcano plot capable of easily comparing the water oxidation trends. Figure 2.12 is drawn through this method [32].

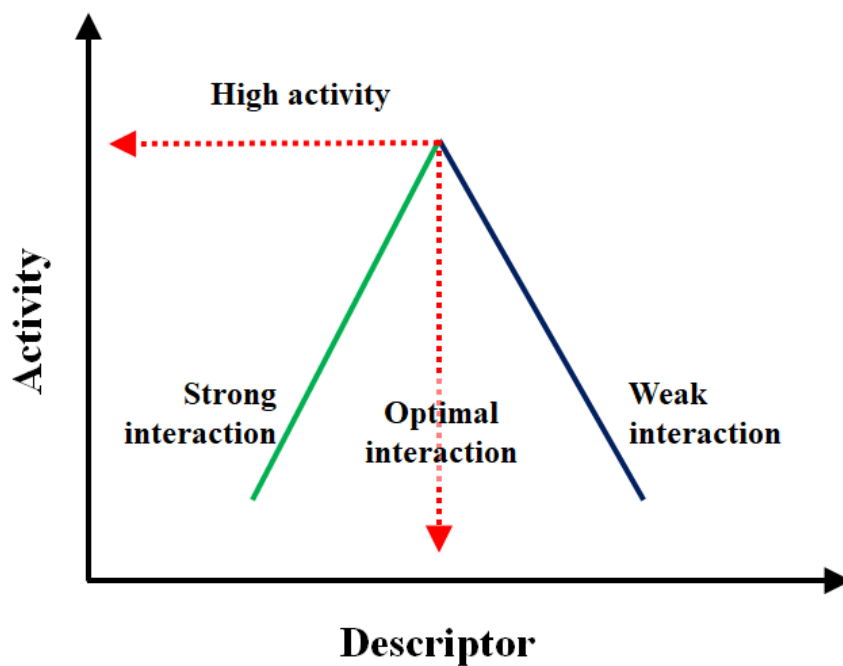


Figure 2.11 Schematic of format of the simple volcano plot. The descriptor, such as difference of Gibbs free energy between intermediates, versus the activity.

Chapter 2: Theoretical Background

The Figure 2.12 shows the volcano plot of candidates of the heterogeneous electrocatalysts for water oxidation. The X-axis of graph is difference of the Gibbs free energy of intermediates, which are MO and MOH. The Y-axis of graph is overpotential of electrocatalysts. As shown in the descriptor of Figure 2.12, difference of Gibbs free energy of intermediates is often used. Recently, this can be obtained through binding energy calculation through DFT calculation.

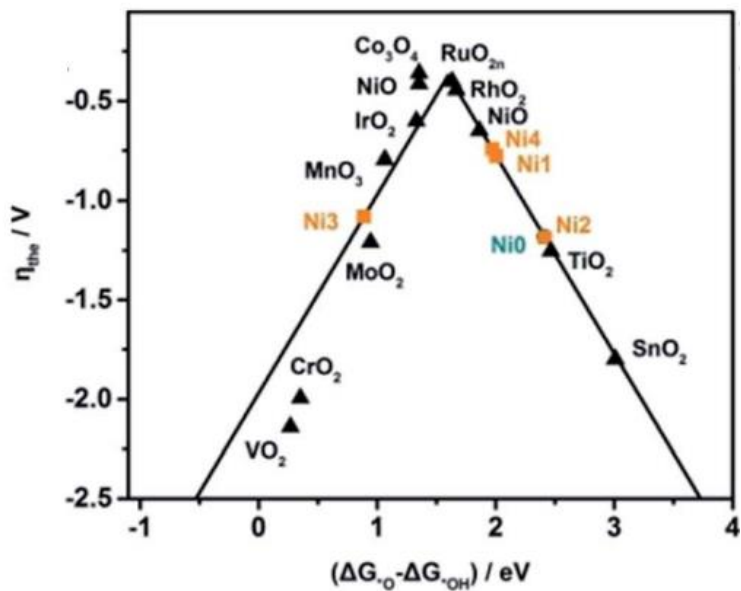


Figure 2.12 The volcano plots for heterogeneous electrocatalysts for water oxidation [32, 87].

Chapter 2: Theoretical Background

To design the electrocatalysts of enhanced catalytic activity for water oxidation, it is useful to compare their electrocatalytic performances, which have been widely studied in the past. The Table 2.1 shows electrocatalytic performances in the alkaline condition, 1.0 M KOH or NaOH, of water oxidation for various materials [7].

Table 2.1 Comparison of OER catalytic activity with previous reports of transition metal compounds.

Catalyst	Overpotential	Current density	Tafel slopes	Ref.
MOF-driven CoS ₂	298 mV	10 mA cm ⁻²	94 mV dec ⁻¹	Current work [7]
Galox-B:NiFe LDH	229	10	57	Current work
CoS ₂ microboxes	308	10	41.4	[88]
Porous (Ni _{0.33} Co _{0.67})S ₂	295	100	78	[23]
Pt-CoS ₂	300	10	58	[89]
Co@NC, (core-shell)	330	10	43.9	[90]

Chapter 2: Theoretical Background

Co-Mo-Nitride	294	10	57	[91]
NiCoP/C nanoboxes	330	10	96	[92]
Co/CoP	340	10	79.5	[93]
Au@CoS _x , (core-shell)	345	10	138	[94]
CoZn-Se	320	10	66	[95]
Co, N doped porous carbon nanosheet	350	10	83	[96]
2D nonlayered NiSe	290	10	77.1	[97]
Co(S _{0.71} Se _{0.29}) ₂ in carbon fiber	307	10	67.5	[98]
CoS ₂ in carbon fiber	386	10	81.4	[98]
NiFe LDH nanosheet	300	10	40	[55]
NiFeOOH	270	80	28	[99]

Chapter 2: Theoretical Background

NiFe LDH	280	30	50	[8]
NiFe LDH	224	10	53	[100]
NiFe LDH/CNT	247	10	31	[29]
EG/Co _{0.85} Se/NiFe LDH	270	150	57	[30]
NiFe LDH nanosheet@DG10	210	10	52	[101]
NiFe LDH	300	10	36	[102]
NiFeCr LDH	225	25	69	[6]
NiFe-WO ₄ -LDH (FNP)	290	10	41	[47]
Single atom-Au/NiFe LDH	237	10	36	[63]

2.3. Electrochemical hydrogen evolution reaction (HER)

The HER of water splitting was conducted in cathode, which is reduction electrode. The reduction of water is a counter reaction of OER of water splitting. In other words, the HER is the half reaction of the water splitting. Like the OER in the previous section, the HER also does not need to consider competitive reactions because HER is only one product, hydrogen. Thus, in water splitting, lowering the overpotential is one of the best ways to increase efficiency. HER can also predict electrocatalysts activity by calculation binding energy between catalyst surface and reactants through DFT calculation. The HER is a relatively simple reaction with fewer steps compared to OER.

As shown in Figure 2.13, this graph displays a basic HER performance curves in white box. Because of kinetics, the HER generated at the cathode should be applied with a potential negatively greater than 0.0 V. If this is replaced with the overpotential which is the performance factor of HER, it is $\eta = E_c - E_{eq}$, and as previously mentioned, the overpotential at 10 mA cm⁻² is typically used.

In this section, the detailed mechanism and theory for the hydrogen evolution of water splitting are reviewed. Furthermore, the trends and performances in electrocatalytic activity of HER for water splitting according to the suggested descriptors are described.

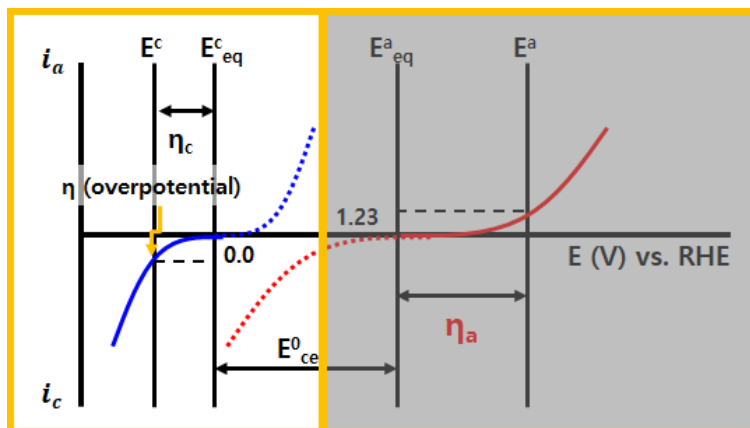
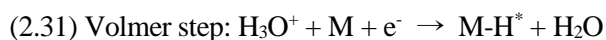


Figure 2.13 Polarization curves for hydrogen evolution in cathode.

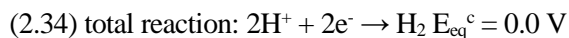
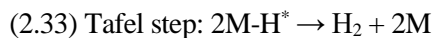
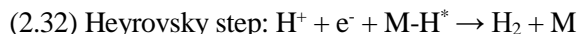
2.3.1. Theory of electrochemical HER

In terms of a mechanistic analysis of the HER for water splitting, whose major obstacle is the binding energy between surface and reactant, unlike OER. In addition, as briefly mentioned above, the mechanism of water splitting varies depending on the conditions of the electrolyte, such as neutral, acidic, alkaline conditions.

Over the past few decades, many research groups have suggested possible mechanism of HER for water splitting in acidic or alkaline condition. The mechanism most likely to proposed is the one shown in Figure 2.14 [103]. Under the both conditions, alkaline and acidic conditions, $M-H^*$ is commonly produced as intermediates. The eqn (2.31) to eqn (2.34) represent the mechanism in acidic conditions. It was described by adding M, active sites on the surface electrode, to the aforementioned mechanism.

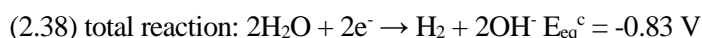
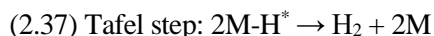
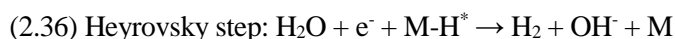
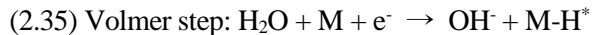


Chapter 2: Theoretical Background



As shown in the left of Figure 2.14, first, when H^+ from electrolyte and electron from external circuit are absorbed at the active site M of the surface, one M-H^* and one water molecule are generated. Next, it is divided into two paths. In first case, the formed M-H^* meets H^+ and electron to form H_2 and return to M. In second case, hydrogen is generated directly from 2M-H^* . Totally, HER in acidic medium produces hydrogen from 2H^+ .

The eqn (2.35) to eqn (2.38) represent the mechanism in alkaline conditions.



Hydrogen is produced as a final product according to the steps described above. Firstly, H_2O and electron are reacted with M, the active site of electrocatalyst, to form OH^- and M-H^* . Next, it is divided into two paths. In the first case, the formed M-H^* again combines with H_2O and electron to generate hydrogen and form OH^- and return to M. In the second case, hydrogen is generated directly from 2M-H^* . Totally, HER in alkaline medium produces hydrogen from H_2O .

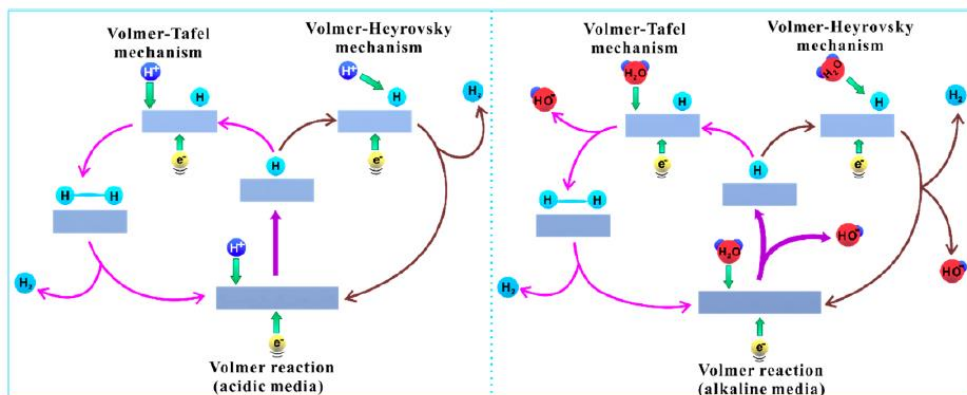


Figure 2.14 Schematic of mechanism of hydrogen evolution in acidic (left) and alkaline (right) electrolyte [103].

Each step of HER, Volmer, Heyrovsky, and Tafel step, is also called electrochemical hydrogen adsorption, electrochemical desorption, and chemical desorption [103]. In addition, the Tafel slope can be calculated through the equation derived above for each step in alkaline condition [104].

$$(2.39) \text{ Volmer step: } 120 \text{ mV dec}^{-1}$$

$$(2.40) \text{ Heyrovsky step: } 40 \text{ mV dec}^{-1}$$

$$(2.41) \text{ Tafel step: } 30 \text{ mV dec}^{-1}$$

Therefore, the Tafel plot can be plotted through the polarization curve of each electrocatalyst, and the Tafel slope can be calculated to know the step when HER is in progress.

2.3.2. Summary of HER electrocatalysts and performances

Like the OER, many researches have been conducted from the kinetics and mechanistic perspectives to overcome the limitation of HER. Various rational designed electrocatalysts have been reported. Despite these efforts, accurate classification was difficult until DFT calculation was applied through physicochemical property of descriptor. The OER is a complex and slow because it is a kinetically hindered process, whereas HER is relatively simple and has few descriptors. It is generally calculated through the binding energy of hydrogen and active site (M) [28, 34, 105].

In particular, the volcano plot is one of the most representative heterogeneous electrocatalysis categories [28]. As shown in Figure 2.15(a), representative format of volcano plot in HER is presented. The most successful descriptors typically describe the binding energy between the hydrogen and the surface of catalyst [28, 105]. In Figure 2.15(a), it represents the current density change according to the descriptors, binding energy. Like the OER, for most catalysts, including electrocatalysts, reactants and products should not be too adsorbed or desorbed too well, because the catalyst fails to activate the reactants or the products fail to dissociate. By combining Gibbs free energy corresponding to descriptors of candidates of heterogeneous electrocatalysts for HER of water splitting and current density corresponding to activity, it is possible to fit a volcano plot capable of easily comparing the HER trends. Figure 2.15(b) is drawn through this method [28, 105].

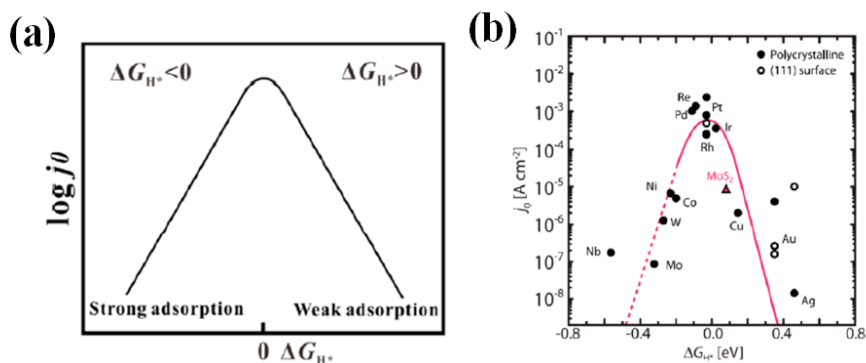


Figure 2.15 (a) Relationship between $\log j_0$ and ΔG_{H^*} under the Langmuir adsorption model [105]. (b) The volcano plots for heterogeneous electrocatalysts for HER of water splitting [28].

To design the electrocatalysts of enhanced catalytic activity for HER, it is useful to compare their electrocatalytic performances, which have been widely studied in the past. The Table 2.2 shows electrocatalytic performances in the alkaline condition, 1.0 M KOH or NaOH, of HER for various materials [7].

Table 2.2 Comparison of HER catalytic activity with previous reports of transition metal compounds.

Catalyst	Overpotential	Current density	Tafel slopes	Ref.
MOF-driven CoS ₂	-196 mV	-10 mA cm ⁻²	113 mV dec ⁻¹	Current work [7]

Chapter 2: Theoretical Background

Porous (Ni _{0.33} Co _{0.67})S ₂	-334	-100	127	[23]
Co/CoP	-253	-10	73.8	[93]
CoS ₂ -TiO ₂	-198	-10	55	[3]
Carbon tubes / Cobalt sulfide	-190	-10	131	[106]
NiS ₂ hollow microsphere	-219	-10	157	[107]
Ni _{0.7} Fe _{0.3} S ₂ microflowers	-155	-10	109	[108]
2D nonlayered NiSe	-177	-10	58.2	[97]
Co(S _{0.71} Se _{0.29}) ₂ in carbon fiber	-122	-10	85.7	[98]
CoS ₂ in carbon fiber	-233	-10	150.2	[98]
FeS ₂ /C nanoparticles	-202	-10	98	[70]

2.4. Electrochemical oxidation methods

The electrochemical oxidation is a method of controlling oxidation number through an electrochemical reaction, unlike heat treatment in an oxygen atmosphere. By setting the potential through the Nernst equation mentioned above sections, it is possible to confirm the change in the oxidation number and phase accordingly. For example, as shown in the Figure 2.16, the Pourbaix diagram shows the phase change according to the electrolyte conditions and applied potential [62, 169]. Since the electrochemical oxidation is performed through an electrochemical reaction, the basic configuration is the same as that of the electrochemical cell.

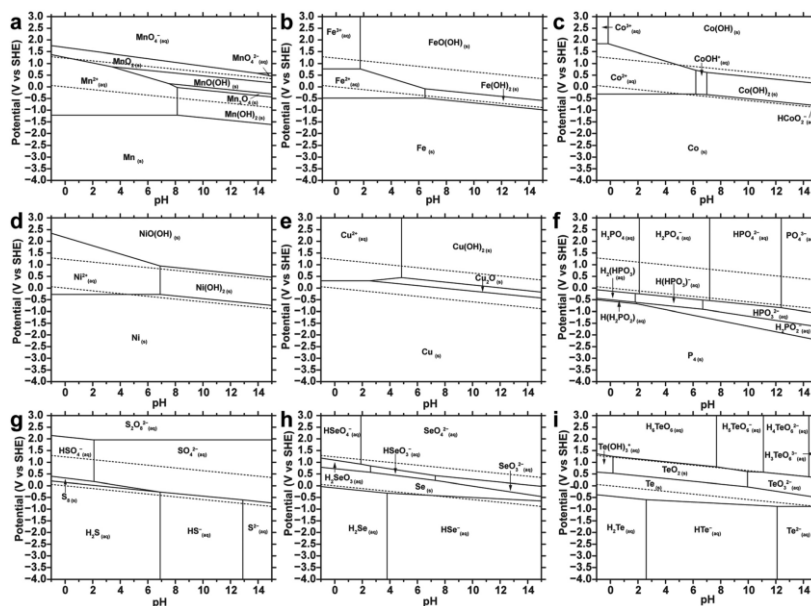


Figure 2.16 The Pourbaix diagrams for (a) Mn, (b) Fe, (c) HCoO₂⁻, (d) Ni, (e) Cu, (f) P, (g) S, (h) Se, and (i) Te species under 298 K [62, 169].

In general, there are two types of electrochemical oxidation methods, and depending on the method of applying current or voltage, it can be divided into cyclic voltammetry method and galvanostatic method.

2.4.1. Cyclic voltammetry method

As shown in Figure 2.17(a), diagram of cyclic voltammetry method, which is conventionally used method [109-111]. This method is continuously repeating positive and negative scans within a specified potential range. However, there are some demerits in this method. The repeated negative sweeps can result in dissolution and precipitation, resulting in loss of active materials [112, 113]. Additionally, thermodynamic prediction through Pourbaix diagram is difficult.

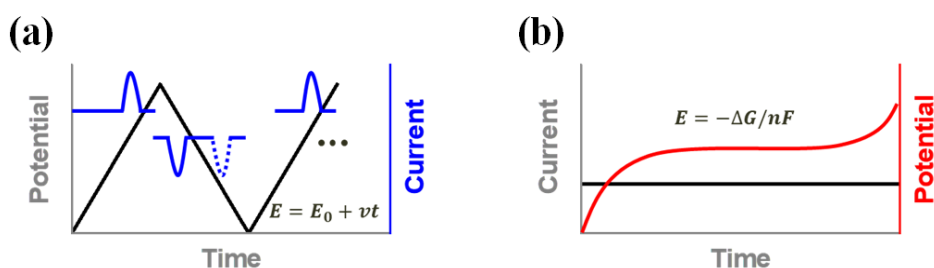


Figure 2.17 Schematic profiles of (a) cyclic voltammetry and (b) galvanostatic methods.

2.4.2. Galvanostatic method

As shown in Figure 2.17(b), profile diagram of galvanostatic method, which is oxidation or reduction dominant method. It is a reaction in which oxidation or reduction occurs continuously. Thus, the loss of active materials is relatively negligible and the maintenance of the electrocatalyst structure is relatively easy unlike cyclic voltammetry method [114-116].

2.5. Water splitting cell configuration

In the past few years, studies on large-area application for mass production of electrochemical water splitting have been reported. In order to examine the activity of the electrocatalysts, it is a priority that a laboratory scale should be conducted, but large-scale, including membrane system, is also important, because when applied in a large area, other issues may occur. As shown in Figure 2.18, full-cell of two-electrode, which consists of cathode and anode, is a cell configuration that is the first step for large-scale application [33]. In this part, the importance of the bifunctional electrocatalysts where the two electrodes are the same is emphasized, and the comparison of recently reported performance under alkaline condition, including 1.0 M KOH or NaOH, is shown in Table 2.3.

As shown in Figure 2.19, it is schematic diagrams of large-scale application in industry of water splitting system [74, 117]. These systems cover currents of at least hundreds to thousands of mA. The Figure 2.19(a) is industrial alkaline electrochemical water splitting, which is most basic large-scale applied water splitting. The Figure 2.19(b, c) are membrane electrode assembly (MEA) based electrochemical water splitting. The Figure 2.19(b) is a proton exchange membrane (PEM) system where proton is a carrier ion, and an acidic solution is used as the electrolyte. The Figure 2.19(c) is an anion exchange membrane (AEM) system where anion, such as OH^- , is a carrier ion, and an alkaline solution is used as the electrolyte.

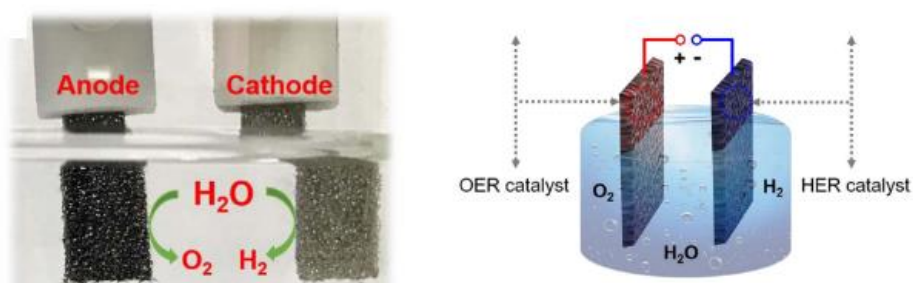


Figure 2.18 Image and schematic diagram of two-electrode full-cell system [33].

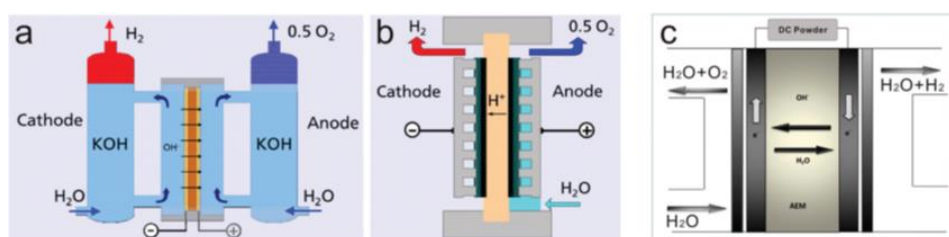


Figure 2.19 Schematics of (a) industrial alkaline water electrolysis, (b) proton exchange membrane (PEM), and (c) anion exchange membrane (AEM) electrolysis [74, 117].

Table 2.3 Comparison of overall water splitting performances with previous reports.

Catalyst	Voltage (V)	Current density	Ref.
MOF-driven CoS ₂	1.65 V	10 mA cm ⁻²	Current work [7]
Porous (Ni _{0.33} Co _{0.67})S ₂	1.57	10	[23]

Chapter 2: Theoretical Background

Carbon tubes / Cobalt sulfide	1.743	10	[106]
Ni _{0.7} Fe _{0.3} S ₂ microflowers	1.625	10	[108]
2D nonlayered NiSe	1.69	10	[97]
Co(S _{0.71} Se _{0.29}) ₂ in carbon fiber	1.63	10	[98]
FeS ₂ /C nanoparticles	1.72	10	[70]
TiO ₂ @Co ₉ S ₈ array	1.56	10	[118]
Co ₉ S ₈ array	1.71	10	[118]
Porous NiFe/NiCo ₂ O ₄	1.67	10	[119]

CHAPTER 3

Experimental Procedures

3.1. Sample Preparation

3.1.1. Fabrication of NiFe LDH based electrocatalysts

The NiFe LDH was used as a starting material before boronization. This starting material was synthesized using conventional hydrothermal. First, nickel, iron base precursors were dissolved in DI water and vigorously stirred for 30 min. The molarity of each precursor is 50 mM of nickel nitrate hexahydrate, 9 mM of iron sulfate heptahydrate, 250 mM of ammonium fluoride, and 625 mM of urea, respectively. All precursors for synthesis were bought by Sigma-Aldrich. The prepared solution with Ni foam (Sigma-Aldrich) was sealed in a Teflon-lined stainless steel autoclave, which was heated at 120 °C for 18 hours in dry oven. Second, boronization step was conducted through annealing with boron source. The three pieces of NiFe LDH, synthesized through hydrothermal, and 3 g of boric acid (Sigma-Aldrich) were loaded in a tube furnace. Then, the furnace was thermally treated under 30 sccm Ar gas flow at 350 °C for 3 hours at a ramp rate of 5 °C min⁻¹. Finally, the boronized NiFe LDH was

Chapter 3: Experimental Procedures

electrochemically oxidized through galvanostatic method using potentiostat (ZIVE MP2A, Wonatech, Korea). The galvanostatic oxidation at constant current density of 10 mA cm^{-2} for 12 hours was conducted through conventional three-electrode cell under 1.0 M KOH (Sigma-Aldrich). The three-electrode cell consists of B:NiFe LDH of working electrode, Pt foil of counter electrode, and standard calomel electrode (SCE) of reference electrode, respectively. The total fabrication steps were indicated in Figure 3.1.

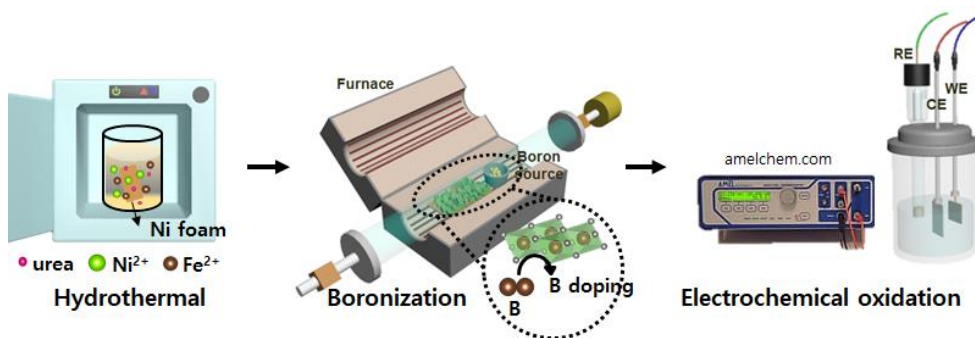


Figure 3.1 Schematic illustration of the fabrication process, including the hydrothermal, boronization, and electrochemical oxidation, of NiFe LDH based electrocatalysts.

3.1.2. Fabrication of CoS₂ based electrocatalysts

(*This section self-cites reference [7])

First, the cobalt Prussian blue analogues (Co-PBAs), one of the MOFs, was used as a starting material before sulfurization. The Co-PBAs were synthesized through a simple precipitation method. Two type solutions were prepared. All solutes were purchased by Sigma-Aldrich. Type 1 solution consists of 30 mM cobalt acetate and 17 mM sodium citrate in DI water. Potassium hexacyanocobaltate (III) was dissolved in DI water for type 2 solution. Then, type 1 solution was dropwise added into type 2 solution through syringe pump at 400 mL/hr and vigorous stirring for 10 minutes, and mixed solution was aged for 18 hours at room temperature. The dispersed precipitate was filtered through vacuum pump and washed with DI water several times to remove residues. Subsequently, obtained powder, Co-PBAs, was dried in dry oven at 60 °C, 12 hours.

Second, the Co-PBAs were thermally treated with sulfur for fabrication of cobalt sulfide. The 30 mg of Co-PBAs with thermodynamic calculated amounts of sulfur was loaded in 5 mL glass ampoule. The sealed ampoule after sulfurization was displayed in Figure 3.2. According to the amounts of sulfur, the phase of synthesized cobalt sulfide was different. After that, prepared ampoule was sealed through vacuum pump under 0.1 Torr for control of oxygen. The sealed ampoule was thermally treated using tube furnace at a 500 °C, above boiling point of sulfur, 2 hours and ramping rate of 5 °C min⁻¹. Finally, to investigate the electrochemical performance of the fabricated cobalt sulfides, such as Co, Co₉S₈, CoS₂, electrodes were prepared. The 4 mg of synthesized cobalt sulfide nanoparticles were dispersed in a mixture of 800 µL of DI water, 200 µL of EtOH (Sigma-Aldrich), and 80 µL of Nafion (Sigma-Aldrich) and sonicating for 30 min. The 5 µL of mixed ink was coated on Ni foam (Sigma-Aldrich) by drop casting using micropipette. The coated

Chapter 3: Experimental Procedures

electrodes were dried in dry oven at 60 °C, 12 hours. The total fabrication steps were indicated in Figure 3.3.



Figure 3.2 Image of sealed glass ampoule. Co-PBAs and sulfur powder were inserted, and the pressure inside was maintained 0.1 Torr.

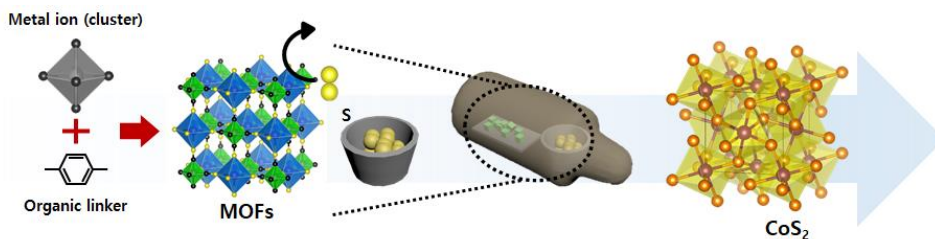


Figure 3.3 Schematic illustration of the fabrication process, including the sulfurization, of MOF-driven cobalt sulfide electrocatalysts.

3.2. Thermodynamic calculation

In NiFe LDH based electrocatalysts, the binary phase diagram of nickel-boron system was used as an indicator to determine boron doping and boron formation. Furthermore, an appropriate boron sources was found through boronization with NiFe LDH according to the boron source, such as boric acid, sodium borohydride. All databases were used through thermochemical database program (FactsageTM). In MOF-driven cobalt sulfide electrocatalysts, the ternary phase diagram, and analysis graphs of expected products depending on amounts of sulfur were drawn with FactsageTM. In both cases, the used database in this work was FACT pure substances database (FactPS).

3.3. Electrochemical analysis

In NiFe LDH based electrocatalysts, the polarization curves of each electrode were performed under same configuration as the electrochemical oxidation step. The potential range of linear sweep voltammetry (LSV) was 1.1 to 1.8 V (vs. reversible hydrogen electrode (RHE)) with a scan rate 1.0 mV s^{-1} . To examine the active surface area, the ECSA was conducted through cyclic voltammetry (CV). The potential range of CV was 0.18 to 0.28 V (vs. RHE) at a scan rate of 5, 10, 25, 50, 100, 200, 400, 600, 800, and 1000 mV s^{-1} . The linear slope and ECSA were calculated by plotting J_a - J_c at 0.23 V (vs. RHE) depending on scan rates. To verify the charge transfer effect, potentiostat electrochemical impedance spectroscopy (PEIS) was conducted within a frequency range from 100,000 Hz to 0.01 Hz at a constant voltage. The evolved gas was analyzed through gas chromatography (Micro GC Fusion gas analyzer, INFICON) during stability test at constant current density.

In MOF-driven cobalt sulfide electrocatalysts, the polarization curves of each electrode were performed under same configuration as the NiFe LDH based electrocatalysts. The conditions of electrochemical analysis of MOF-driven cobalt sulfides are the same as NiFe LDH based electrocatalysts, only LSV conditions are different. The LSV was conducted in the potential range between 1.2 and 1.8 V (vs. RHE) at a scan rate of 1.0 mV s^{-1} in OER, between -0.4 and 0.0 V at a scan rate of 5.0 mV s^{-1} in HER. In the case of overall water splitting, two-electrode system, both electrodes were prepared electrodes using potential range between 0.0 and 2.0 V at a scan rate of 5.0 mV s^{-1} .

3.4. Morphological and Phase analysis

In both cases, to analyze phase of synthesized electrocatalyst, X-ray diffraction analysis (XRD, New D8 Advances, Bruker) was performed through Cu K α radiation. The microstructure, including size and morphologies of synthesized electrocatalysts, and energy dispersive X-ray spectrometry (EDS) were observed using a field-emission scanning electron microscope (FE-SEM, SIGMA & MERLIN COMPACT, Carl Zeiss). To further verify the microstructure analysis of both cases, transmission electron microscope (TEM, JEM-2100F, JEOL Ltd.) analysis was performed. In TEM analysis, the fast Fourier transformation (FFT), selected area electron diffraction (SAED) patterns and EDS mapping images were obtained.

3.5. Physical and chemical analysis

The specific surface area was conducted using a Brunauer-Emmett-Teller (BET) analyzer with N₂ gas adsorption/desorption at a 77.3 K (ASAP 2420, Micromeritics Instruments). The chemical spectra characterization was performed through Raman spectroscopy (LabRAM HR Evolution, HORIBA), Fourier transformation infrared (FT-IR, Nicolet 6700, Thermo Scientific), and X-ray photoelectron spectroscopy (XPS). The source of ICP-AES (OPTIMA 8300, Perkin-Elmer, USA) was Ar plasma 6000 K. The spectral range was 167 ~ 782 nm.

CHAPTER 4

Fabrication of B doped NiFe LDH with Galvanostatic Oxidation

4.1. Introduction

Recently, demand for hydrogen energy, which is eco-friendly and clean energy source, is rapidly increasing, due to depletion of fossil fuels. In particular, hydrogen production through electrochemical water splitting, which is called green hydrogen, is one of the promising solutions to solve this problem. The OER is one of the two electrodes that make up electrochemical water splitting [24, 25]. However, the OER has some issues mentioned in the previous chapter [7, 9]. Solving these issues could increase the overall efficiency of water splitting [7, 17].

The objective of Chapter 4 of this thesis is to enhance the oxygen evolution electrocatalytic performance through heteroatom doping and activation. For investigation of thermally driven heteroatom doping and activation of electrocatalysts, a variety of characterization were performed. In this study, structural design of electrocatalysts is conducted to facilitate charge transfer.

4.2. Fabrication of boron doped NiFe LDH

To perform the OER for effective electrochemical water oxidation, structural design of the electrocatalysts and controlling its intrinsic conductivity and charge transfer is essential. Thus, in this section, the process of heteroatom doping for effective OER catalyst synthesis and process for improving active site are discussed.

4.2.1. Optimization of boron sources for boronization

To increase the OER performance of LDHs in lately previous studies, the active sites of LDHs have been improved to affect partial charge transfer through various transition metal combinations, such as Ni, Fe, Mn, V, Cr, etc. in LDHs [6, 47, 120-124]. Another strategy is heterogeneous element doping in LDH to adjust the electronic structure for conductivity or improved charge transfer resistance and improved active sites of electrocatalysts [43, 125, 126].

In general, heteroatom doping through boron has been reported to have a positive effect on OER performance. When boron is doped into Ni metal, activation occurs relatively compared to pristine Ni metal that does not have boron doping after OER operation, which can be confirmed by an increase in NiOOH after OER [59]. Additionally, due to boron doping, intrinsic conductivity changes and charge transfer is affected [60].

However, the boiling point and melting point of boron are high, about 3,000 °C, 2,000 °C, respectively. The previously reported, above-mentioned, boronization process for boron doping requires a high temperature of about 800 °C, although it is not necessary to the temperature as much as the boiling and melting point [59, 60]. The

Chapter 4: Fabrication of B doped NiFe LDH with Galvanostatic Oxidation

doping heteroatoms such as boron, sulfur, nitrogen, is a necessary step to improve OER electrocatalytic activity, but this high temperature can be problems for large-scale applications for future mass production. Thus, it is needed to find a more efficient heteroatom doping method and a boron source that can replace the original boron.

Herein, efficient OER electrocatalyst of hierarchically designed structure to facilitate charge transfer is suggested using gas-solid boronization and electrochemical oxidation. The strategy for designing the efficient water oxidation electrocatalysts is depicted in Figure 4.1. First, nickel iron LDH (NiFe LDH) was synthesized using the simple hydrothermal method. Second, boron doped NiFe LDH (B:NiFe LDH) was fabricated through boronization step, which was conducted through annealing of NiFe LDH and boron source. The boronization should be easy to synthesize, in order to applying to mass production. The boronization was performed more simply through boron source with a relatively low boiling point.

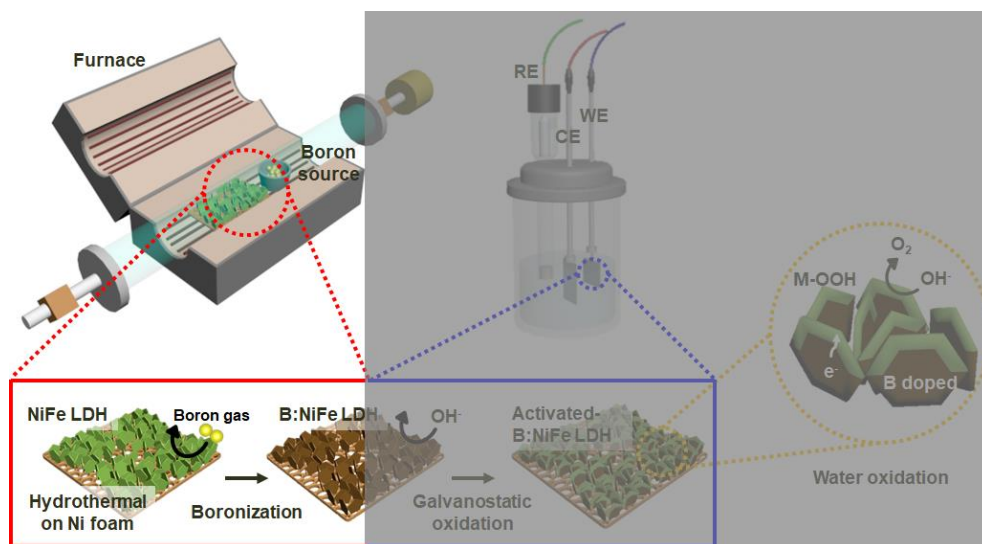


Figure 4.1 Schematic of synthesis of first step, boronization except for gray box, of electrocatalysts for efficient water oxidation.

Chapter 4: Fabrication of B doped NiFe LDH with Galvanostatic Oxidation

The starting material for synthesis of electrocatalysts is NiFe LDH. As mentioned above, it is one of the attractive materials as a water oxidation electrocatalysts. To synthesized NiFe LDH on nickel foam, it was fabricated through a simple hydrothermal method. The hydrothermal is a simple process that can produce a continuous nanostructure on various substrate or non-substrate. Depending on substrate types, it is beneficial of securing the charge transfer of electron, which is effect on electrocatalysts performance. Additionally, hydrothermal is a simple process that does not require a binder to attach the synthesized nanostructure to the substrate and can be applied to a large area. Particularly, the advantage of not having a binder is that an electrochemically inactive material is not added, so that an active material can be added as much as the inactive material does not enter. Also, the reason why nickel foam is used as a substrate is that it is a highly porous substrate, so the surface area of the electrode can be large and conductivity is high, which is advantageous for charge transfer.

The hydrothermal process for fabrication of NiFe LDH based electrocatalysts is as follows. First, each precursor was dissolved in DI water (50 mL) and stirred for 30 minutes. The mole concentration of nickel nitrate hexahydrate ($\text{Ni}(\text{NO}_3)_2 \cdot 6\text{H}_2\text{O}$), iron sulfate heptahydrate ($\text{FeSO}_4 \cdot 7\text{H}_2\text{O}$), ammonium fluoride (NH_4F), and urea (NH_2CONH_2) was 50 mM, 9 mM, 250 mM, and 625 mM, respectively. The prepared solution with nickel foam was sealed in a Teflon-lined stainless steel autoclave. Then, the autoclave was heated at 120 °C for 18 hours using dry oven.

Next, before proceeding with boronization, it is necessary to find a suitable boron sources to replace boron. The precursor containing boron is the candidate groups, such as boric acid (H_3BO_3), sodium borohydride (NaBH_4), triphenylborane ($(\text{C}_6\text{H}_5)_3\text{B}$). Among them, boric acid has relatively low boiling point and melting point compared with other boron based precursor, which are approximately 300 °C and 170.9 °C,

Chapter 4: Fabrication of B doped NiFe LDH with Galvanostatic Oxidation

respectively. Therefore, boric acid can be considered as one of the best boron precursors for doping boron in NiFe LDH at relatively low temperatures.

Additionally, in order to be able to do boron doping, it is necessary to find a condition that does not form a transition metal compound, that is, transition metal boride, with Ni and Fe, transition metals, of NiFe LDH [13].

As shown in Figure 4.2, in the phase diagram of nickel and boron system, the reaction in the area of nickel boride should not proceed for boron doping [170]. When the reaction proceeds under the conditions of the corresponding area, nickel boride is formed. The extrinsic heteroatom doping can be made when boronization is performed through heat treatment in a condition in which transition metal boride is not formed [127, 128].

Thus, boronization was performed at a temperature higher than the boiling point of the selected boron source, boric acid, but much lower than the temperature at which general boronization proceeds. In this work, boronization was conducted at a relatively low temperature of approximately 350 °C, resulting in successful boron doping in NiFe LDH, which is called B:NiFe LDH in this work.

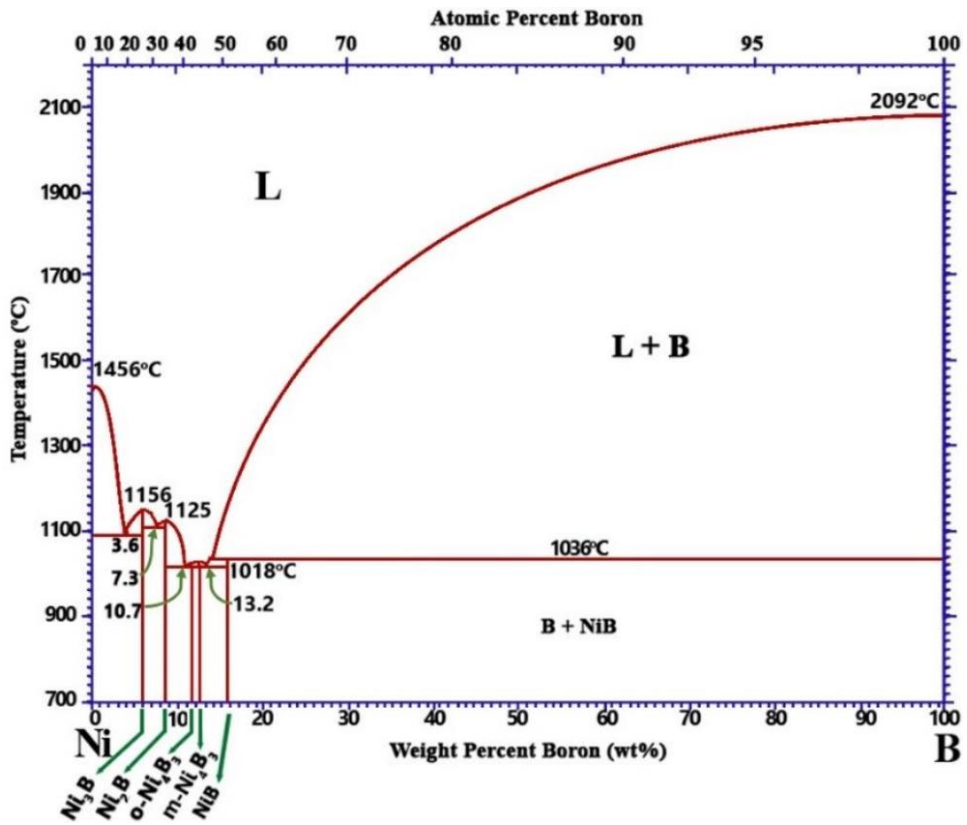


Figure 4.2 Phase diagram of Ni-B system [170].

4.3. Electrochemical oxidation of boron doped NiFe LDH

To perform the OER for effective electrochemical water oxidation, structural design of the electrocatalysts and controlling its active sites are essential. If heteroatom doping was performed for the intrinsic conductivity and facile charge transfer in the previous section 4.2, after that step, electrochemical oxidation was conducted to improve the active site and activate electrocatalysts. Thus, in this section, the process of electrochemical oxidation for effective OER catalyst for improving active site are discussed.

4.3.1. Optimization of electrochemical oxidation

To increase the OER performance of LDHs in lately previous studies, the active sites of LDHs have been improved through electrochemically oxidize using activation step. In particular, it has been reported that when boron doping, active site changes occur and this phenomenon has a positive effect on OER catalytic performance [53-55, 129]. In addition, it is important to increase the ratio of oxyhydroxide because transition metal oxyhydroxide has a higher OER activity than hydroxide constituting LDH [61]. The related electrochemical performance changes will be discussed in the next chapter, and the optimization process of electrochemical oxidation are discussed.

In this context, it has been reported about activation of transition metal compounds, including oxides, carbides, sulfides, oxyhydroxides, in OER, anodic, conditions or conversion of transition metal compounds to oxyhydroxides, so-called pre-catalysts [62]. In particular, elements used for heteroatom doping such as metallic, non-metallic, and metalloid, may be electrochemically unstable in an aqueous electrolyte [130, 169].

Chapter 4: Fabrication of B doped NiFe LDH with Galvanostatic Oxidation

According to the researches related to this, when irreversible *in-situ* electrochemical conversion under oxidation conditions was performed [131, 132], the properties of OER electrocatalysts were reported to be superior to non-activated LDH [133, 134].

Herein, efficient OER electrocatalyst of hierarchically designed structure to enhance the active sites is suggested using electrochemical oxidation of boron doped NiFe LDH. The strategy for designing the efficient water oxidation electrocatalysts is depicted in Figure 4.3. After the boronization, formation of B:NiFe LDH, electrochemical oxidation is conducted for improvement of active sites, which is applicable to large-scale because *in-situ* conversion with all electrochemical cell configurations in the same state. The boron doped NiFe LDH with electrochemical oxidation confirmed that oxyhydroxides were formed on the surface, which showed better OER electrocatalytic performance than directly synthesized NiFe LDH due to facile charge transfer structure and improved active sites of B:NiFe LDH and pristine NiFe LDH.

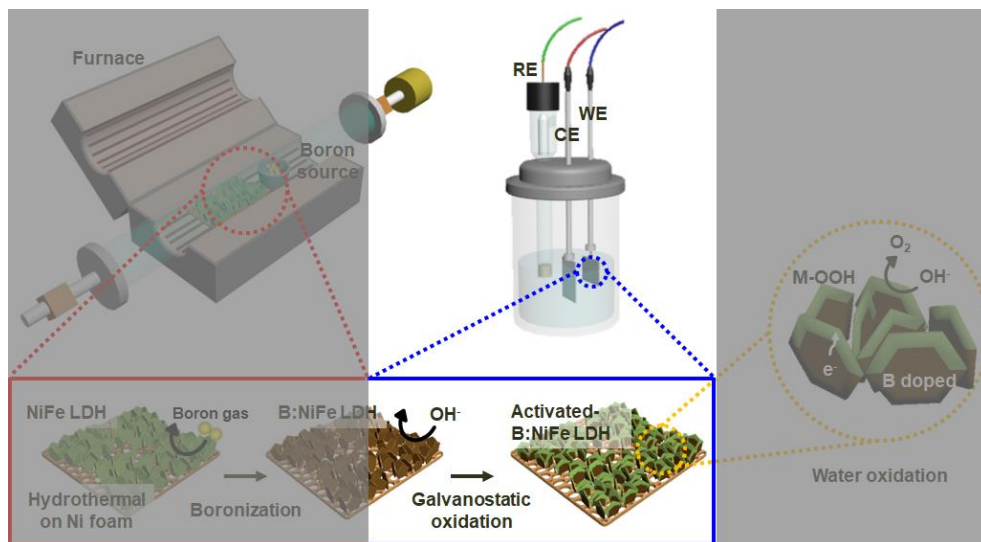


Figure 4.3 Schematic of synthesis of second step, electrochemical oxidation except for gray box, of electrocatalysts for efficient water oxidation.

Chapter 4: Fabrication of B doped NiFe LDH with Galvanostatic Oxidation

The starting material for electrochemical oxidation of electrocatalysts is B:NiFe LDH. As mentioned above, although boron doped NiFe LDH is one of the attractive materials as a water oxidation electrocatalysts, activation through electrochemical oxidation can change the active sites and improve it with more efficient water oxidation electrocatalysts. The electrochemical oxidation is one of the methods that can control the oxidation number or the phase control without heat treatment. In particular, this oxidation method is advantageous because it can be converted to *in-situ* in an electrochemical cell configuration. Additionally, by controlling the OER conditions, the target material of the working electrode can be oxidized to MO, MOH, MOOH, MO₂, etc [135].

As described previous chapter, there are two types of electrochemical oxidation. The first type is a method of oxidizing by applying alternating positive scan and negative scan by cyclic voltammetry. The second type is a galvanostatic or potentiostatic method that applies a constant current or constant voltage. This method can continuously maintain an oxidizing or reducing atmosphere [115].

The electrochemical oxidation process for increasing ratio of oxyhydroxide is as follows. The electrochemical oxidation of B:NiFe LDH is conducted by galvanostatic method at constant current density 0.1 mA cm⁻² for 12 hours using general electrochemical analyzer through conventional three-electrode electrochemical cell system under 1.0 M KOH. To set the parameter of galvanostatic oxidation to 0.1 mA cm⁻², the following process was performed. First, the position of the target phase is confirmed through the Pourbaix diagram in Figure 4.4, and the appropriate conditions were found. The current density corresponding to the appropriate potential is found under the alkaline conditions, the electrolyte [62].

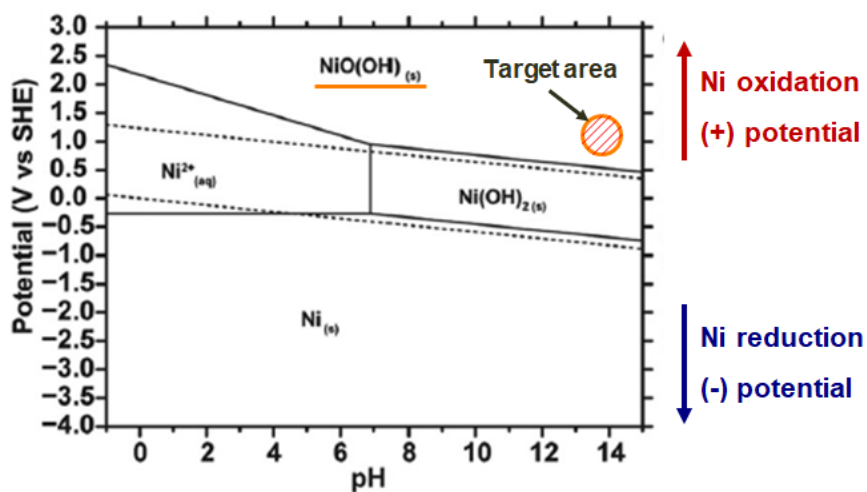


Figure 4.4 Pourbaix diagram of nickel system according to the pH. Redraw the ref [62].

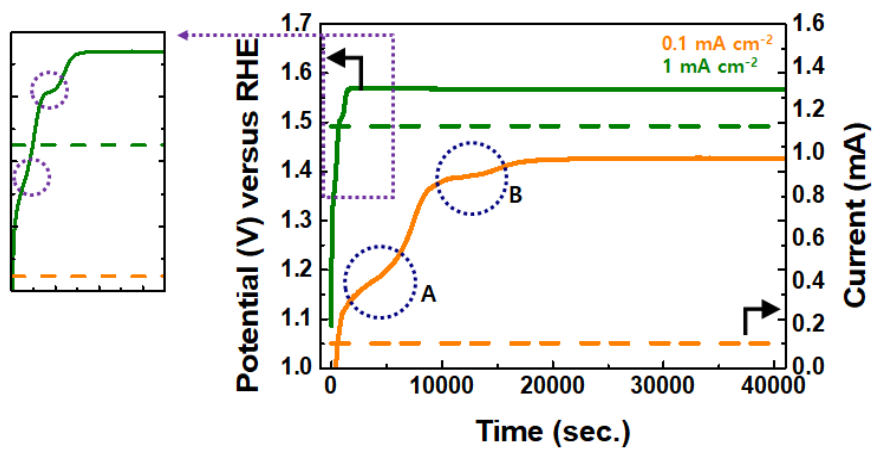


Figure 4.5 The potential profile of the galox-B:NiFe LDH during galvanostatic oxidation at 0.1 and 1.0 mA cm^{-2} over 12 hours.

Chapter 4: Fabrication of B doped NiFe LDH with Galvanostatic Oxidation

Galvanostatic oxidation, electrochemical oxidation using galvanostatic method, was compared by electrochemical oxidation through two current density conditions. As shown in Figure 4.5, the potential profiles at 0.1 and 1.0 mA cm⁻² were plotted to compare the tendency of oxidation.

The reaction step according to oxidation will be explained in the next section. To compare only the profile tendency, there is a difference in the time when the potential stabilizes after oxidation. It was confirmed that B:NiFe LDH with a current density of 1.0 mA cm⁻² stabilized in a faster time than B:NiFe LDH with 0.1 mA cm⁻².

4.3.2. Reaction step of electrochemical oxidation

In Figure 4.5, the potential profiles of galvanostatic oxidation of B:NiFe LDH was depicted. As shown in the potential profile, two plateaus can be identified regardless of the current density, 0.1, 1.0 mA cm⁻². The orange line and the green line are 0.1 and 1.0 mA cm⁻², respectively. Although plateaus are detected at different times, the overall shape is similar. The graph on the right in Figure 4.5 is an enlarged potential profile of current density 1.0 mA cm⁻². The plateau region in the chronopotentiometry curve, which shows the potential change through galvanostatic oxidation, means that an electrochemical reaction occurs [115]. In other words, the potential profile in Figure 4.5 means that two electrochemical reaction occur. With the application of a positive potential according to the positive current density, the electrochemical reaction occurring in this reaction can be regarded as oxidation. The electrochemical oxidation reaction in each plateau is equal to eqn (4.1) and eqn (4.2) [136]. In Figure 4.5, A is the eqn (4.1) reaction and B is the eqn (4.2) reaction.

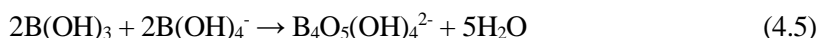


Therefore, even if the current density is different, in the Pourbaix diagram of Figure 4.4, if the corresponding conditions are within the same area, the same electrochemical reaction is shown. As can be seen from these results of potential profile, the difference in current density can be seen as the difference in the rate related kinetics of electrochemical reaction. The potential profile shows the oxidation of the two plateaus to oxyhydroxide at the top of the Pourbaix diagram of Figure 4.4. Characterization to

Chapter 4: Fabrication of B doped NiFe LDH with Galvanostatic Oxidation

analyze this will be discussed in the next section.

Additionally, J. Masa et al. reported that following electrochemical oxidation in alkaline solution when B_2O_3 of transition metal boride showed the following behavior [137]. According to the pH of aqueous solution, boron based species are reacted. First, B_2O_3 reacts with water to form boric acid as eqn (4.3). Second, B_2O_3 reacts with KOH or NaOH in alkaline solution to form metaborates or polyborates as eqn (4.4) and eqn (4.5), respectively.



Similarly, BO_x by boron doping in NiFe LDH undergoes an electrochemical oxidation to form B_2O_3 like eqn (4.6), and metaborate through eqn (4.3) and eqn (4.4).



Also, B-OH in B:NiFe LDH can form polyborates through eqn (4.5).

The contents of improvement of active sites related to these results will be further discussed in connection with the electrochemical analysis in the next chapter.

4.4. Characterization of NiFe LDH based electrocatalysts

The synthesis results of NiFe LDH through hydrothermal were confirmed. In addition, the results of boron doping in NiFe LDH through boronization were examined, and various characterizations were performed to analyze the results after electrochemical oxidation.

First, the morphology of as-prepared NiFe LDH based electrocatalysts was observed in Figure 4.6. The field emission-scanning electron microscopy (FE-SEM) analysis displays nanoplates from in all samples. Even if boronization and galvanostatic oxidation, which is one of the electrochemical oxidation through galvanostatic method, were conducted, the nanoplate structures did not any collapse, such as delamination, destruction, breaking. However, it was observed that the thickness of the nanoplates were relatively thin after heat treatment for boronization.

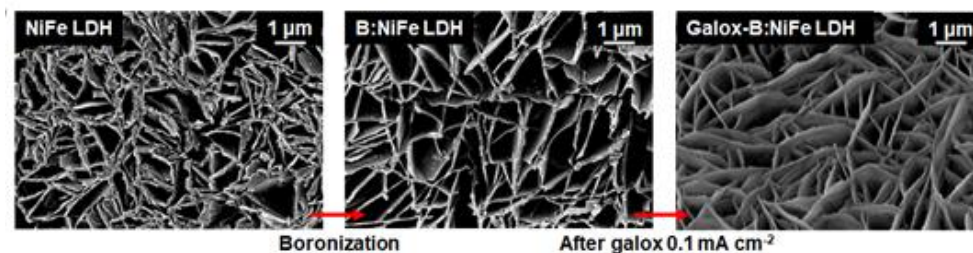


Figure 4.6 Field-emission scanning electron microscopy (FE-SEM) images of NiFe LDH based electrocatalyst under each condition.

Chapter 4: Fabrication of B doped NiFe LDH with Galvanostatic Oxidation

Second, to verify the successful boron doping in NiFe LDH, energy dispersive X-ray spectrometry (EDS) analysis was conducted. As shown in Figure 4.7, EDS analysis confirmed the distribution of boron on the surface of NiFe LDH. The intensity of boron peak was highly increased in EDS spectrum of B:NiFe LDH compared with pristine NiFe LDH (Figure 4.7(a)). In Figure 4.7(a), the blue region is B:NiFe LDH, and the red region is pristine NiFe LDH. It can be confirmed that the peak is detected in the vicinity of 0.2 keV, which is the energy adjacent to carbon. It can be seen that the intensity of the B:NiFe LDH, boron-doped sample, is high. Furthermore, the chemical composition of B:NiFe LDH was uniformly distributed over the entire surface of the Ni foam in EDS mapping results (Figure 4.7(b-f)). In Figure 4.7(b-f), each image is a scanning image for mapping B:NiFe LDH, and mapping images for Ni, Fe, B, and O, respectively. In particular, when mapping images for each element (Figure 4.7(c-f)) are compared with scanning image (Figure 4.7(b)), it can be seen that contours appear according to the structure of the NiFe LDH. In addition, it can be seen that the boron is also distributed as a whole, and thus successfully doped with NiFe LDH.

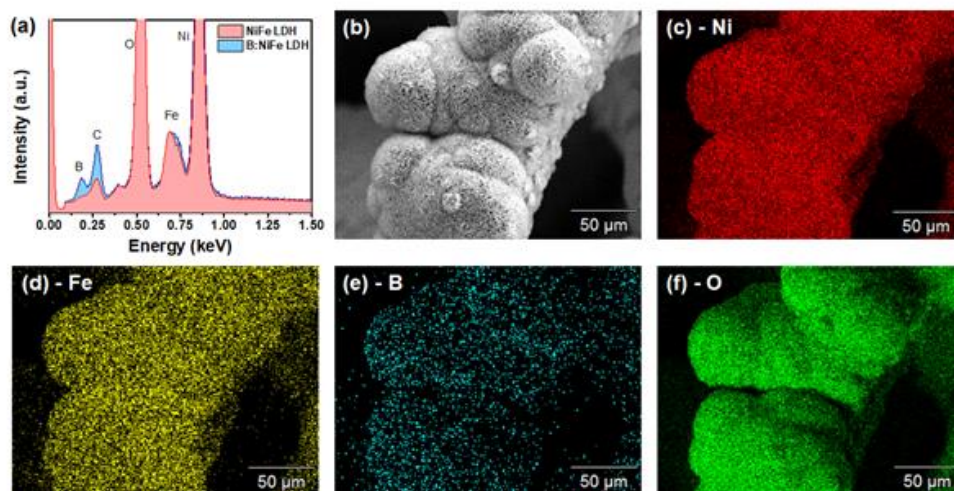


Figure 4.7 Morphological characterization of B:NiFe LDH. (a) Energy dispersive X-ray spectrometry (EDS) spectrum. (b) EDS scanning image. (c-f) EDS elemental mapping images of B:NiFe LDH. (c) Ni. (d) Fe. (e) B, and (f) O.

Chapter 4: Fabrication of B doped NiFe LDH with Galvanostatic Oxidation

To further verify the morphology and microstructure characterization, transmission electron microscopy (TEM) analysis was conducted. Figure 4.8 and Figure 4.11 show the results of microstructural characterization of NiFe LDH based electrocatalysts through TEM analysis, where the selected area electron diffraction (SAED) pattern and EDS mapping were obtained. As in the previous SEM results (Figure 4.6), no significant change in morphology was observed even when boronization and electrochemical oxidation were performed (Figure 4.8). The SAED after boronization and electrochemical oxidation was examined to pattern what is corresponding to each d-spacing. The SAED result of pristine NiFe LDH accorded with dot pattern for (101), (110), (202), (212), (033), and (220) plane of NiFe LDH. Similarly, the B:NiFe LDH, after boronization, was corresponding to pattern for same plane with pristine NiFe LDH. In both cases, hexagonal based space group was observed. Furthermore, the B:NiFe LDH after OER sweep and galox-B:NiFe LDH, B₂NiFe LDH after electrochemical oxidation, showed similar SAED patterns. As a result of Figure 4.8, even if boronization was progressed, it was confirmed that LDH was maintained without changing the lattice. Additionally, when OER sweep and electrochemical oxidation of B:NiFe LDH were conducted, it was confirmed that (oxy)hydroxides was formed. The d-spacing results of high resolution-TEM (HR-TEM) and corresponding fast Fourier transformation (FFT) of each NiFe LDH based electrocatalysts are shown in Figure 4.9. As a result of obtaining d-spacing through FFT of HR-TEM, it was confirmed that d-spacing corresponding to NiFe LDH was obtained as in SAED of Figure 4.8.

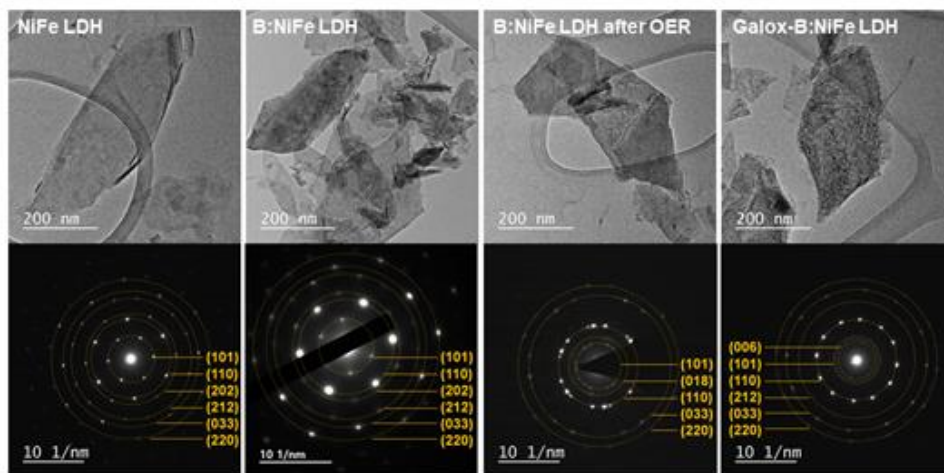


Figure 4.8 Morphological characterization of boron doped NiFe LDH (B:NiFe LDH) and B:NiFe LDH with galvanostatic oxidation (galox-B:NiFe LDH) electrocatalyst. Transmission electron microscopy (TEM) analysis (top of each row) and selected area electron diffraction (SAED) pattern (bottom of each row) of NiFe LDH based electrocatalysts under each condition.

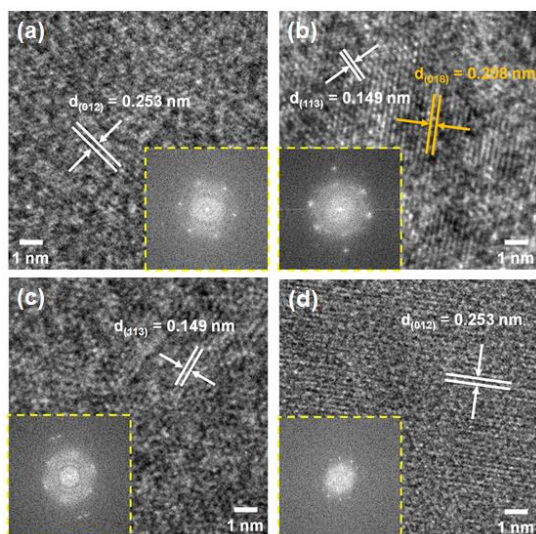


Figure 4.9 High resolution-transmission electron microscopy (HR-TEM) and fast Fourier transformation (FFT) analysis (inset) of (a) NiFe LDH, (b) B:NiFe LDH, (c) B:NiFe LDH after OER test, and (d) galox-B:NiFe LDH.

Furthermore, to verify the successful boron doping in NiFe LDH, TEM EDS through scanning TEM (STEM) analysis was conducted. As shown in Figure 4.10 and Figure 4.11, EDS analysis confirmed the distribution of boron of NiFe LDH. The STEM image and mixed EDS image of STEM image were shown in Figure 4.10(a) and (b), respectively. From the mixed EDS image, it can be seen that Ni, Fe, B, and O constituting B:NiFe LDH are distributed as a whole. The corresponding EDS mapping image (Figure 4.11) was shown that the Ni (green), Fe (yellow), B (red), and O (blue) of B:NiFe LDH were uniformly distributed.

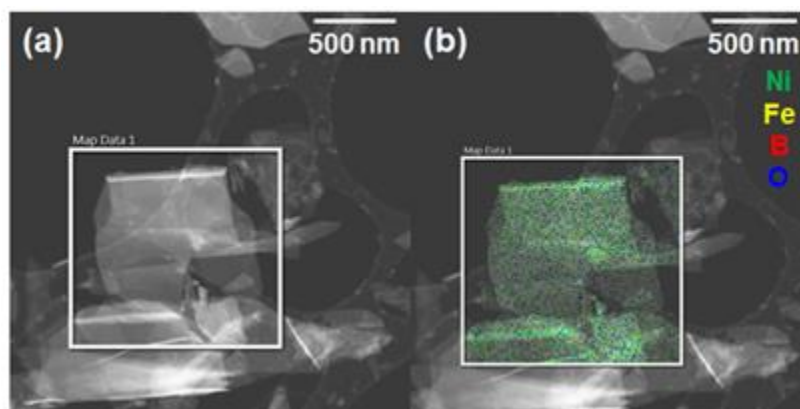


Figure 4.10 EDS of TEM through STEM analysis of B:NiFe LDH. (a) STEM image. (b) Mixed EDS image of STEM, Ni (green), Fe (yellow), B (red), and O (blue) chemical composition.

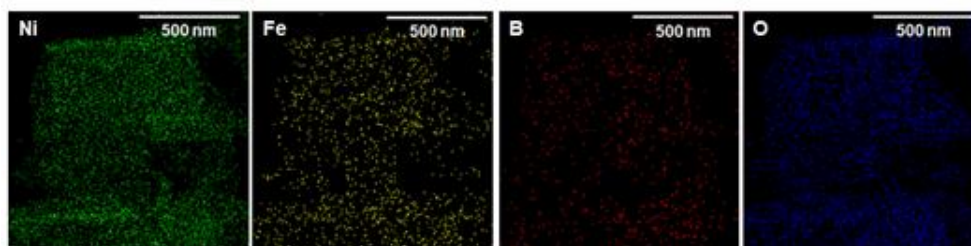


Figure 4.11 EDS of TEM through STEM analysis of B:NiFe LDH. EDS mapping of TEM images of the B:NiFe LDH composition (Ni: green, Fe: yellow, B: red, O: blue).

Chapter 4: Fabrication of B doped NiFe LDH with Galvanostatic Oxidation

To further verify the structural and bonding nature characterization of galox-B:NiFe LDH, boron doped NiFe LDH with electrochemical oxidation, compared with before boronization and electrochemical oxidation were investigated through X-ray diffraction (XRD), Raman analysis, and Fourier transformation infrared (FT-IR) (Figure 4.12).

The Figure 4.12(a) displays the phase analysis of prepared NiFe LDH based electrocatalysts after the different conditions. The red, blue, and orange line are pristine NiFe LDH, after hydrothermal, B:NiFe LDH, after boronization, galox-B:NiFe LDH, after electrochemical oxidation, respectively. The XRD pattern of pristine NiFe LDH was agreement with the reference PDF card (00-040-0215) which is NiFe LDH [43]. In the case of the B:NiFe LDH, galox-B:NiFe LDH, although the peaks except for main peak are difficult to distinguish, the main peak of LDH around 11 degrees are clear [31, 43, 55].

In order to confirm the existence of LDH in more detail, an analysis through bonding vibration was performed using Raman spectroscopy. Figure 4.12(b) shows the Raman spectroscopy of the NiFe LDH based electrocatalysts before and after boronization and electrochemical oxidation. In this Raman analysis results, the pristine nickel foam, which was not synthesized at all, was not detected any peaks. The peaks of the pristine NiFe LDH (red line) appeared at 300, 457, 531, and 650 cm^{-1} which are corresponding to the vibrations of NiFe-O [17]. Additionally, B:NiFe LDH and galox-B:NiFe LDH were similar Raman results compared with pristine NiFe LDH. The peak was detected at 477, 566 cm^{-1} , which is the peak corresponding to typical $\delta(\text{Ni}^{3+}\text{-O})$, $\nu(\text{Ni}^{3+}\text{-O})$ vibrations of $\gamma\text{-NiOOH}$ [59, 60, 63].

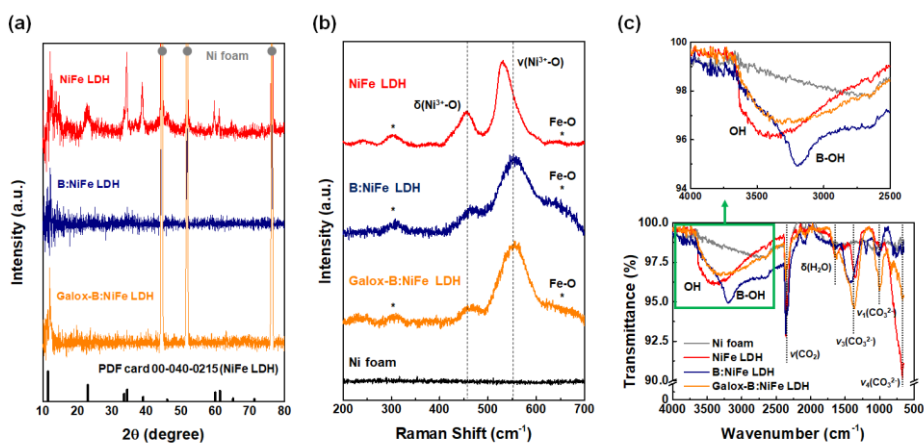


Figure 4.12 Phase characterization and chemical spectra analysis to confirm boronization and electrochemical oxidation inducement. (a) X-ray diffraction (XRD) analysis for confirmation of boronization and electrochemical oxidation. (b) Raman spectroscopy analysis for the NiFe LDH based electrocatalysts. (c) Fourier transformation infrared (FT-IR) analysis to confirm boron doping in NiFe LDH (top of (c): enlargement of FT-IR result).

As shown in the peak of vibration of crystal, the Raman results confirmed that the NiFe-O remain after gas-solid boronization and electrochemical oxidation. In other words, considering the results of the previous morphological, structural, and chemical characterization, it was confirmed that the boron was distributed through EDS, and the structure of the LDH did not collapse, confirming that the boron was successfully doped. In more detail, FT-IR analysis was performed to confirm the change in bonding by boron doping (Figure 4.12(c)).

In the full range FT-IR spectra (bottom of Figure 4.12(c)), several peaks were

Chapter 4: Fabrication of B doped NiFe LDH with Galvanostatic Oxidation

commonly detected below approximately 2500 cm^{-1} in NiFe LDH based electrocatalysts. The band spectra 1620 cm^{-1} is agreement with the vibration of water molecules ($\delta(\text{H}_2\text{O})$) [138]. As shown in band spectra between 1400 and 600 cm^{-1} , the vibration peak of CO_3^{2-} appeared in 1360 , 1000 , and 680 cm^{-1} , which are agreement with the asymmetrical bending (ν_3), the symmetrical stretching (ν_1), and the asymmetrical bending (ν_4) vibration, respectively [31, 102]. Additionally, the wavelength of 2700 , 2360 cm^{-1} is corresponding to $\text{H}_2\text{O}-\text{CO}_3^{2-}$, CO_2 , respectively in all NiFe LDH based electrocatalysts, including even nickel foam [47, 139]. Meanwhile, in all NiFe LDH based electrocatalysts except nickel foam, a broad peak represented by OH^- , hydroxide ion, was detected between 3500 and 3000 cm^{-1} , which is broad absorption spectra (top of Figure 4.12(c)). This broad spectra range is O-H stretching vibrations of the hydroxyl groups in the hydrotalcite layers and interlayer water molecules [17, 140]. Particularly, boron doped NiFe LDH detects new peaks that are not detected in other NiFe LDH based electrocatalysts. A 3201 cm^{-1} peak was detected, which is a B-OH stretching mode, according to another reference [141]. Therefore, it can be seen that the heteroatom, which is boron in this work, is successfully doped with NiFe LDH.

Chapter 4: Fabrication of B doped NiFe LDH with Galvanostatic Oxidation

To further verify the quantitative analysis and X-ray adsorption analysis of galox-B:NiFe LDH, boron doped NiFe LDH with electrochemical oxidation, compared with before boronization and electrochemical oxidation were investigated through inductively coupled plasma-atomic emission spectroscopy (ICP-AES) and X-ray absorption fine structure (XAFS).

As shown in Table 4.1, nickel and boron ratio through ICP-AES of pristine NiFe LDH and B:NiFe LDH were indicated. The source of ICP-AES (OPTIMA 8300, Perkin-Elmer, USA) was Ar plasma 6000 K. The spectral range was 167 ~ 782 nm.

Table 4.1 ICP-AES analysis for verification of chemical composition of pristine NiFe LDH and B:NiFe LDH.

Sample	Ni (ppm)	B (ppm)	Ni : B ratio
NiFe LDH	7.5×10^3	0.1	1 : 0
B:NiFe LDH	7.9×10^3	1.9×10	1 : 0.013

According to the ICP-AES results, almost negligible amount of boron was detected in pristine NiFe LDH, and approximately 1.3 at% boron was detected in B:NiFe LDH compared to nickel. The amount of nickel was measured slightly differently by the nickel foam as a substrate.

Figure 4.13 shows the XAFS results of boronization and electrochemical oxidation. Figure 4.13(a) shows the X-ray absorption near-edge structure (XANES) spectra of boronization and electrochemical oxidation. Although the XANES shape has a

difference in intensity, there is no significant difference even if the peak shift does not occur and boronization step. Additionally, Figure 4.13(b) shows the extended X-ray absorption fine structure (EXAFS) spectra of boronization and electrochemical oxidation. Prof. W. Schuhmann group reported that Ni-B bonding in Ni_xB was observed at approximately 2 Å of EXAFS [61]. Accordingly, Ni-B bonding was confirmed by boron doping in B:NiFe LDH.

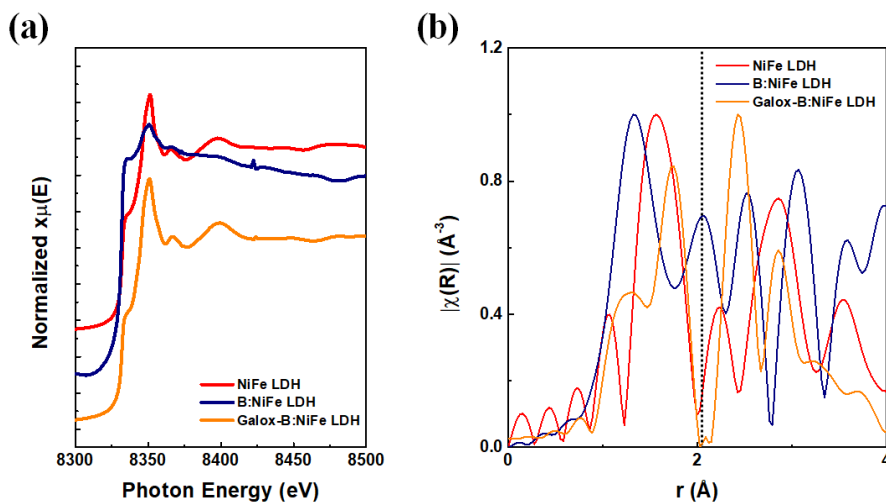


Figure 4.13 X-ray absorption fine structure (XAFS) results of NiFe LDH based electrocatalysts. (a) X-ray absorption near-edge structure (XANES) and (b) Extended X-ray absorption fine structure (EXAFS).

4.5. Summary

The boron doped nickel iron layered double hydroxide with electrochemical oxidation was fabricated through the simple hydrothermal method, gaseous boronization, and followed thermodynamically predictive electrochemical oxidation using Pourbaix diagram. The hydrothermal process is conducted by quantifying the atomic ratio of nickel and iron precursor to 4:1 to improve the catalytic performance.

Then, in order to enhance the intrinsic conductivity of NiFe LDH and facilitate the charge transfer, heteroatom, boron, was doped into NiFe LDH. As-prepared NiFe LDH through hydrothermal was thermally treated with boron source, which contains boron and has a low melting and boiling point. Therefore, boronization was performed at a much lower temperature than the previously reported boron doping methods, and successful boron doping was conducted. To demonstrate successful boron doping in NiFe LDH, analytical methods such as morphological, structural, phase, and chemical characterization were performed. We discovered the simple boronization method with low temperature using boron source.

Electrochemical oxidation was performed by applying a galvanostatic method to B:NiFe LDH. Successfully converted to oxyhydroxide through activation under the conditions in the Pourbaix diagram. In addition, the difference according to the applied current density during galvanostatic oxidation was confirmed through the potential profile. Also, a reaction scheme was suggested during electrochemical oxidation when boron was doped in NiFe LDH. In this chapter, an efficient NiFe LDH based electrocatalyst was prepared through above steps, and was proved by characterizations.

CHAPTER 5

Electrochemical Performance of NiFe LDH catalysts

5.1. Introduction

In Chapter 4, we have successfully fabricated heteroatom doped NiFe LDH, which is expected to be crucial for the enhanced water oxidation. Additionally, the hierarchical structure to adopt boron doped NiFe LDH to the anode of water splitting, which consists of electrochemically oxidized boron doped NiFe LDH is developed to improve the electrocatalytic OER performance. This is due to an increase in the proportion of oxyhydroxide through electrochemical oxidation and a change in the active site caused by doped boron.

The purpose of this chapter is to analyze the effect of boron doping in NiFe LDH on the charge transfer, as well as the effect of activation through galvanostatic oxidation on the active site of NiFe LDH. In this chapter, *ex-situ* analysis, including electrochemical analysis to explain this effect, will be discussed.

5.2. Electrochemical performances

The electrochemical performance of the NiFe LDH based electrocatalysts was investigated under alkaline electrolyte of 1.0 M KOH. As shown in Figure 5.1, to examine the oxygen evolution electrocatalytic activity of galox-B:NiFe LDH, linear sweep voltammetry (LSV) was conducted for each electrode. The oxygen evolution polarization curves, LSV of each electrode, were performed with a conventional three-electrode system in pH 14 electrolyte. The potential range of linear sweep measurements for OER was from 1.1 to 1.8 V (vs. reversible hydrogen electrode (RHE)) at a scan rate of 1.0 mV s⁻¹. As a result of polarization curves, the OER electrocatalytic activity of the NiFe LDH based electrocatalysts was measured as the overpotential at a current density of 10 mA cm⁻², which is typically used as a reference to evaluate electrocatalyst [7, 142]. In order to confirm the superiority of galox-B:NiFe LDH, it was compared with Ir foil, a noble metal most frequently used as an OER electrocatalyst. The galox-B:NiFe LDH electrocatalyst required an overpotential of 229 mV to reach 10 mA cm⁻², which is the lowest overpotential among this work. However, compared with other electrocatalysts, the overpotential of the nickel foam, which is only substrate without LDH, Ir foil, NiFe LDH, and B:NiFe LDH were 465, 371, 315, and 281 mV, respectively under the same measurement condition (top of Figure 5.2).

In particular, it was confirmed that overpotential was further improved as boronization and electrochemical oxidation through galvanostatic method of NiFe LDH and B:NiFe LDH, respectively. As shown in bottom of Figure 5.2, it shows plot of the current density at overpotential of 250 mV, which relates the solar driven hydrogen production. In order to use OER electrocatalysts with solar driven hydrogen production, an overpotential of at least 250 mV is required [114]. Thus, the current density at 250

mV of galox-B:NiFe LDH was 15.0 mA cm⁻², while the others show 0.1, 0.1, 1.9, and 4.6 mA cm⁻², respectively (nickel foam, Ir foil, NiFe LDH, and B:NiFe LDH).

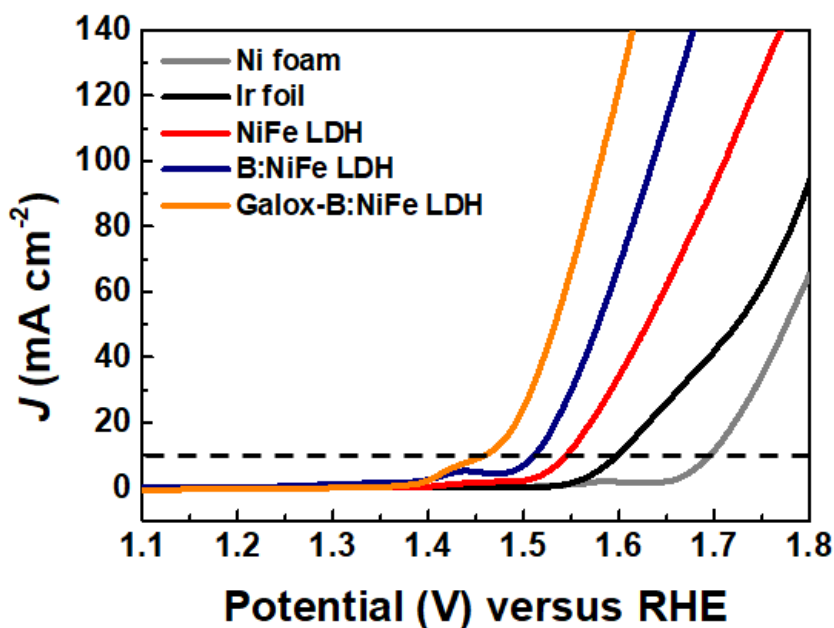


Figure 5.1 Electrochemical characterization of the electrodes of NiFe LDH based electrocatalyst for water oxidation in 1.0 M KOH. The OER polarization curves through linear sweep voltammetry (LSV) of different electrodes with a scan rate 1.0 mV s⁻¹.

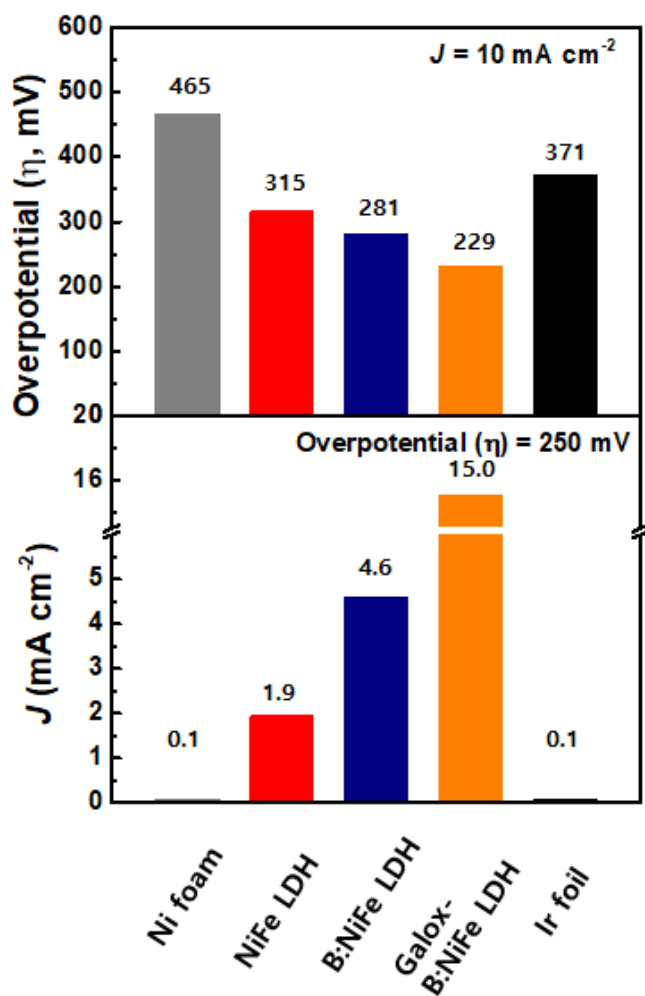


Figure 5.2 Electrochemical characterization of electrodes of NiFe LDH based electrocatalyst for OER in 1.0 M KOH. Top: overpotential of each electrode at 10 mA cm⁻² current density. Bottom: current density of each electrode at overpotential of 250 mV.

Chapter 5: Electrochemical Performance of NiFe LDH catalysts

Next, as shown in Figure 5.3, the Tafel plot was displayed for calculation of Tafel slope and to analyze the electrocatalyst reaction kinetics, which was plotted based on the potential against $\log(J)$. The galox-B:NiFe LDH shows a low Tafel slope, which is 57 mV dec^{-1} , while the others were calculated for 104, 91, 80, and 73 mV dec^{-1} , respectively (nickel foam, Ir foil, NiFe LDH, and B:NiFe LDH). In this context, reaction kinetics of the galox-B:NiFe LDH are fastest among the measured electrocatalysts, which may mean improved charge transfer through boron doped NiFe LDH and changed active sites through electrochemical oxidation.

Furthermore, as shown in Figure 5.4, the number of electron transfer steps are calculated through Butler-Volmer equation, which is described above. As a result of calculating ' n ' to consider the rate determining step, the change in ' n ' in NiFe LDH and galox-B:NiFe LDH occurs from 0.23 to 0.54, but the RDS does not change. Therefore, it was confirmed that the kinetics change occurred, but the RDS did not change. To examine the durability of the NiFe LDH based electrocatalysts, including pristine NiFe LDH, B:NiFe LDH, galox-B:NiFe LDH, a long-term durability test was conducted through the galvanostatic method, which is chronopotentiometric method in Figure 5.5, 5.6. At a constant current density of 10 mA cm^{-2} , the galox-B:NiFe LDH electrocatalyst delivered a stable overpotential of approximately 230 mV over 100 hours (Figure 5.5). Similarly, as shown in Figure 5.6, the pristine NiFe LDH and B:NiFe LDH, boron doped NiFe LDH, delivered a stable overpotential of about 320, 280 mV at 10 mA cm^{-2} , respectively (Figure 5.7).

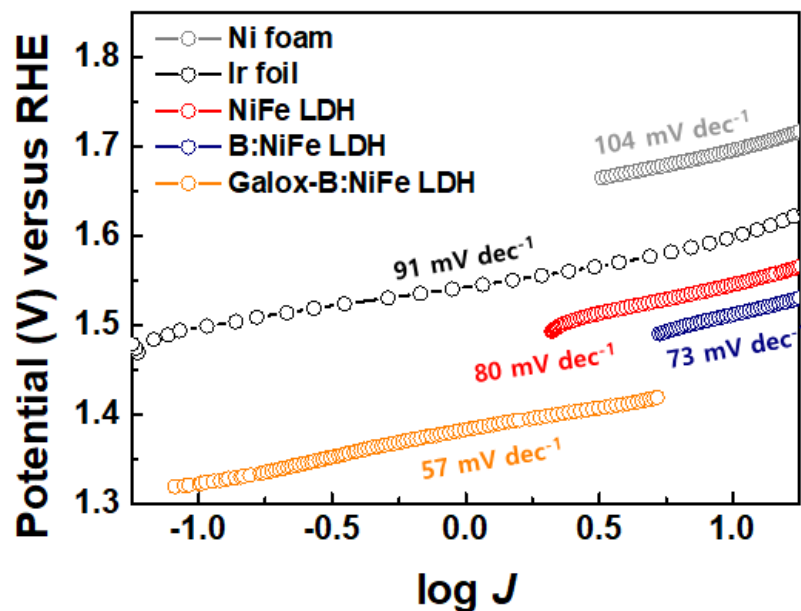


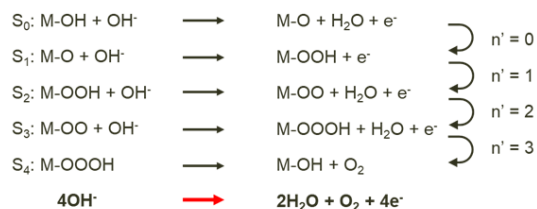
Figure 5.3 Electrochemical characterization of the electrodes of NiFe LDH based electrocatalyst for water oxidation in 1.0 M KOH. The Tafel plot for calculation of Tafel slope of each electrode corresponding to the OER polarization curves.

❖ Butler-Volmer equation

$$i = A \times i_0 \cdot \left[\exp\left(\frac{\alpha_A n F}{RT} \eta\right) - \exp\left(-\frac{\alpha_c n F}{RT} \eta\right) \right]$$

- At room temperature, Tafel slope = $(59 \text{ mV dec}^{-1}) / (n' + \alpha)$
 - n' : number of single electron transfer step prior to the determining step
 - α : symmetry / transfer coefficient (typically 0.5)

❖ OER mechanism step



- NiFe LDH: $80 \text{ mV dec}^{-1} \rightarrow n' = 0.23$
- Galox-B:NiFe LDH: $57 \text{ mV dec}^{-1} \rightarrow n' = 0.54$

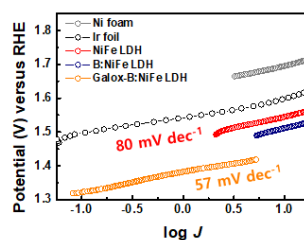


Figure 5.4 OER mechanism step through calculation of Tafel slope in typical transition metal LDH.

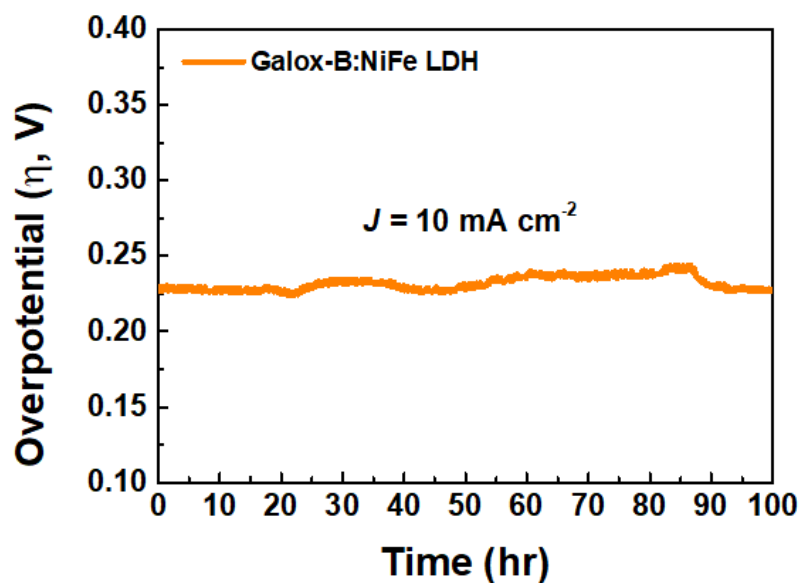


Figure 5.5 Electrochemical characterization of the electrodes of galox-B:NiFe LDH electrocatalyst for water oxidation in 1.0 M KOH. Chronopotentiometric durability test at 10 mA cm^{-2} .

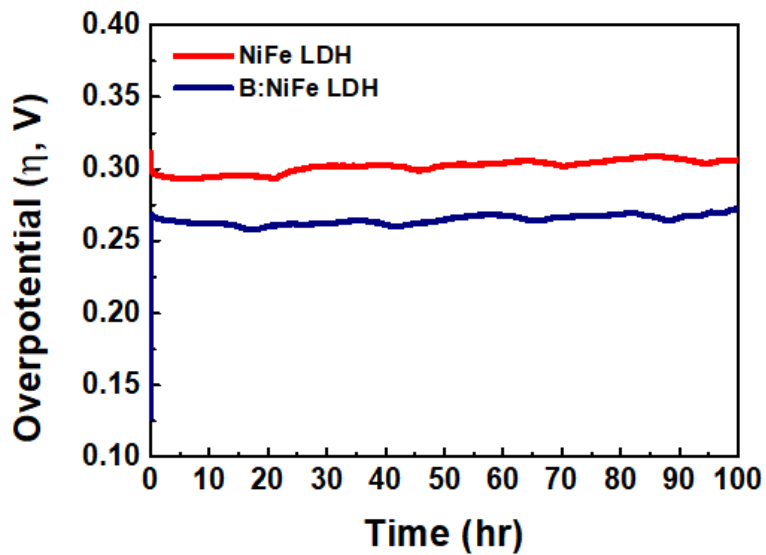


Figure 5.6 Electrochemical characterization of the electrodes of NiFe LDH, B:NiFe LDH electrocatalyst for water oxidation in 1.0 M KOH. Chronopotentiometric durability test at 10 mA cm^{-2} .

Next, it was analyzed by gas chromatography to verify the ratio and Faradaic efficiency of gas generated during the electrochemical water splitting at a constant current density. As shown in Figure 5.7, Faradaic efficiency and amount of evolved gas (O_2 , H_2), which is product of water splitting, during stability test at 10 mA cm^{-2} about the galox-B:NiFe LDH electrocatalyst. The gas generated through gas chromatography in Figure 5.8 was analyzed, and as a result, only O_2 and H_2 were generated. In addition, the Faradaic efficiency was calculated through eqn (5.1). The number of electrons required to generate oxygen was set to 4 according to eqn (5.2), and the number of electrons required to generate hydrogen was set to 2 according to eqn (5.3). The y-axis on the left in Figure 5.7, is the Faradaic efficiency of the gas generated, and the y-axis on the right is the amount of gas generated. Faradaic efficiency confirmed that the gas generated at both electrodes was maintained at 100% during the stability test at 10 mA cm^{-2} , which means that electrochemical water splitting was performed stably without reverse reactions or side reactions. In addition, when calculating the amount of gas, it was confirmed that the ratio of H_2 and O_2 was fixed to 2:1, respectively, at both electrodes consistent with the reaction formulas according to eqn (5.2), (5.3), and (5.4).

$$\text{Faradaic efficiency (FE, \%)} = \frac{Z \cdot n \cdot F}{Q} \quad (5.1)$$

Z: number of electrons for 1 mol gas, n: number of moles

F: Faraday constant, $96,500 \text{ C mol}^{-1}$, Q: passed charge



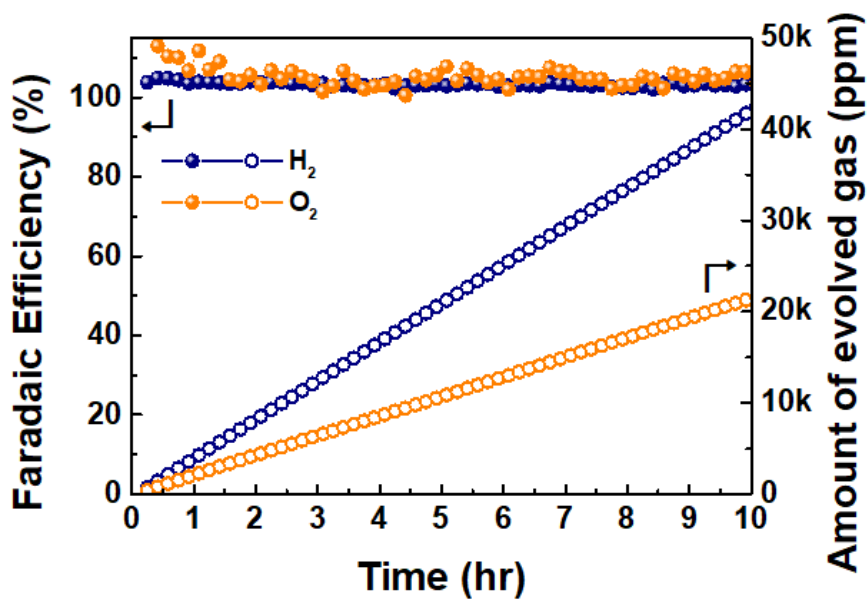


Figure 5.7 Electrochemical characterization of the electrodes of galox-B:NiFe LDH electrocatalyst for water oxidation in 1.0 M KOH. Faradaic efficiency and amount of oxygen and hydrogen during stability test of water splitting at 10 mA cm^{-2} .

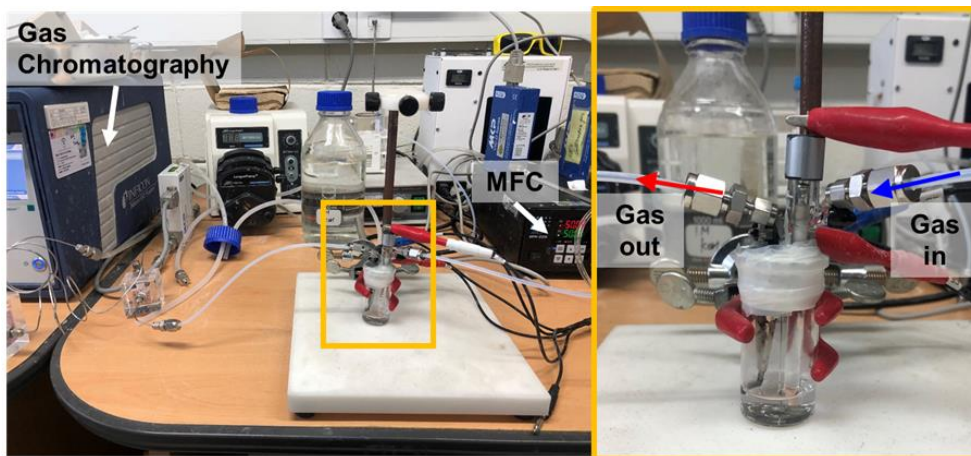


Figure 5.8 Images of equipment, gas chromatography, of evolved gas analysis during stability test of water splitting.

5.2.1. Effects of boron doping in NiFe LDH

The impedance measurements were performed to demonstrate the tendency of electrochemical characterization identified in the previous section. To further clarify the effect of the boron doped NiFe LDH for facile charge transfer during reaction steps for water oxidation, an analysis through electrochemical impedance spectroscopy (EIS) was performed in the frequency from 100,000 to 0.01 Hz at constant overpotential of 350 mV. In order to compare the charge transfer in the reaction step for oxygen evolution, EIS was measured while applying 350 mV to create a condition in which sufficient onset of each electrode had progressed. In order to quantitatively compare the charge transfer, the charge transfer resistance (R_{ct}) term of EIS was used. Figure 5.9 displays the Nyquists plot of the each electrocatalyst depending on the applied overpotential. The resistance term of plotted EIS consist of electrolyte resistance (R_e) and charge transfer resistance (R_{ct}) in Figure 5.9. Since the configuration of the electrochemical cells for measuring each electrode is all the same, the components of the EIS all the same. First, R_e refers to the position of the starting point of the semicircle in the Nyquists plot [143, 144]. The R_e is also a resistance term that occurs in an electrochemical cell, and since the components are all the same, there is no significant difference for each electrode. In the Nyquists plot, the R_{ct} is the value corresponding to the diameter of the semicircle [143, 144]. However, it can be seen that R_{ct} increases in the order of galox-B:NiFe LDH, B:NiFe LDH, and NiFe LDH regardless of the applied overpotential. The tendency of the R_{ct} of electrodes mentioned above is consistent, although the each R_{ct} value decreases when the overpotential is strongly applied. Additionally, in order to measure under the same conditions, it was measured under open circuit potential (OCP), as shown in Figure 5.9(d), because the current density are different under the certain applied overpotential

Chapter 5: Electrochemical Performance of NiFe LDH catalysts

despite of all conditions after oxygen generation. Also in this case (OCP condition), as in the previous results, it was confirmed that the tendency of R_{ct} was consistent. The R_{ct} of B:NiFe LDH electrocatalyst was lower than pristine NiFe LDH. It can be seen as a decrease in charge transfer resistance of NiFe LDH by boron doping in the B:NiFe LDH. Also, the R_{ct} of galox-B:NiFe LDH electrocatalyst was the lowest compared to the other. The effects of activation through electrochemical oxidation will be discussed in the next section.

Thus, it can be expressed as shown in Figure 5.10 by representing it through an equivalent circuit according to the Nyquists plot of Figure 5.9. Due to the decrease in R_{ct} constituting the equivalent circuit, charge transfer is facile performed in the boron doped region as shown in the schematic diagram on the right of Figure 5.10.

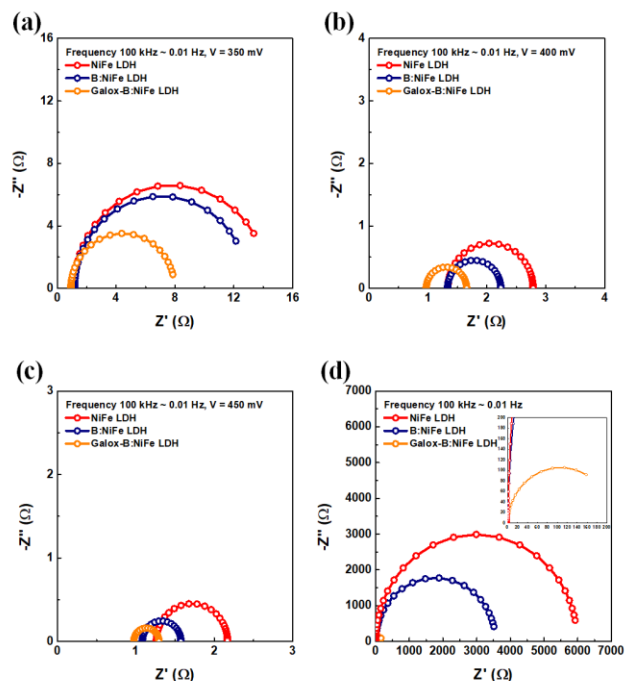


Figure 5.9 Electrochemical characterization of the electrodes of NiFe LDH based electrocatalyst for water oxidation in 1.0 M KOH. Nyquist plots through EIS at (a) 350 mV (vs. RHE) (b) 400 mV (c) 450 mV, and (d) OCP state (inset: magnification of low area) for different electrode.

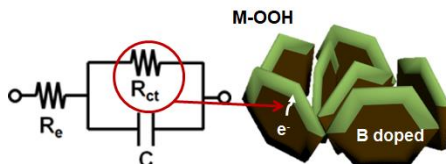


Figure 5.10 Equivalent circuit model and schematic diagram of the possibility of charge transfer in B doped NiFe LDH.

5.2.2. Effects of electrochemical oxidation

As shown in EIS results of Figure 5.9, the R_{ct} of galox-B:NiFe LDH electrocatalyst was the lowest compared to the other. This result can be seen as a change in active sites of B:NiFe LDH by electrochemical oxidation. This result means that facile charge transfer is possible as a result of forming activated oxyhydroxide on the B doped NiFe LDH through galvanostatic oxidation, which increased ratio of oxyhydroxide in NiFe LDH. According to a paper reported by D. G. Nocera group and Z. Zhu group, structural change occurs due to NiB_i formed in anodic condition. In this step, the Jahn-Teller distorted Ni (III) center is activated as a bis-oxo/bridged Ni center, which affects OER performance [54, 129].

In Figure 5.11, the characterization of surface composition was performed for confirmation of improved OER performance. The X-ray photoelectron spectroscopy (XPS) analysis was performed to confirm the increase in the ratio of oxyhydroxide in B:NiFe LDH by activation through electrochemical oxidation. Figure 5.11(a) shows the O 1s XPS result for NiFe LDH after different synthetic process. It can be confirmed that the O 1s of B:NiFe LDH shifted toward high energy compared to NiFe LDH due to O-B bonding by boron doping [145]. On the other hand, it appears that O 1s of the galox-B:NiFe LDH shifted toward low energy again, due to formation of oxyhydroxide by activation through galvanostatic oxidation. Furthermore, there is also an effect of lattice oxygen (O^{2-}) and absorbed molecular water on this shift [114]. In addition, it can be seen that the overall intensity of O 1s for XPS of galox-B:NiFe LDH is relatively increased compared to the intensity of B:NiFe LDH and NiFe LDH, because of increase of oxyhydroxide ratio.

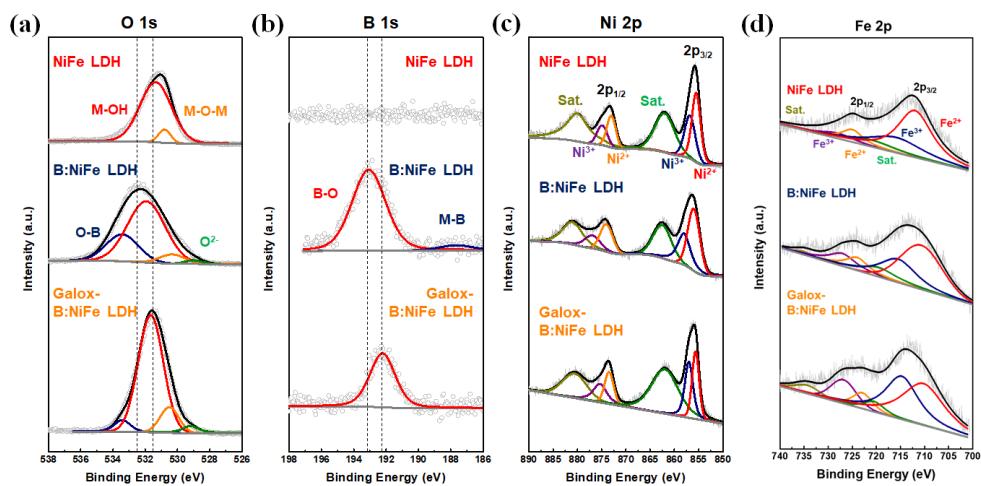


Figure 5.11 Chemical composition characterization for verification of enhanced OER electrocatalytic activity. The X-ray photoelectron spectroscopy (XPS) analysis for observation of chemical composition. (a) O 1s, (b) B 1s, (c) Ni 2p, and (d) Fe 2p of NiFe LDH based electrocatalysts under each condition.

Chapter 5: Electrochemical Performance of NiFe LDH catalysts

In Figure 5.11(b), the B 1s of XPS analysis for NiFe LDH was not detected since it did not react with the boron source, before boronization. However, the B 1s analysis for B:NiFe LDH and galox-B:NiFe LDH demonstrated the formation of boron peak. In particular, B 1s of XPS for B:NiFe LDH shows 188 eV, 193 eV which are corresponding to metal-boron (M-B) peak and surface oxidized B (B-O) peak, respectively [142]. The M-B peak (188 eV) decreases relatively when exposed to air and aqueous based electrolyte during electrochemical oxidation from XPS of the galox-B:NiFe LDH [61]. As in the O 1s trend in Figure 5.11(a), the B-O peak shifted toward low energy.

Next, the XPS results of Ni 2p were confirmed to clarify the formation of oxyhydroxide. In Figure 5.11(c), XPS analysis for Ni 2p exhibited the Ni 2p_{3/2} (855.5 (Ni²⁺) and 856.8 eV (Ni³⁺)) and Ni 2p_{1/2} (873.0 (Ni²⁺) and 874.8 eV (Ni³⁺)). The intensity of Ni³⁺ peaks of the galox-B:NiFe LDH compared with NiFe LDH, B:NiFe LDH was increased due to formation of oxyhydroxide through electrochemical oxidation using galvanostatic method [17]. The XPS analysis for Fe 2p exhibited the Fe 2p_{3/2} (710.2 (Fe²⁺) and 714.7 eV (Fe³⁺)) and Fe 2p_{1/2} (722.9 (Fe²⁺) and 726.8 eV (Fe³⁺)) in Figure 5.11(d). Similar to Ni 2p trends, the intensity of Fe³⁺ peaks of galox-B:NiFe LDH also increased in Fe 2p.

To further verify the physically analyzed surface area characterization in the NiFe LDH, B:NiFe LDH, and galox-B:NiFe LDH, Brunauer-Emmett-Teller (BET) analysis was conducted (Figure 5.12), where the N₂ adsorption and desorption plot (Figure 5.12(a)), BET specific surface area (Figure 5.12(b)), and pore distribution (Figure 5.12(c)) were obtained. In the case of galox-B:NiFe LDH, the BET specific surface area in Figure 5.12(a), (b) was 2.54 m² g⁻¹, compared with 0.02, 0.72, and 0.85 m² g⁻¹ for nickel foam, pristine NiFe LDH, and B:NiFe LDH, respectively. These BET analysis results have a similar tendency to electrochemical surface area (ECSA) in Figure 5.13, Table 5.1. To calculate ECSA, cyclic voltammetry (CV) was measured for each scan rate as shown in Figure 5.14. The ECSA was calculated as a result of plotting the difference in current density according to the scan rate. The CV was conducted in the voltage range between 0.18 and 0.28 V (vs. RHE). The linear slope was calculated by plotting ΔJ at 0.23 V (vs. RHE) depending on scan rates. The linear slope is two-fold of the double-layer capacitance (C_{dl}) [7, 144, 146, 147]. ΔJ , C_{dl} , and ECSA can be calculated following eqn (5.5), (5.6), (5.7) [5, 66, 147].

$$\Delta J = J_a - J_c \quad (5.5)$$

$$C_{dl} = 1/2 \times d(\Delta J)/dV \quad (5.6)$$

$$ECSA = C_{dl} / C_s \quad (5.7)$$

C_s is the capacitance of atomically smooth planar surface in 1.0 M KOH electrolyte ranges between 20 to 60 $\mu\text{F cm}^{-2}$. For calculation, C_s was configured at 40 $\mu\text{F cm}^{-2}$ [66].

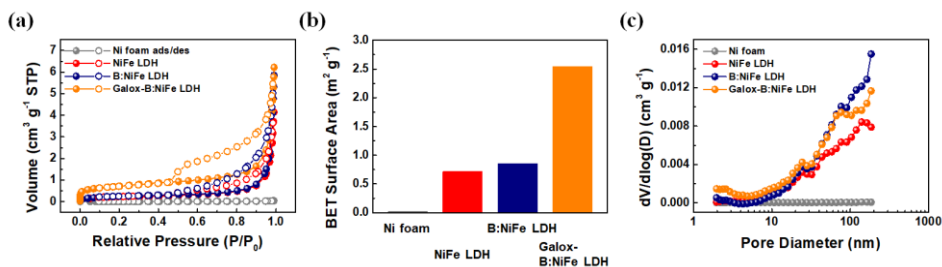


Figure 5.12 Specific surface area characterization for verification of enhanced catalytic activity. Brunauer-Emeett-Teller analysis of (a) isothermal plot with N₂ adsorption/desorption, (b) comparison of BET surface area under each condition, and (c) pore distribution.

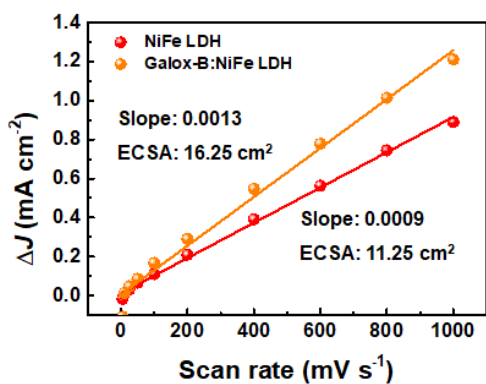


Figure 5.13 Specific surface area characterization for verification of enhanced catalytic activity. Electrochemical surface area (ECSA) of NiFe LDH based electrocatalyst. The linear slope is related to the double layer capacitance.

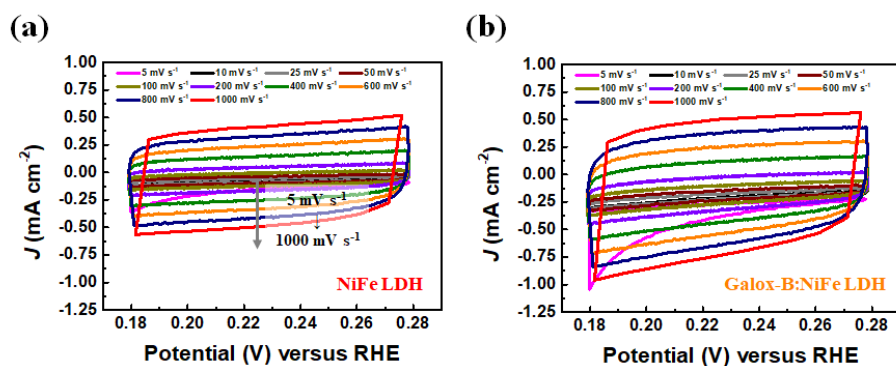


Figure 5.14 Cyclic voltammogram for measurement of ECSA of (a) NiFe LDH and (b) galox-B:NiFe LDH.

Table 5.1 Calculation of ECSA of NiFe LDH and galox-B:NiFe LDH.

Electrocatalysts	Slope	C_{dl}	ECSA
NiFe LDH on Ni foam	0.9 mF cm^{-2}	0.45 mF cm^{-2}	$11.25 \text{ cm}^2_{\text{ECSA}}$
Galox-B:NiFe LDH on Ni foam	1.3 mF cm^{-2}	0.65 mF cm^{-2}	$16.25 \text{ cm}^2_{\text{ECSA}}$

After carrying out the water oxidation stability test, post-analysis, such as XRD and FE-SEM, was conducted (Figure 5.15). As shown in Figure 5.15(a), the XRD pattern of galox-B:NiFe LDH had hardly changed after OER. In XRD pattern, NiFe LDH and KOH, electrolyte in this work, were detected. Additionally, although oxygen gas was vigorously generated during OER in surface of galox-B:NiFe LDH electrocatalyst, the galox-B:NiFe LDH well-retained on the Ni foam in SEM images (Figure 5.15(b)). In SEM results, morphology of KOH was also detected since it is the electrolyte during OER for water splitting.

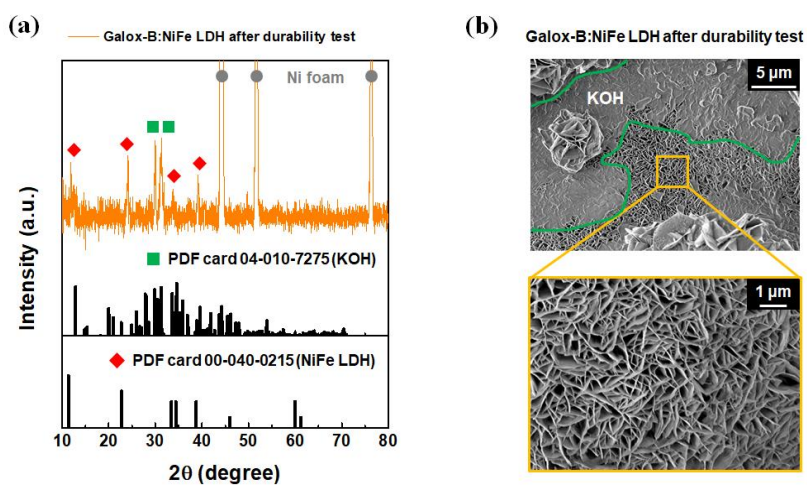


Figure 5.15 Structural and morphological characterization of galox-B:NiFe LDH electrode after OER durability test. (a) XRD analysis of galox-B:NiFe LDH after 100 hours durability test. (b) FE-SEM image of low magnification (top) and high magnification (bottom) of the galox-B:NiFe LDH electrode.

5.3. Summary

In summary, the boron doped nickel iron layered double hydroxide with electrochemical oxidation was fabricated by predictive synthesis based on thermodynamic database and kinetics considerations, such as Pourbaix diagram and current density conditions. The hierarchical structure that consists of boron doped NiFe LDH, and increased ratio of oxyhydroxide on surface of boron doped NiFe LDH through electrochemical oxidation is developed to the OER electrocatalysts for water splitting. Therefore, the electrocatalyst of designed structure achieved an overpotential of 229 mV at 10 mA cm⁻², which confirmed that it was approximately 140 mV lower than Ir under the same conditions.

The boron doping in NiFe LDH is essential for facile charge transfer of efficient oxygen evolution electrocatalysts. The change in intrinsic conductivity due to boron doping and the change in charge transfer due to this conductivity change were confirmed through electrochemical characterization.

The galvanostatic oxidation for activation is essential for improved active sites of oxygen evolution electrocatalysts. It was confirmed that the OER performance was improved due to the increase in the ratio of oxyhydroxide in LDH and the improved active site induced by Jahn-Teller distorted Ni (III) due to NiB_i formation in anodic condition.

While presenting a relatively simple and low temperature boron doping method, it suggested the possibility of mass production of LDH based on enhanced OER performance.

CHAPTER 6

Design and Fabrication of Porous CoS₂ electrocatalysts

(*This chapter self-cites reference [7])

6.1. Introduction

Recently, demand for hydrogen energy, which is eco-friendly and clean energy source, is rapidly increasing, due to depletion of fossil fuels. In particular, hydrogen production through electrochemical water splitting, which is called green hydrogen, is one of the promising solutions to solve this problem. The OER is one of the two electrodes that make up electrochemical water splitting [24, 25]. However, the OER has some issues mentioned in the previous chapter [7, 9]. Solving these issues could increase the overall efficiency of water splitting [7, 17].

The objective of Chapter 6 of this thesis is to enhance the oxygen evolution electrocatalytic performance through phase control and highly porous structure of electrocatalysts. For investigation of gaseous sulfurization and nanopore embedded structure of electrocatalysts, a variety of characterization were performed. In this study, structural design of electrocatalysts is conducted for high exposure of active sites.

6.2. Fabrication of MOF-driven CoS₂ nanoparticles

To perform the HER, OER for effective electrochemical water splitting, structural design of the electrocatalysts and controlling its phase and porosity is essential. Thus, in this section, the process of nanopore embedded electrocatalysts for effective OER catalyst synthesis and process for controlling phase of electrocatalyst are discussed.

In order to apply the mass production of hydrogen, several problems must be solved. First, except for the noble metal electrocatalysts such as Pt in HER, Ir and Ru based materials in OER, the overpotential associated with catalytic activity is very large. Second, while a water electrolysis cell consists of an anode and a cathode in one cell, both electrodes are not balanced. In other words, while HER at cathode is relatively facile and fast, OER at anode is comparatively complex, as described above chapter [7, 9]. Third, although bifunctional electrocatalysts for overall water splitting are in great demand due to simplicity and cost effectiveness, performance is insufficient [12].

6.2.1. Thermodynamic calculation

In order to be applied to mass production, the manufacturing method of the electrocatalysts material should be simple. As the composition of material increases, the synthesis method of electrocatalysts becomes inevitably complicated. For large scale application high efficiency electrocatalysts, the methodology should be simple, and the essential factors such as high activity, high conductivity, and large surface area must be satisfied.

Since metal-organic frameworks (MOFs) are generally known as a porous structure, it or its derived structure can expose many active sites due to large specific surface area

[1, 148]. In particular, Prussian blue analogues (PBAs), category of the MOFs, have a large lattice parameter, about 10 Å, which is advantageous for facile diffusion and high exposure of active site [149]. Additionally, in simple transition metal compounds, the cobalt disulfide (CoS₂), one of the pyrite-type, has high conductivity in transition metal sulfides [3, 150, 151]. Also, it has been reported to exhibit high activity as a OER, HER, or overall water splitting electrocatalysts [3, 48, 72, 152]. Therefore, it is important to synthesize mono-phase CoS₂. However, since cobalt sulfide has various phases such as CoS, Co₉S₈, Co₃S₄, and CoS₂, precise phase control is required. Additionally, since water splitting involves hydrogen and oxygen gas evolution reactions, porosity in the electrocatalysts is very important for improving their performance by facilitating gas emission and exposing active sites. Thus, to further increase the catalytic activity of CoS₂, it is necessary to synthesize porous CoS₂ with nanometer scale pores.

Here, we fabricated highly porous mono-phase CoS₂ as bifunctional water splitting electrocatalysts. Cobalt-based MOFs, namely a cobalt Prussian blue analogue (Co-PBAs, Co₃[Co(CN)₆]₂), were used as a starting material. The Co-PBA was then sulfurized in thermodynamically controlled conditions to remove the organic linker in the Co-PBAs, resulting in pure and mono-phase CoS₂. The synthetic process was predicted based on thermodynamics because cobalt sulfide has been reported in various phase [153], where the phase depends on the S/Co ratio, such as CoS [154], Co₉S₈ [155], and CoS₂ [51, 67]. Thermodynamic calculations control the sulfur vapor pressure depending on the amount of cobalt-based starting materials before sulfurization.

For thermodynamically controlled sulfurization of Co-PBAs, components of the material and process parameters should be determined before the experiment. As a cobalt based starting materials, a Co-PBA was selected, and sulfur powder was used as a sulfur source. To control the sulfur vapor pressure for phase control of cobalt sulfide,

a closed system was used, which was in a fully vaporized state for the thermodynamic calculations about loaded solid sulfur source. To prevent the formation of cobalt oxide, the inside of the closed system was maintained at 0.1 Torr by rotary pump to control oxygen.

As shown in Figure 6.1, the thermodynamic predictive conditions were indicated. The thermodynamic database for thermodynamics calculation is based on the FactsageTM, a thermochemical calculation program. In Figure 6.1(a), the Co-S-O ternary phase diagram at 500 °C, which is higher than the boiling point of sulfur (445 °C), was used to find the mole fraction of cobalt and oxygen for the sulfurization of the Co-PBAs, and the determined value was set as the sulfur amount. Since C and N in Co-PBAs are vaporized to CN at 500 °C, the ternary phase diagram consists of Co-S-O components (Figure 6.1(c)). As the amount of sulfur component is increased, a cobalt sulfide phase with an increased S/Co ratio is synthesized, such as Co, Co₉S₈, CoS₂. To set the exact sulfur amount, the ratio of each element, including Co and O, was calculated. The moles of Co and O were fixed to the certain amount of Co-PBAs in 0.1 Torr in a closed system, illustrated as the dotted line in the phase diagram. Then, the amount of sulfur was the only parameter. Three experimental conditions for sulfur content were selected: 0, 0.1, and 0.5 weight ratios of sulfur/Co-PBAs, as marked in ternary phase diagram as a circle, triangle, and star, respectively. In this thermodynamic calculation, the weight of Co-PBAs was fixed at 30 mg, and the weight of sulfur according to the ratio of S/Co-PBAs was 0, 3, and 15 mg, respectively. The amount of reaction products at 500 °C according to the sulfur loading was calculated and is illustrated on the Figure 6.1(b). As the sulfur content increased in the Figure 6.1(b), Co₉S₈ was produced at first, and then the amount of CoS₂ increased. For a sulfur content with a ratio of more than 0.5, which is 15 mg in this calculated system, a mono-phase CoS₂ can be obtained. However, when the sulfur

exceeded 0.9, which is 27 mg in this system, the liquid sulfur phase remained.

As shown in Figure 6.1(c), it can be seen that as reacting with sulfur, the chemical composition constituting the organic linker of Co-PBA is vaporized into the gas phase. Therefore, the position of the chemical composition forms nanopore due to their vaporization.

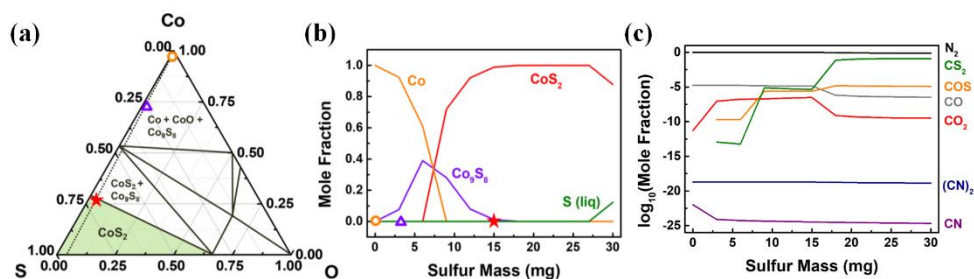


Figure 6.1 Thermodynamics calculations in certain condition. (a) Ternary phase diagram at 500 °C for predicting the required composition to form the target phase. (b) The expected products depending on the amount of sulfur through thermodynamic calculated condition. (c) Sulfurization of Co-PBA related gaseous decomposition products at 500 °C. Other products were completely vaporized except for the cobalt sulfide.

6.2.2. Design of the sulfurization

For thermodynamically controlled sulfurization of Co-PBAs, components of the material and process parameters should be determined before the sulfurization. The synthesis of MOF-driven CoS₂ is schematically shown in Figure 6.2. As a cobalt precursor, a Co-PBA was selected, and sulfur powder was used as a sulfur source. A closed system, comprising a sealed glass ampoule (Figure 6.3), was used to ensure the loaded solid sulfur source was in a fully vaporized state for the thermodynamic conditions. The sulfur and Co-PBA were inserted into the glass ampoule, and the ampoule was fused to create a seal while the pressure inside was maintained at 0.1 Torr. As described in the previous section, it was maintained at 0.1 Torr to suppress the formation of cobalt oxide. Next, to fabricate the cobalt sulfide through gas-solid reaction between sulfur gas and Co-PBA, the reaction temperature was 500 °C, which is higher than the boiling point of sulfur (445 °C). The sulfur inside was completely vaporized, and a reaction between the solid Co-PBA and gaseous sulfur took place. Accordingly, sulfurization was performed at 500 °C for 2 hours to control S/Co according to the amount of sulfur to synthesize cobalt sulfide corresponding to each condition. Considering Co-S-O in the ternary phase diagram of the thermodynamic calculation of previous section, O was maintained at 0.1 Torr and Co-PBAs was set to 30 mg. Accordingly, the weight ratio of S/Co-PBA was set to 0, 0.1, and 0.5, and the weight of sulfur was set to 0, 3, and 15 mg, respectively, which loaded into the ampoule.

Characterization of the synthesized MOF-driven cobalt sulfide will be discussed in the next section.

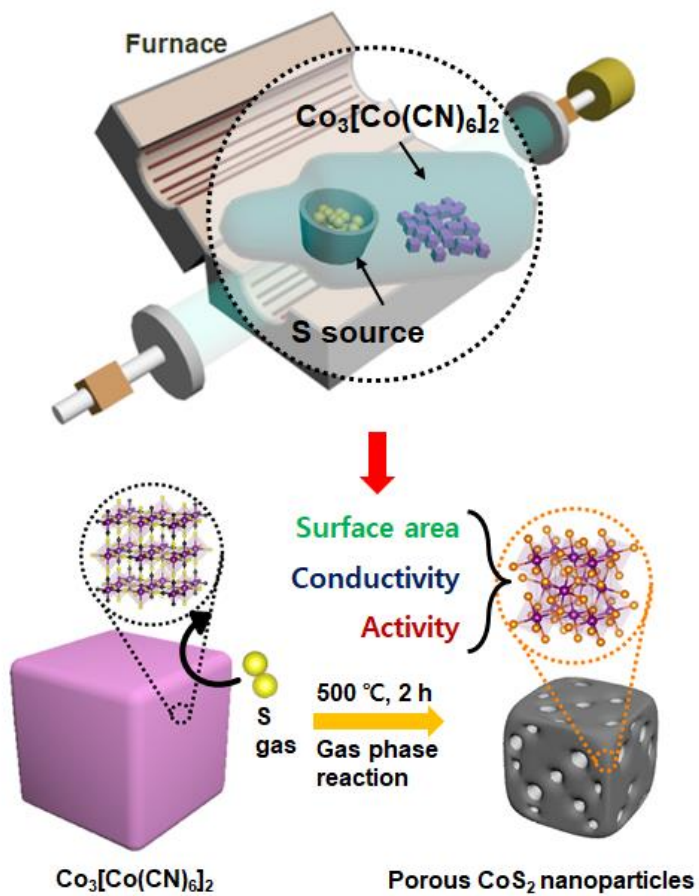


Figure 6.2 Schematic diagram of the fabrication of MOF-driven porous CoS_2 .



Figure 6.3 Image of sealed glass ampoule. Co-PBA and sulfur powder were inserted. The pressure of ampoule was maintained 0.1 Torr.

6.3. Characterization of MOF-driven CoS₂ nanoparticles

Before sulfurization, the morphology of the synthesized Co-PBAs was confirmed through field-emission scanning electron microscopy (FE-SEM) and transmission electron microscopy (TEM) images, as shown in Figure 6.4. The Co-PBAs were fabricated through simple precipitation method. It was confirmed that most of the synthesized nanoparticles remain in angular shape from Co-PBAs in TEM images. This angular shape was typically confirmed in PBAs, which size distribution is usually from tens of nanometers to micrometers scale. The reason for the uniform and angular shape are as follows. In synthesis of PBAs step, sodium citrate is involved in uniformity of PBAs particle size. Citrate in the solution suppressed nucleation of PBAs, and when citrate exceeded further added, second nucleation is avoided [156]. In the mixed solution of cobalt acetate ($\text{Co}(\text{CH}_3\text{COO})_2 \cdot 4\text{H}_2\text{O}$) and sodium citrate ($\text{Na}_3\text{C}_6\text{H}_5\text{O}_7 \cdot 2\text{H}_2\text{O}$), Co^{2+} ion was surrounded by citrate, and reducing the free Co^{2+} ions. Additionally, the XRD pattern of Co-PBA was agreement with the reference PDF card (04-012-6179) which is Prussian blue analogues in Figure 6.5.

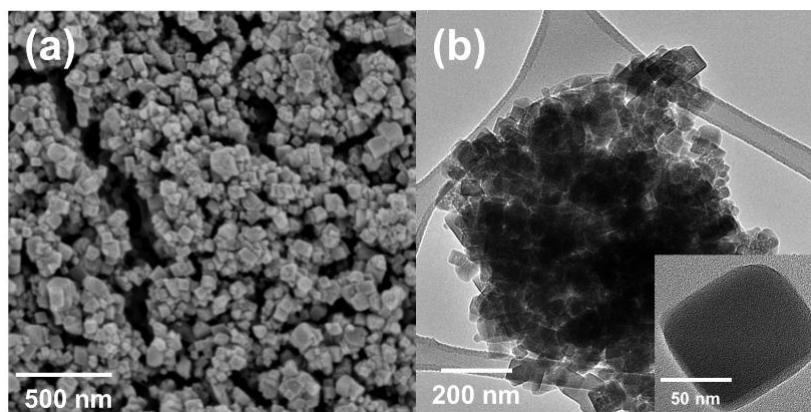


Figure 6.4 Characterization of Co-PBA nanoparticles. (a) FE-SEM and (b) TEM images after synthesis of Co-based MOF using simple precipitation method.

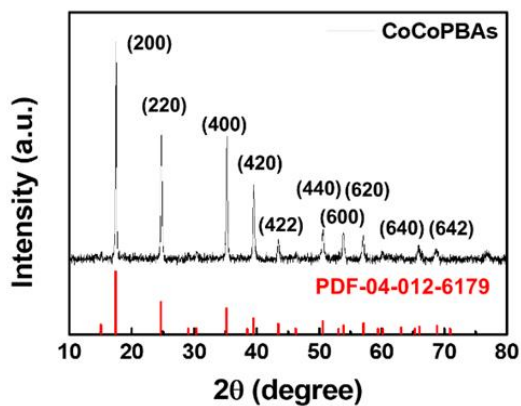


Figure 6.5 Characterization of Co-PBA nanoparticles. XRD analysis for verification of Co-PBA.

Figure 6.6 shows the phase analysis of annealed Co-PBAs after the different sulfur loading mass conditions. Each condition corresponds to the circle, triangle, and star indicated in the phase diagram in the previous section. XRD was conducted for phase analysis after each thermodynamically controlled condition was held for 2 hours. When a 15 mg (0.5 ratio of S/Co-PBA) of sulfur was loaded with mono-phase CoS₂, the target phase was synthesized, while a 0 mg (0 ratio of S/Co-PBA) of sulfur synthesized the Co single phase and a 3 mg (0.1 ratio of S/Co-PBA) of sulfur synthesized the Co₉S₈ phase. As a result of the XRD analysis, it was determined that annealing Co-PBAs without sulfur corresponds to the Co reference PDF card (00-015-0806) in Figure 6.6(a), and sulfurization of the Co-PBAs in the condition represented by a triangle corresponds to the Co₉S₈ reference PDF card (04-004-4525) in Figure 6.6(b). The XRD analysis in Figure 6.6(c) clarified that CoS₂ is mono-phase. In addition, to compare the activity of sulfide and oxide, Co-PBA and air were thermally treated under the same temperature conditions to synthesize Co₃O₄. As shown in Figure 6.7, it was confirmed that Co₃O₄ was synthesized through Co-PBA. Therefore, it can be seen that it is not limited to cobalt sulfide and is a platform capable of synthesizing various porous transition metal compounds according to reactants, such as oxygen, sulfur, phosphorus.

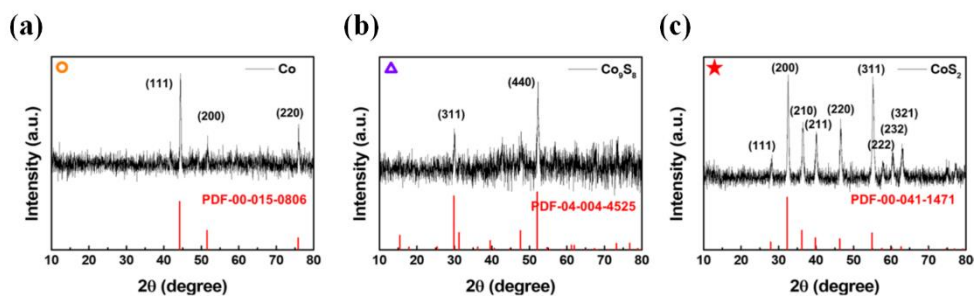


Figure 6.6 Structural characterization for phase analysis of sulfurized Co-PBAs. (a) Annealing for only Co-PBAs, (b) sulfurization of Co-PBAs with 3 mg sulfur, and (c) sulfurization of Co-PBAs with 15 mg sulfur.

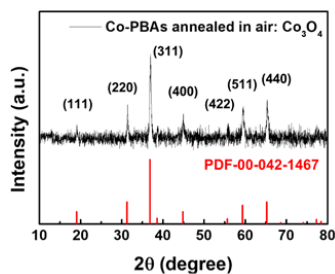


Figure 6.7 XRD analysis of annealed Co-PBAs in 500 °C, air.

Chapter 6: Design and Fabrication of Porous CoS₂ electrocatalysts

To further verify the quantitative analysis of MOF-driven cobalt compound, such as Co, Co₉S₈, and CoS₂, compared with S/Co ratio was investigated through inductively coupled plasma-atomic emission spectroscopy (ICP-AES).

As shown in Table 6.1, cobalt and sulfur ratio through ICP-AES of MOF-driven Co, MOF-driven Co₉S₈, and MOF-driven CoS₂ were indicated. The source of ICP-AES (OPTIMA 8300, Perkin-Elmer, USA) was Ar plasma 6000 K. The spectral range was 167 ~ 782 nm.

Table 6.1 ICP-AES analysis for verification of chemical composition of MOF-driven cobalt compound.

Sample	Co (ppm)	S (ppm)	Co : S ratio
MOF-driven Co	6.7 x 10 ⁵	0	1 : 0
MOF-driven Co ₉ S ₈	5.8 x 10 ⁵	1.9 x 10 ⁵	1 : 0.6
MOF-driven CoS ₂	3.6 x 10 ⁵	3.9 x 10 ⁵	1 : 2

The ratio of Co and CoS₂ corresponds to the ICP-AES result, while the ratio of Co₉S₈ differs slightly. As shown in Figure 6.1(c), part of the loaded sulfur is used to decompose the organic linker of MOF. In particular, compared to CoS₂ (S/Co-PBAs weight ratio: 0.5), a small amount of sulfur is loaded for the fabrication of Co₉S₈ (S/Co-PBAs: 0.1). In Co₉S₈ case, it means that a relatively large ratio of sulfur in total reactant is used for decomposition. For this reason, in Co₉S₈ case, sulfur ratio could be detected relatively low. However, we confirmed that phase of 0.1 ratio of Co/PBAs corresponds with Co₉S₈

through XRD in Figure 6.6(b).

The Figure 6.8-6.10 show the results of microstructural analyses to characterize MOF-driven cobalt sulfide nanoparticles. First, microstructural characterization of MOF-driven Co, Co₉S₈ (0, 0.1 ratio of sulfur/Co-PBA), and commercial CoS₂ were displayed in Figure 6.8. The FE-SEM (Figure 6.8(a-c)) and TEM (Figure 6.8(d-f)) were shown. Furthermore, the FE-SEM (Figure 6.9(a)) and TEM (Figure 6.10) images after sulfurization show that the MOF-driven porous CoS₂ had uniform particle sizes of approximately 25 nm. It is confirmed that the higher S/Co ratio, the smaller the particle size. As can be seen from Figure 6.1(c) of the thermodynamic consideration section, the gas product generated increases as the reaction amount of sulfur increases.

The scanning TEM (STEM) results of MOF-driven CoS₂ are shown in Figure 6.9(b). From the STEM, and EDS mapping images, it can be seen that Co and S constituting MOF-driven CoS₂ are distributed as overall nanoparticles. The corresponding EDS mapping image (Figure 6.9(b)) was shown that the Co (red) and S (green) of MOF-driven CoS₂ were uniformly distributed.

In Figure 6.10(a), there are bright parts in the TEM image that are highlighted with dotted yellow circles [157-160]. As shown in the TEM image, the size of the bright area was approximately 3 to 4 nm, which is shown as nanopore embedded in MOF-driven CoS₂. Through high-resolution TEM (HR-TEM), as shown in Figure 6.10(b), it was confirmed that the MOF-driven CoS₂ had uniform crystallinity for each nanoparticle with a d-spacing of 0.28 nm, which corresponds to the (002) planes. In the inset of Figure 6.10(b), the fast Fourier Transform (FFT) pattern was obtained.

Furthermore, the electron energy loss spectroscopy (EELS) was conducted depending to different sulfurization conditions, such as 0, 0.1, and 0.5 weight ratio of S/Co-PBAs (Figure 6.11). Verification of charge distribution of MOF-driven cobalt compounds was

verified through EELS results. As shown in Figure 6.11, the shift of energy of the Co L₂₃ edge was confirmed according to different sulfurization conditions. The chemical shift of Co L₂₃ edge to higher energy was observed depending on higher S/Co ratio of cobalt sulfide [52].

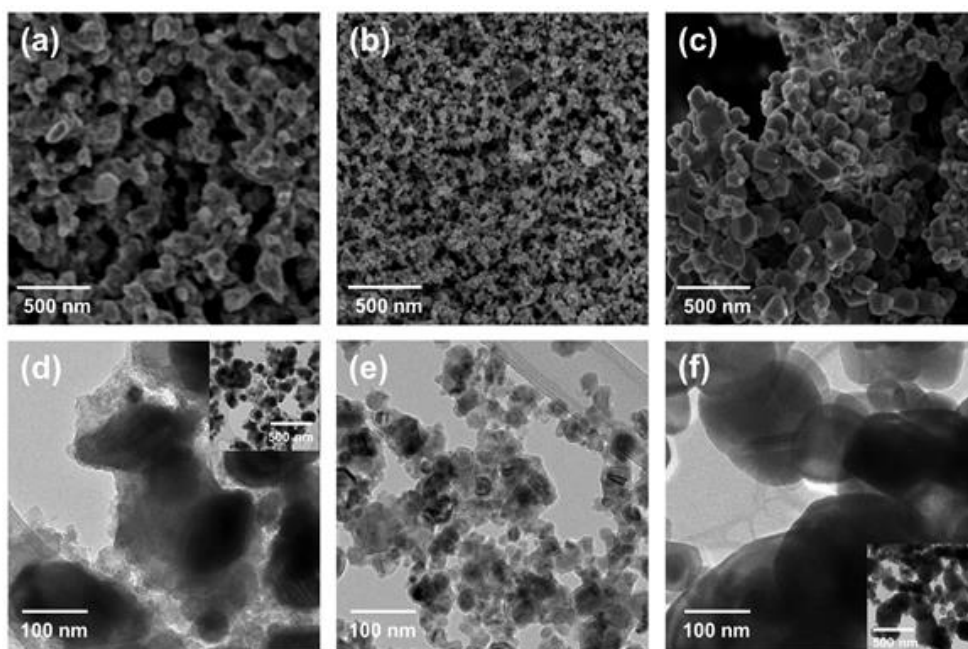


Figure 6.8 Microstructural characterizations, including SEM and TEM, of sulfurized Co-PBAs (MOF-driven Co, Co₉S₈) and commercial CoS₂. (a-c) FE-SEM images and (d-f) TEM images of each cobalt compound, (a), (d) MOF-driven Co, (b), (e) MOF-driven Co₉S₈, and (c), (f) commercial CoS₂.

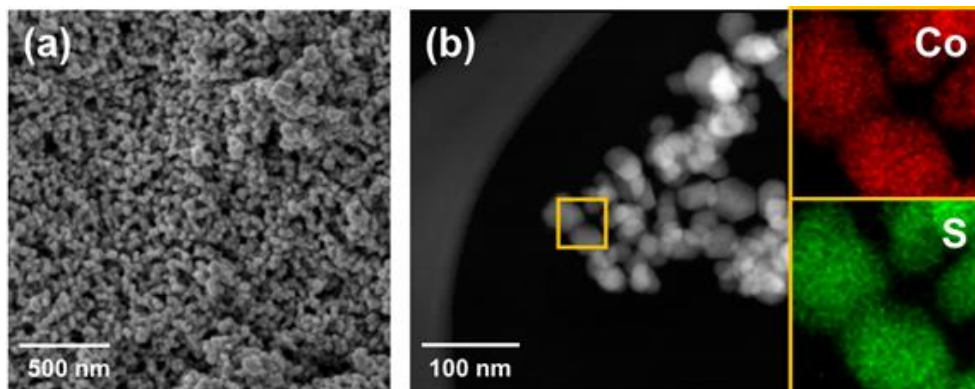


Figure 6.9 Microstructural characterizations, including SEM and STEM, of MOF-driven CoS₂. (a) FE-SEM image. (b) STEM image and EDS elemental mapping images (Co: red, S: green in inset).

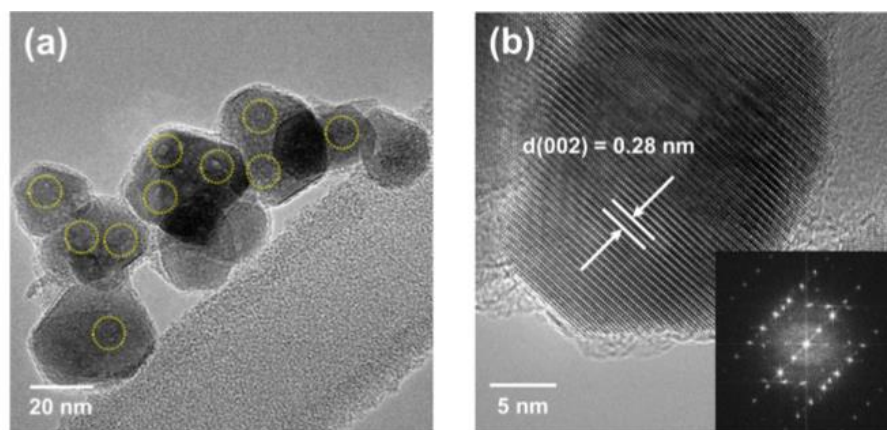


Figure 6.10 Microstructural characterization of MOF-driven CoS₂ nanoparticles. (a) TEM image and (b) HR-TEM image and FFT analysis (inset).

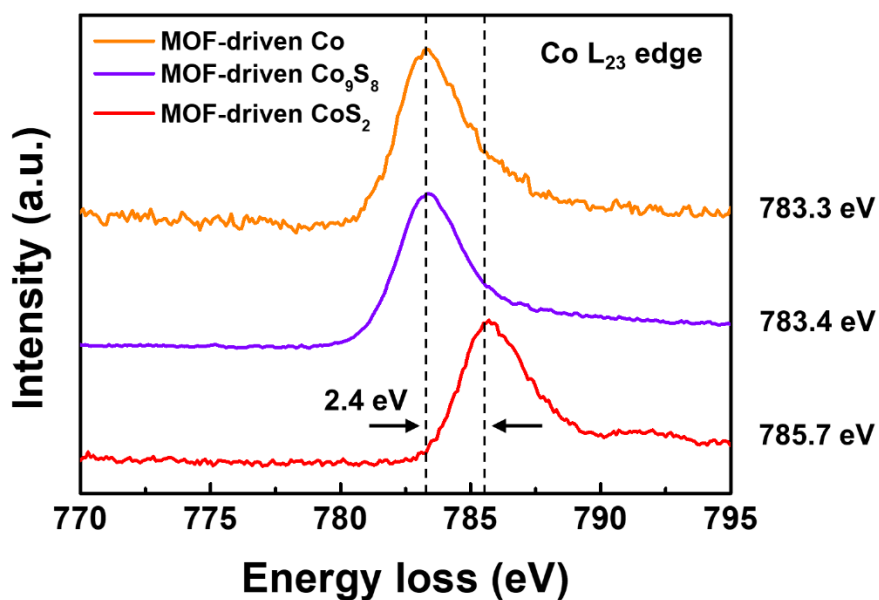


Figure 6.11 The electron energy loss spectroscopy (EELS) spectrum analysis of Co L₂₃ edge for verification of sulfurization from MOF-driven Co, Co₉S₈, and CoS₂ (S/Co-PBAs weight ratio: 0, 0.1, and 0.5).

The X-ray photoelectron spectroscopy (XPS) was performed to investigate the chemical and electronic states of MOF-driven CoS₂ as shown in Figure 6.12. The broad scan, total range scan, in Figure 6.12(a) showed peaks at binding energy of approximately 163, 286, 400, 530, and 780 eV, which were indexed to S 2p, C 1s, N 1s, O 1s, and Co 2p, respectively. In Figure 6.12(b), O 1s for XPS of MOF-driven CoS₂ showed almost negligible peak intensity due to successful fabrication of mono-phase porous CoS₂. In Figure 6.12(c), the Co 2p for XPS of MOF-driven CoS₂ consists of peaks at 794 and 779 eV, which are agreement with Co 2p_{1/2} and Co 2p_{3/2}, respectively. Each peak can split into three sub-peaks, which are located at 796.7, 795.1 and 793.7 eV for the Co 2p_{1/2} peak and 781, 779.7 and 778.5 eV for the Co2p_{3/2} result. As indicated in Figure 6.12(c), the sub-peaks are known as satellites corresponding to Co²⁺ and Co³⁺ [12, 16, 50, 73, 161, 162]. The S 2p spectrum shown in Figure 6.12(d) can typically be split two sub-parts with peaks at 168 and 163 eV. The 163 eV peak generally indicated the ‘-1’ valence state of sulfur, with sub-peaks indexed as 2p_{1/2} (163.6 eV) and 2p_{3/2} (162.5 eV). The peak at 168 eV is typically indexed as a sulfur oxide [72, 152]. In this results, the sulfur oxide peak has a negligibly low intensity compared with other previous reports that describe CoS₂ through hydrothermally sulfurized synthesis. The results of the physical and chemical property analysis through XRD, HR-TEM, and XPS show that the synthesized MOF-driven porous CoS₂ had high purity.

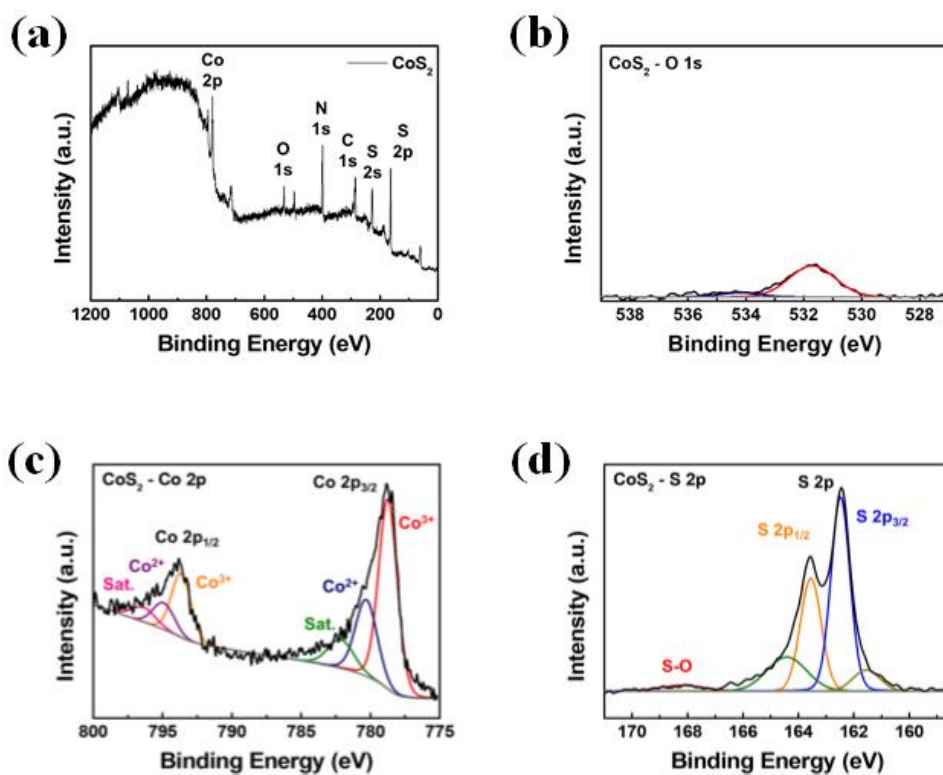


Figure 6.12 Chemical characterization of MOF-driven CoS_2 nanoparticles. (a) The broad scan of MOF-driven CoS_2 nanoparticles. (b) O 1s for XPS. (c) Co 2p spectrum. (d) S 2p spectrum of MOF-driven CoS_2 .

6.4. Summary

The metal-organic framework-driven cobalt sulfides was fabricated through the simple precipitation method, and followed thermodynamically programmed sulfurization process. The metal-organic framework is used as a template to create a porous structure. Then, we controlled the sulfurization condition in closed system of annealing of cobalt based metal-organic framework due to controlling the phase of the cobalt sulfide. In a closed system, only sulfur was used as a parameter, and the phase could be predicted through sulfur vapor pressure control.

Therefore, highly porous structures including nanoscale pores were fabricated. The structural characterization of the synthesized metal-organic framework-driven cobalt disulfide confirmed the uniformity and porous structure compared with commercial cobalt disulfide. Furthermore, according to the amount of sulfur loaded in closed system, it was confirmed that not only cobalt disulfide but also other cobalt sulfide can be synthesized.

CHAPTER 7

Electrochemical Performance of Porous CoS₂ electrocatalysts

(*This chapter self-cites reference [7])

7.1. Introduction

In Chapter 6, we have successfully fabricated metal-organic framework-driven cobalt disulfide, which is expected to be crucial for the enhanced overall water splitting. Additionally, the hierarchical porous structure to adopt metal-organic framework-driven cobalt disulfide to the both electrodes, including cathode and anode, of water splitting, which consists of porous active materials is developed to improve the electrocatalytic HER, OER performance. This is due to an increase in the nanopores through sulfurized cobalt based metal-organic framework and high exposure of active site.

The purpose of this chapter is analyze the effect of nanopores in the electrocatalysts, as well as the effect of controlling the phase of electrocatalysts. In this chapter, *ex-situ* analysis, including electrochemical, physical adsorption analysis to explain this effect, will be discussed.

7.2. Electrochemical performances

The electrochemical performance of the MOF-driven cobalt sulfide OER and HER electrocatalysts was investigated under alkaline electrolyte of 1.0 M KOH. To examine the bifunctional electrocatalytic activity of the MOF-driven porous CoS₂ nanoparticles on the nickel foam electrode, linear sweep voltammetry (LSV) was conducted for the bare nickel foam, IrO₂, Pt electrode, commercial CoS₂, and MOF-driven cobalt compound, such as Co, Co₉S₈, Co₃O₄, and CoS₂. The OER and HER were performed with a conventional three-electrode system in 1.0 M KOH. The polarization curves were conducted in the potential range between 1.2 and 1.7 V (vs. reversible hydrogen electrode (RHE)) for the OER at a scan rate 1.0 mV s⁻¹ and between -0.4 and 0.0 V (vs. RHE) for the HER at a scan rate of 5.0 mV s⁻¹. First, the OER activity of the electrocatalysts was measured as the overpotential at a current density of 10 mA cm⁻², which is typically used as a reference to evaluate electrocatalyst [7, 142] and the Tafel slope. As shown in Figure 7.1, displays the polarization curves of the OER range. In order to confirm the superiority of MOF-driven CoS₂ electrode, it was compared with IrO₂, a noble metal oxide most frequently used as an OER electrocatalyst. The MOF-driven CoS₂ electrocatalyst electrode shows a low overpotential requirement of 298 mV at 10 mA cm⁻², while the others show a higher overpotential. The overpotential of the MOF-driven Co, MOF-driven Co₉S₈, commercial CoS₂, IrO₂, and MOF-driven Co₃O₄ were 411, 362, 379, 374, and 359 mV, respectively. Additionally, the LSVs of Ir foil, Pt electrode, and nickel foam were conducted (Figure 7.3). The activity of MOF-driven Co₃O₄ was investigated for comparison with MOF-driven CoS₂. Co₃O₄ is known as the most efficient OER electrocatalyst among the cobalt oxide phases, but does not reach the efficiency of MOF-driven CoS₂ electrocatalyst. Additionally, the oxidation peak in

the polarization curves was confirmed to be from the Co (III) to Co (IV) transition [90]. The MOF-driven CoS₂ shows a larger oxidation peak in this location than that in previously reported studies. The larger the specific surface area, the greater the intensity of the redox peak. Analysis of the specific surface area associated with this will be discussed in the next section.

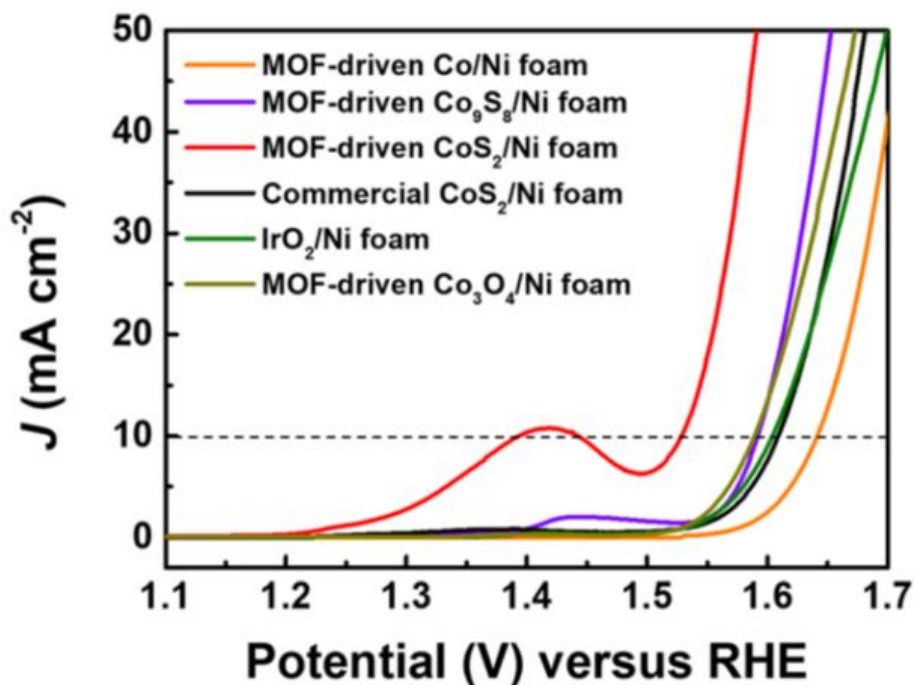


Figure 7.1 Electrochemical characterization of each electrode for water oxidation in 1.0 M KOH. The OER polarization curves through linear sweep voltammetry (LSV) of different electrode with a scan rate 1.0 mV s⁻¹.

Chapter 7: Electrochemical Performance of Porous CoS₂ electrocatalysts

Next, as shown in Figure 7.2, the Tafel plot was displayed for calculation of Tafel slope and to analyze the electrocatalyst reaction kinetics, which was plotted based on the potential against $\log(J)$. The tendency of the Tafel slope and overpotential were similar. The synthesized MOF-driven CoS₂ electrode, which had the lowest overpotential in the polarization curves, showed a low Tafel slope value (94 mV dec⁻¹). In this context, reaction kinetics of the MOF-driven CoS₂ are fastest among the measured electrocatalysts, which may mean high exposure of active site with nanopore embedded structure and phase control through sulfur vapor pressure in closed system.

To verify the stability of the MOF-driven porous CoS₂ nanoparticles, a long-term durability test was performed using the chronoamperometric method (Figure 7.4). At a constant voltage of 1.53 V (vs. RHE, 300 mV), the synthesized MOF-driven CoS₂ electrode delivered a relatively stable current density of 12 mA cm⁻² over 20 hours. As oxygen evolution occurs during the stability test, fluctuations were observed due to gas bubbling.

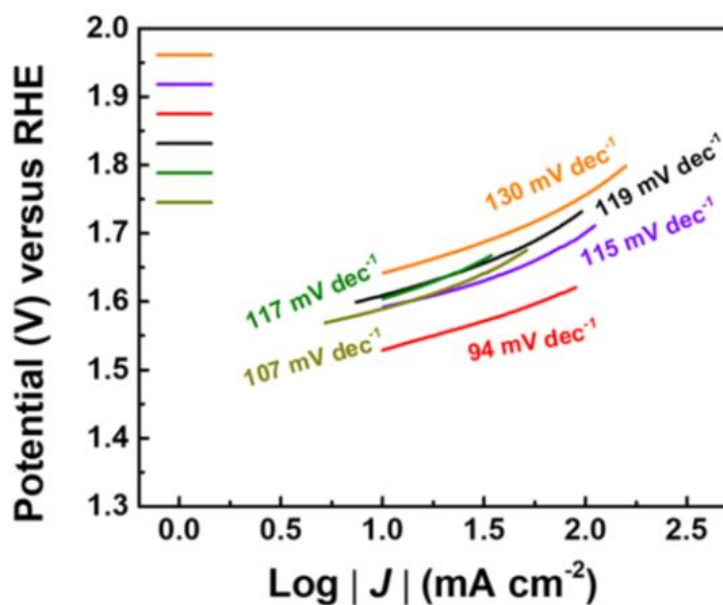


Figure 7.2 Electrochemical characterization of each electrode for water oxidation in 1.0 M KOH. Tafel slopes of polarization curves in OER.

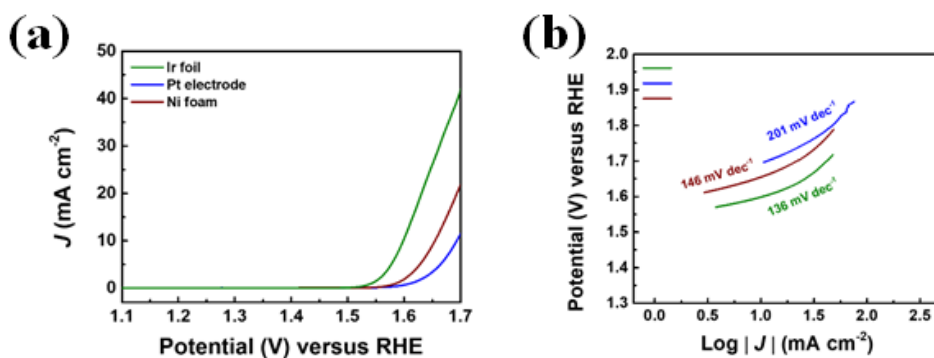


Figure 7.3 Electrochemical characterization of Ir foil, nickel foam, and Pt electrode. (a) OER polarization curves. (b) Tafel slopes of polarization curves in OER.

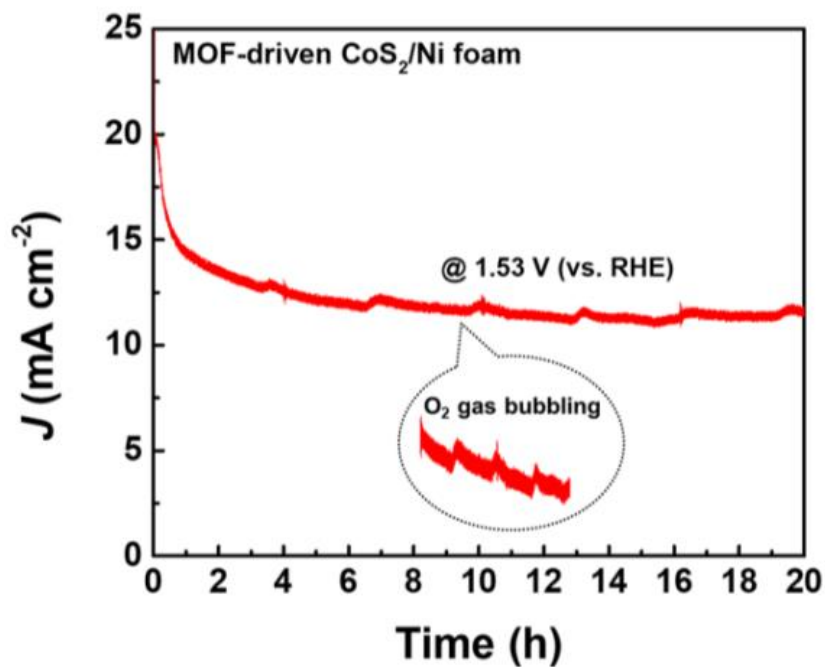


Figure 7.4 Electrochemical characterization of MOF-driven CoS₂ electrode. The stability test through chronoamperometric method of fabricated MOF-driven CoS₂ at constant voltage.

Chapter 7: Electrochemical Performance of Porous CoS₂ electrocatalysts

Next, HER electrocatalytic activity was assessed as the overpotential at a current density of 10 mA cm⁻² and the Tafel slope. As shown in Figure 7.5, displays the polarization curves of the HER range. In order to confirm the superiority of MOF-driven CoS₂ electrode, it was compared commercial CoS₂, which is simple particle without pore. The MOF-driven CoS₂ electrocatalyst electrode shows a low overpotential requirement of -196 mV at 10 mA cm⁻², while the commercial CoS₂ electrocatalysts shows a large overpotential. The overpotential of the MOF-driven Co, MOF-driven Co₉S₈, IrO₂, and Pt electrode were -214, -213, -198, and -67 mV, respectively. Additionally, the LSVs of Ir foil and nickel foam were conducted (Figure 7.7). The synthesized MOF-driven CoS₂ electrode also shows high activity in the HER despite the presence of a strong alkaline electrolyte.

As shown in Figure 7.6, the Tafel slope was calculated based on the HER polarization curves, as in the OER results. Under the overpotential results, Pt and synthesized MOF-driven CoS₂ electrodes exhibited Tafel slopes of 38 and 113 mV dec⁻¹, respectively. Therefore, the synthesized CoS₂ electrode shows the Volmer-Heyrovsky mechanism behavior [104].

To verify the HER stability of the MOF-driven porous CoS₂ nanoparticles, a long-term durability test was performed using the chronoamperometry (Figure 7.8). At a constant voltage of -0.2 V (vs. RHE), the synthesized MOF-driven CoS₂ electrode delivered a relatively stable current density of -11 mA cm⁻² over 20 hours. As hydrogen evolution occurs during the stability test, fluctuations were observed due to gas bubbling.

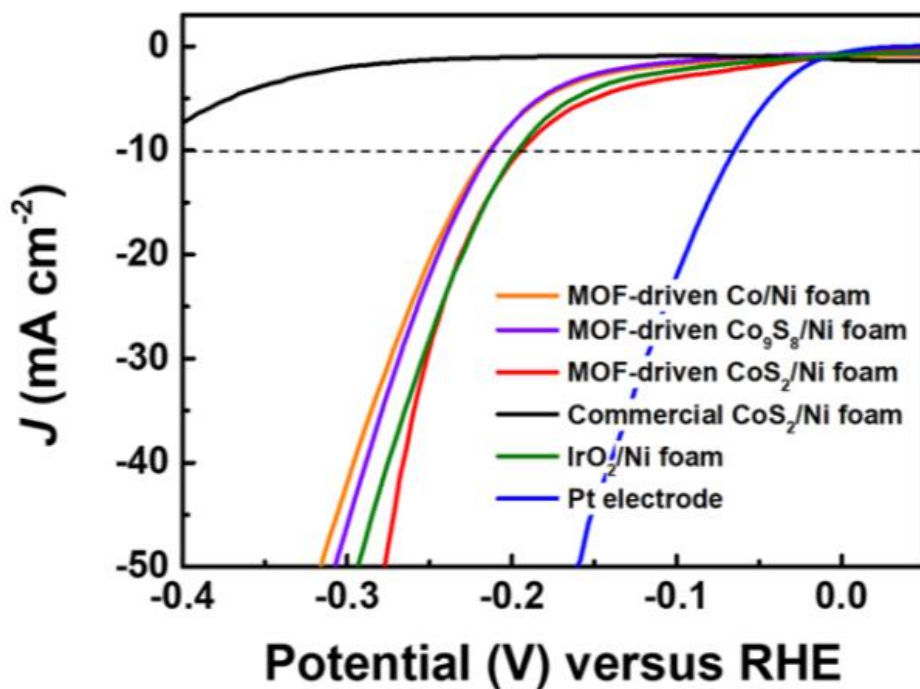


Figure 7.5 Electrochemical characterization of MOF-driven porous CoS₂ nanoparticles in 1.0 M KOH. HER polarization curves of electrode with a scan rate 5 mV s⁻¹.

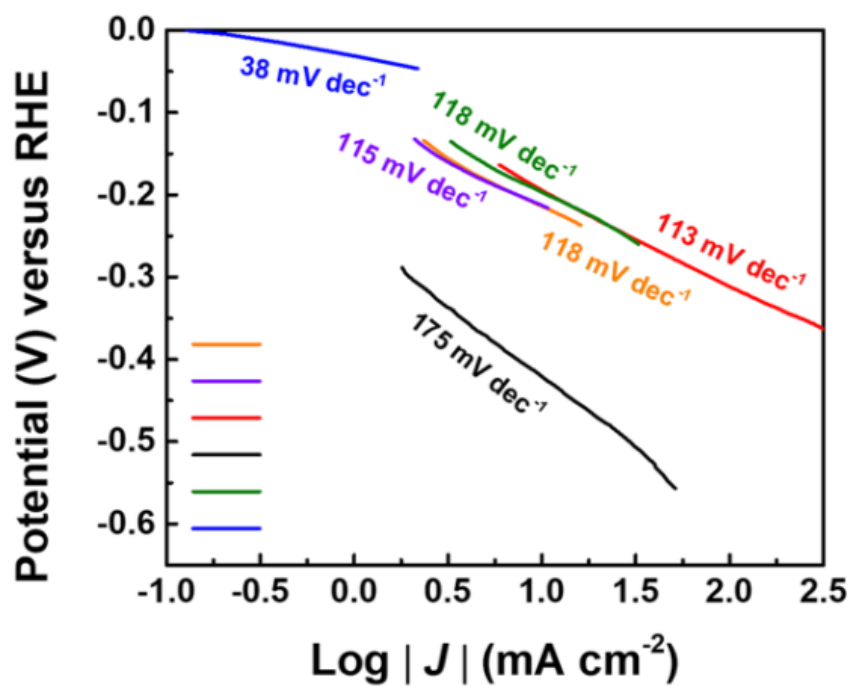


Figure 7.6 Electrochemical characterization of MOF-driven porous CoS₂ nanoparticles in 1.0 M KOH. Tafel slopes of polarization curves in HER.

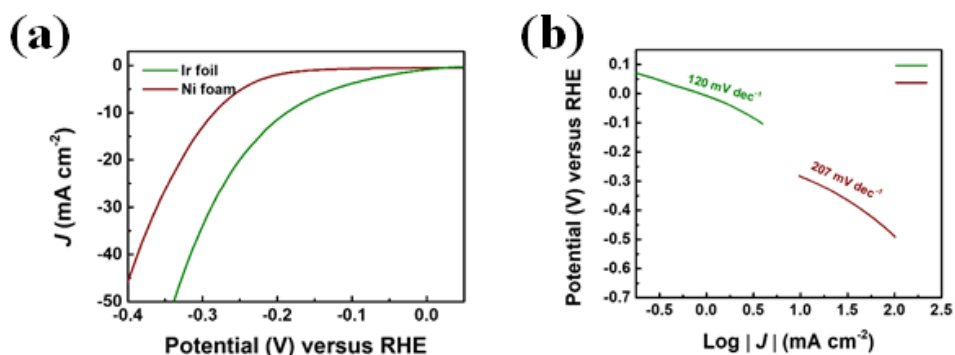


Figure 7.7 Electrochemical characterization of Ir foil and nickel foam. (a) HER polarization curves. (b) Tafel slopes of polarization curves in HER.

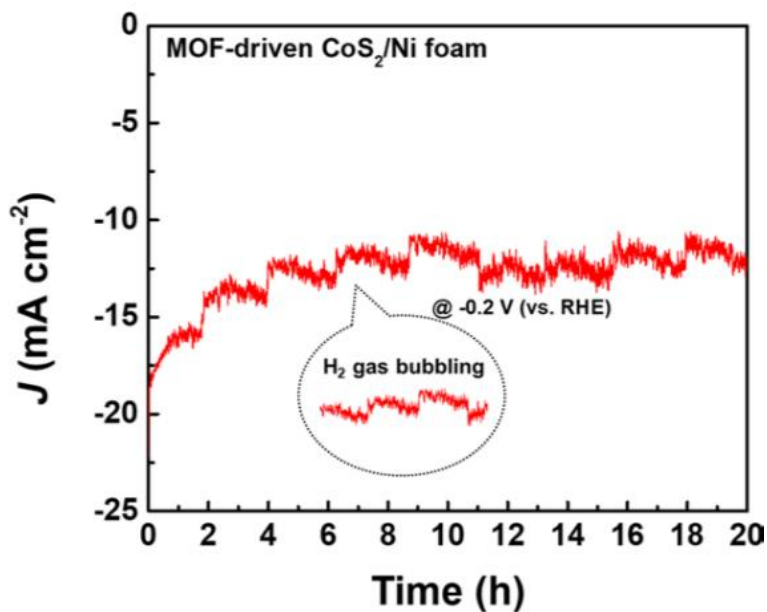


Figure 7.8 Electrochemical characterization of MOF-driven CoS_2 electrode. The stability test through chronoamperometry of fabricated CoS_2 at constant voltage.

Chapter 7: Electrochemical Performance of Porous CoS₂ electrocatalysts

Figure 7.9 shows the performance of bifunctional electrocatalytic activity, which was performed through a full-cell test of electrochemical water splitting for a practical two-electrode system in 1.0 M KOH. Both electrodes, anode for OER and cathode for HER, were assembled from the same electrode material, which was MOF-driven CoS₂ on Ni foam in this work. The potential range was from 0.0 to 2.0 V with a scan 5.0 mV s⁻¹. As shown in Figure 7.9, the assembled full-cell exhibited an overpotential of 1.65 V at 10 mA cm⁻².

As shown in Figure 7.10, the stability test was also conducted for symmetric full-cell. At a constant voltage of 1.7 V, the synthesized MOF-driven CoS₂ electrode delivered a relatively stable current density of 11 mA cm⁻² over 20 hours. As shown above, it was verified with structural characterization, chemical characterization and morphological characterization that the synthesized MOF-driven CoS₂ had a highly porous structure, including nanoscale pores. According to these results, the MOF-driven CoS₂ nanoparticles provided facile diffusion kinetics as well as enough active sites. For this reason, the fabricated MOF-driven CoS₂ electrode had a high OER and HER catalytic activities despite no additional treatment.

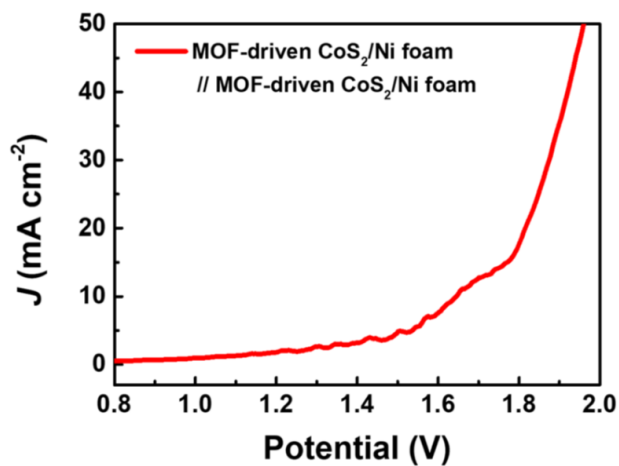


Figure 7.9 Overall water splitting performance of MOF-driven CoS₂ nanoparticles through polarization curve using symmetric full-cell.

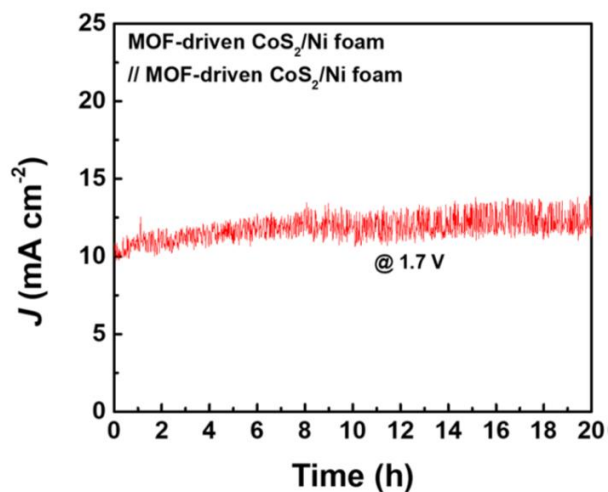


Figure 7.10 Overall water splitting performance of MOF-driven CoS₂ nanoparticles through chronoamperometric durability test of symmetric full-cell.

7.2.1. Effects of nanopores in electrocatalysts

The electrochemical and physical adsorption characterizations were performed to demonstrate the tendency of electrochemical performance identified in the previous section. To further verify the formation of porous structure in the MOF-driven cobalt sulfide, an analysis through Brunauer-Emmett-Teller (BET) was performed through N₂ adsorption/desorption, where BET specific surface area and pore diameter were obtained. In the case of MOF-driven CoS₂, the BET specific surface area in Figure 7.11 was 915.6 m² g⁻¹, compared with 6.1, 46.0, and 60.1 m² g⁻¹ for commercial CoS₂, MOF-driven Co, and Co₉S₈, respectively. Additionally, BET specific surface area of MOF-driven Co₃O₄ in Figure 7.12 was 43.2 m² g⁻¹. This result implies that MOF-driven CoS₂ had 150 times higher porosity than that of commercial CoS₂. Furthermore, the Barrett-Joyner-Halenda (BJH) desorption was measured to quantitatively express the pore diameter shown in Figure 7.13. Two main peaks were observed in the BJH results, and the peaks appeared at approximately 3.5 nm in MOF-driven CoS₂ and at ~ 20 nm, gradually increasing from 6 nm, which includes the surface of nanoparticles because there is no selectivity of pore and surface for the adsorption/desorption of N₂ during BET specific surface area measurements. Additionally, the peak of MOF-driven Co and Co₉S₈ were also detected at approximately 3.5 nm. However, it was relatively low intensity compared with MOF-driven CoS₂. The pore size and distribution could be related sulfur vapor pressure, since as can be seen from Figure 6.1(c) of the thermodynamic consideration section, the gas product generated increases as the reaction amount of sulfur increases. In contrast, the pore size and distribution were not nearly detected in the commercial CoS₂.

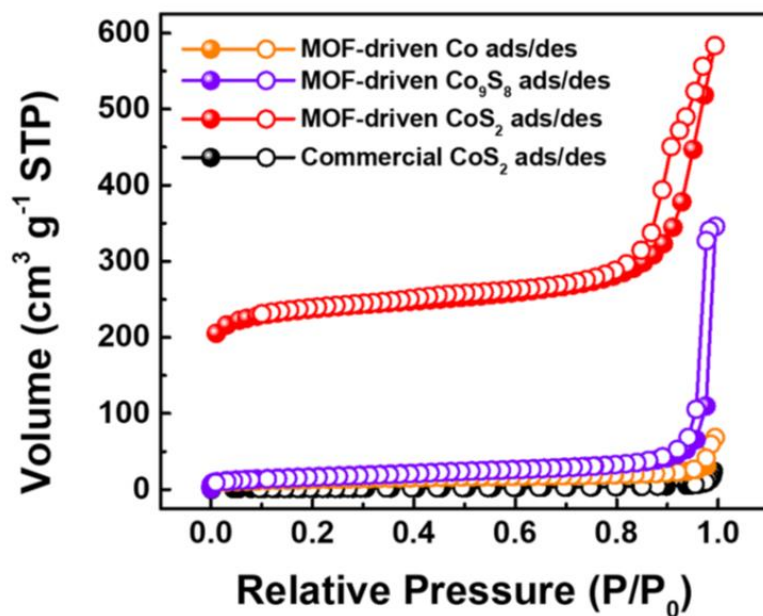


Figure 7.11 Physical adsorption characterization of MOF-driven cobalt compound and commercial CoS₂ electrocatalysts. BET analysis of isothermal plot with N₂ adsorption/desorption.

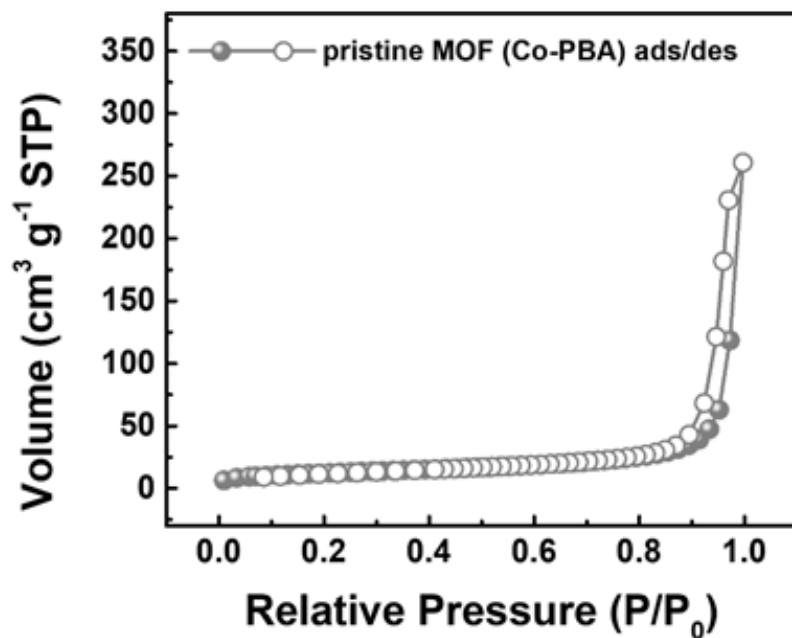


Figure 7.12 Physical adsorption characterization of MOF-driven Co₃O₄ electrocatalysts. BET analysis of isothermal plot with N₂ adsorption/desorption.

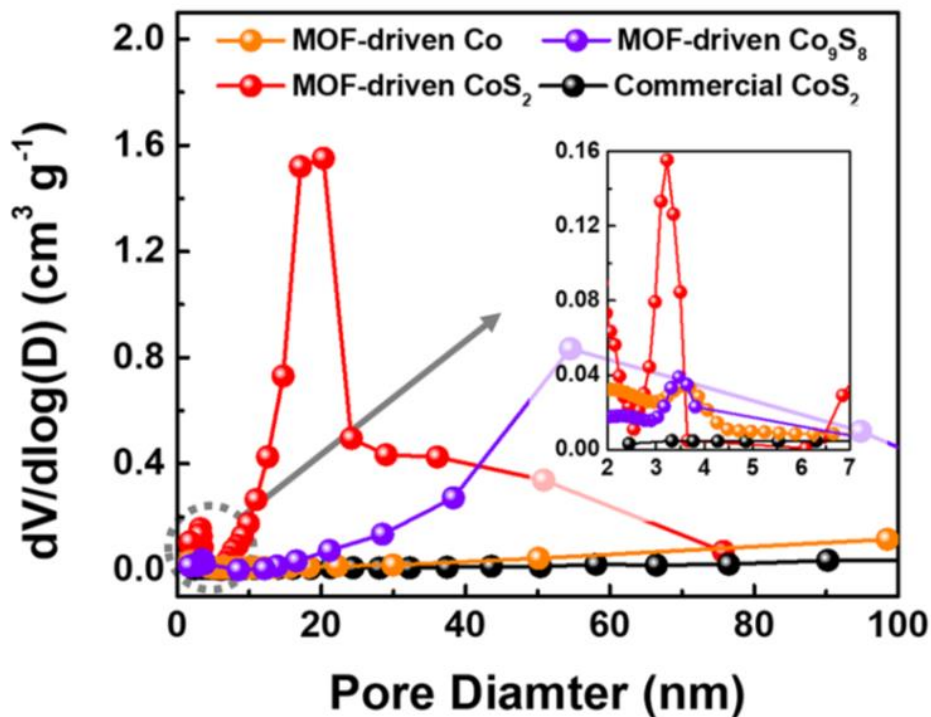


Figure 7.13 Physical adsorption characterization of MOF-driven cobalt compound and commercial CoS₂ electrocatalysts. Pore diameter distribution of MOF-driven Co, Co₉S₈, CoS₂ and commercial CoS₂ (inset: magnification of the small pore diameter area).

The porous structures were also observed in the TEM image in Figure 6.10(a), which confirmed the BET analysis. As shown in the TEM image, the size of the bright area was approximately 3 to 4 nm. Additionally, the results of electrochemical surface area (ECSA) were shown in Figure 7.14 and Table 7.1. The linear slopes of commercial CoS₂ on nickel foam electrode and MOF-driven CoS₂ on nickel foam electrode are 0.7 and 1.5 mF cm⁻², respectively, confirmed that the ECSA difference was about 2.1-fold.

Additionally, the ECSA of MOF-driven Co and Co₉S₈ showed 0.7 and 1.1 mF cm⁻², respectively. The ECSA of each electrode was calculated in Table 7.1.

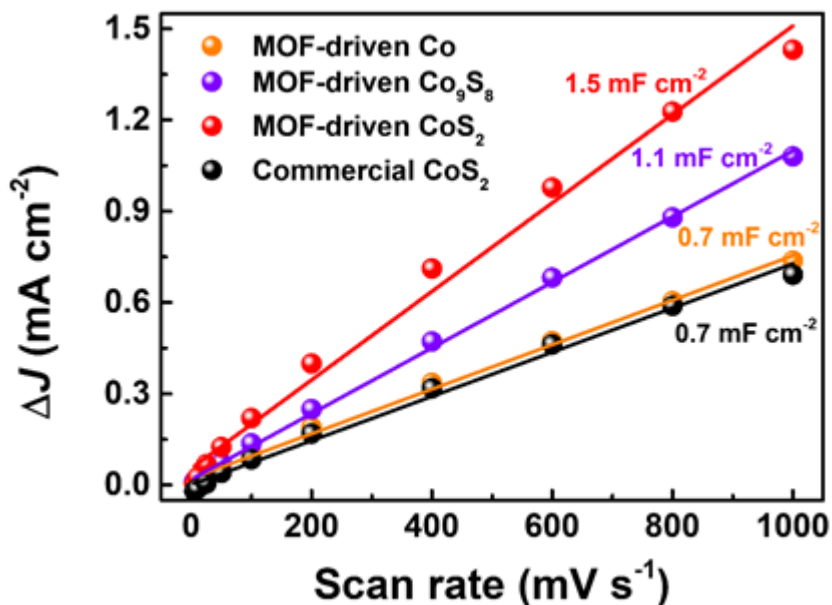


Figure 7.14 ECSA of commercial CoS₂, MOF-driven Co, Co₉S₈, and CoS₂ (S/Co-PBAs weight ratio: 0, 0.1, and 0.5). The linear slope is related to the double layer capacitance.

As described previous Chapter 5, the CV was conducted in the voltage range between 0.18 and 0.28 V (vs. RHE). The linear slope was calculated by plotting ΔJ at 0.23 V (vs. RHE) depending on scan rates. The linear slope is two-fold of the double-layer capacitance (C_{dl}) [7, 114, 146, 147]. ΔJ , C_{dl} , and ECSA can be calculated following eqn (7.1), (7.2), (7.3) [5, 66, 147].

Chapter 7: Electrochemical Performance of Porous CoS₂ electrocatalysts

$$\Delta J = J_a - J_c \quad (7.1)$$

$$C_{dl} = 1/2 \times d(\Delta J)/dV \quad (7.2)$$

$$ECSA = C_{dl} / C_s \quad (7.3)$$

C_s is the capacitance of atomically smooth planar surface in 1.0 M KOH electrolyte ranges between 20 to 60 μF cm⁻². For calculation, C_s was configured at 40 μF cm⁻² [66].

Table 7.1 Calculation of ECSA of commercial CoS₂, MOF-driven Co, Co₉S₈, and CoS₂.

Electrocatalysts	Slope	C _{dl}	ECSA
MOF-driven Co/Ni foam	0.7 mF cm ⁻²	0.35 mF cm ⁻²	8.75 cm ² _{ECSA}
MOF-driven Co ₉ S ₈ /Ni foam	1.1 mF cm ⁻²	0.55 mF cm ⁻²	13.75 cm ² _{ECSA}
MOF-driven CoS ₂ /Ni foam	1.5 mF cm ⁻²	0.75 mF cm ⁻²	18.75 cm ² _{ECSA}
Commercial CoS ₂ /Ni foam	0.7 mF cm ⁻²	0.35 mF cm ⁻²	8.75 cm ² _{ECSA}

7.2.2. Effects of phase control in cobalt sulfide

The impedance measurements were performed to demonstrate the tendency of electrochemical characterization depending on the cobalt sulfide phases identified in the previous section. To further clarify the effect of the porous CoS₂ electrocatalysts for facile charge transfer during reaction steps for water oxidation, an analysis through electrochemical impedance spectroscopy (EIS) was performed in the frequency from 100,000 to 0.01 Hz at constant overpotential of 300 mV. In order to compare the charge transfer in the reaction step for oxygen evolution, EIS was measured while applying 300 mV to create a condition in which sufficient onset of each electrode had progressed. In order to quantitatively compare the charge transfer caused by porous structure due to nanopore embedded structure, the charge transfer resistance (R_{ct}) term of EIS was used.

The resistance term of plotted EIS consist of electrolyte resistance (R_e) and charge transfer resistance (R_{ct}) in Figure 7.15. Since the configuration of the electrochemical cells for measuring each electrode is all the same, the components of the EIS all the same. First, R_e refers to the position of the starting point of the semicircle in the Nyquists plot [143, 144]. The R_e is also a resistance term that occurs in an electrochemical cell, and since the components are all the same, there is no significant difference for each electrode. In the Nyquists plot, the R_{ct} is the value corresponding to the diameter of the semicircle [143, 144]. It can be seen that R_{ct} increases in the order of MOF-driven CoS₂, commercial CoS₂, MOF-driven Co₉S₈, and MOF-driven Co. The R_{ct} of MOF-driven CoS₂ was lower than commercial CoS₂. It can be seen as a decrease in charge transfer resistance of porous CoS₂ by nanopore embedded in electrocatalysts. Also, the R_{ct} of CoS₂ group, including MOF-driven CoS₂ and commercial CoS₂, was the lowest compared to the other cobalt compound, such as MOF-driven Co, and Co₉S₈. Regardless

of porosity of electrocatalyst, it can be seen that CoS₂ is one of the most suitable OER electrocatalysts in terms of charge transfer.

Thus, it can be expressed as shown in inset of Figure 7.15 by representing it through an equivalent circuit according to the Nyquist plot of Figure 7.15.

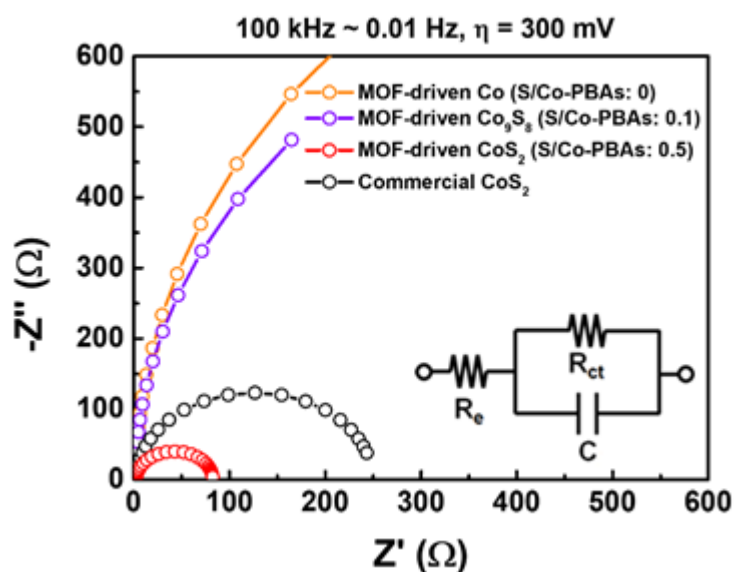


Figure 7.15 Nyquist plots at 300 mV (vs. RHE) for commercial CoS₂, MOF-driven Co, Co₉S₈, and CoS₂ (S/Co-PBAs weight ratio: 0, 0.1, and 0.5) electrodes. Inset is equivalent circuit model.

Chapter 7: Electrochemical Performance of Porous CoS₂ electrocatalysts

In Figure 7.16, to further investigate the change of MOF-driven CoS₂ upon electrochemical characterization, such as OER, HER durability test, morphological, structural and chemical characterization was performed after OER and HER durability test. As shown in Figure 7.16(b) and (f), the MOF-driven CoS₂ nanoparticles well-retained on the nickel foam compared with Figure 7.16(a), although slight change of morphology was shown in FE-SEM images after OER and HER durability test. This slight change phenomenon is inevitable, because oxygen and hydrogen gas were vigorously generated during OER and HER stability test, respectively [16, 163]. Additionally, the XRD pattern of MOF-driven CoS₂ on nickel foam electrode had hardly changed after HER (Figure 7.17). On the other hand, peak of CoOOH was slightly detected in the electrode after OER durability test (Figure 7.17). This detection of CoOOH can also be confirmed in TEM and XPS, and is known as a reaction product generated when the Co based electrocatalyst undergoes the OER [23].

As shown in Figure 7.16(c-e), TEM, including HR-TEM, analysis after OER stability was conducted. The lattice fringes and FFT corresponding to CoS₂ (Figure 7.16(d)) and CoOOH (Figure 7.16(e)) were observed. However, these lattice fringes featured low crystallinity, due to the crystalline to amorphous transition in electrocatalysts of transition metal compound [12]. The EDS mapping after OER durability test of MOF-driven CoS₂ electrode was conducted (Figure 7.18(a)). The signal of sulfur was relatively weak due to formation of surface CoOOH [23], although the cobalt and oxygen of MOF-driven CoS₂ after OER stability test were uniformly distributed. XPS analysis was performed (Figure 7.18(b-d)). The peak of CoOOH in 783 eV was observed in Co 2p spectrum [23, 64]. In S 2p spectrum, only S-O peaks were featured [12, 164]. The intensity of total O 1s after OER stability test was relatively increased

Chapter 7: Electrochemical Performance of Porous CoS₂ electrocatalysts

compared to O 1s before test in Figure 6.12(b). Furthermore, additional peak was also detected at 529.9 eV corresponding to the cobalt oxide [90].

After carrying out the HER stability test, TEM analysis, including HR-TEM, was also performed (Figure 7.16(g), (h)). The lattice fringe of low crystalline CoS₂ was observed as OER part. EDS mapping and XPS analysis after HER stability test were displayed in Figure 7.19. In EDS mapping (Figure 7.19(a)), relatively weak signal of oxygen and sulfur was detected due to formation of transition chalcogenide hydrides during HER [16, 165]. In XPS analysis (Figure 7.19(b-d)), the peak of intensity at 781 eV corresponding to Co 2p_{3/2} was increased, which this phenomenon was also reported in previous work [12].

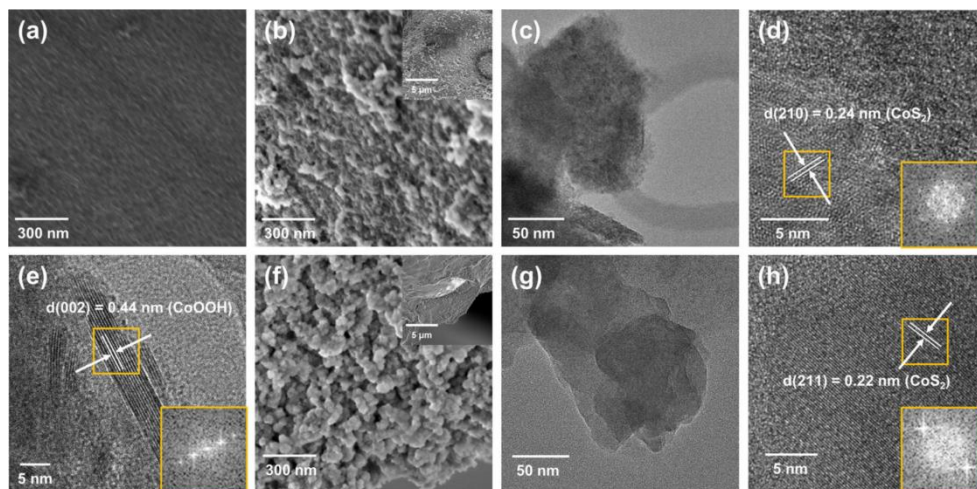


Figure 7.16 Morphological characterization of MOF-driven CoS₂ electrode after stability test. (a) FE-SEM image of the bare nickel foam. (b) FE-SEM (inset: low magnification), (c) TEM, and (d,e) HR-TEM (inset: FFT analysis) image of MOF-driven CoS₂ electrode after OER stability at 1.53 V (vs. RHE). (f) FE-SEM (inset: low magnification), (g) TEM, and (h) HR-TEM (inset: FFT analysis) image of MOF-driven CoS₂ electrode after HER stability at -0.2 V (vs. RHE).

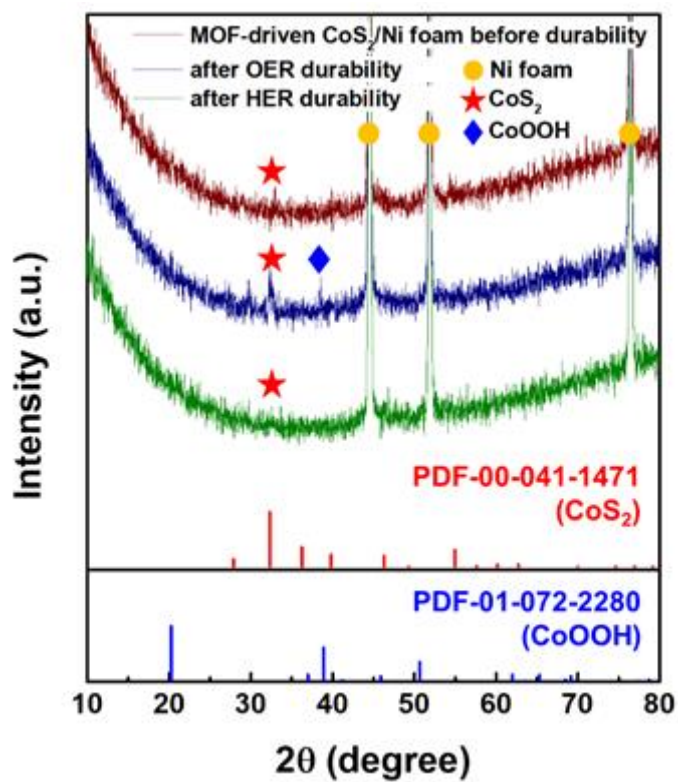


Figure 7.17 XRD analysis for observation of phase change of MOF-driven CoS_2 after 20 hours OER and HER stability test.

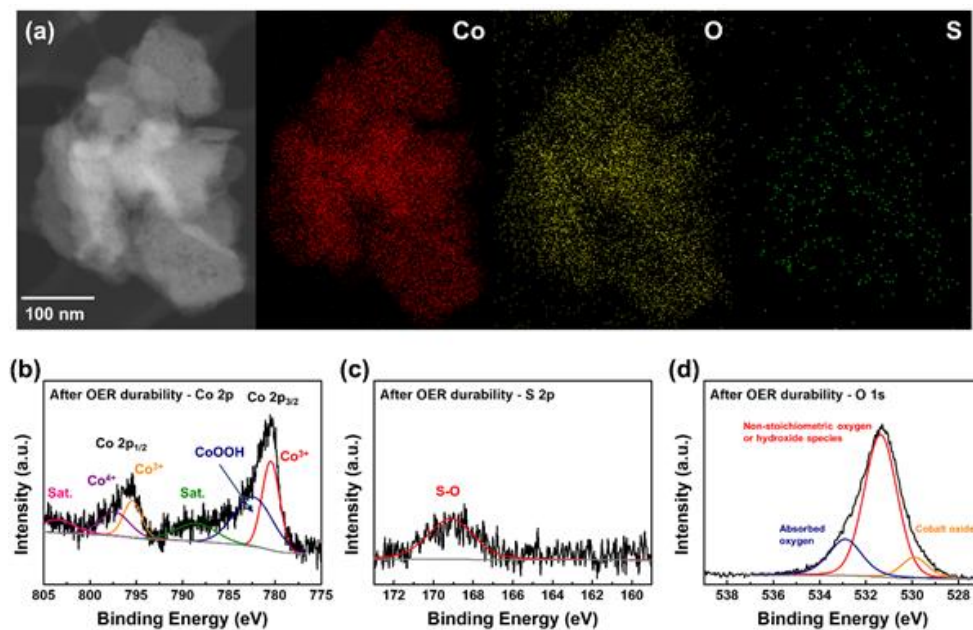


Figure 7.18 Chemical composition and electronic state change of MOF-driven CoS₂ after 20 hours OER stability test at 1.53 V (vs. RHE). (a) STEM image and EDS elemental mapping images in inset (cobalt: red, oxygen: yellow, sulfur: green). XPS analysis of MOF-driven CoS₂ after OER stability test. (b) Cobalt 2p, (c) sulfur 2p, and (d) oxygen 1s spectrum, respectively.

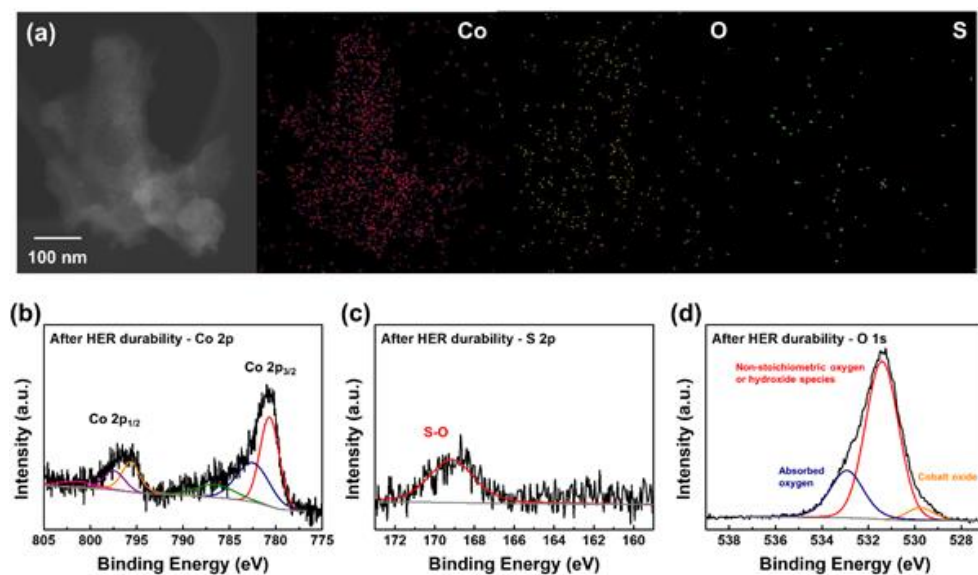


Figure 7.19 Chemical composition and electronic state change of MOF-driven CoS₂ after 20 hours HER stability test at -0.2 V (vs. RHE). (a) STEM image and EDS elemental mapping images in inset (cobalt: red, oxygen: yellow, sulfur: green). XPS analysis of MOF-driven CoS₂ after HER stability test. (b) Cobalt 2p, (c) sulfur 2p, and (d) oxygen 1s spectrum, respectively.

7.3. Summary

In summary, the metal-organic framework-driven cobalt disulfide was fabricated by predicted synthesis based on thermodynamic consideration, such as phase diagram and calculation of Gibbs free energy depending on sulfur vapor pressure. The hierarchical nanopore embedded and phase controlled structure that consists of MOF-driven porous CoS₂ nanoparticles is developed to the bifunctional electrocatalysts for electrochemical water splitting. Therefore, the electrocatalysts of designed structure achieved an overpotential of 298 mV and -198 mV at 10 and -10 mA cm⁻² in OER and HER conditions, respectively. Furthermore, in practical full-cell system, in which both electrodes consist of the same electrodes, the MOF-driven CoS₂ electrocatalyst achieved a 1.65 V at 10 mA cm⁻².

The nanopore embedded porous CoS₂ is essential for high exposure of active sites for bifunctional electrocatalysts. The nanopore and porous structure caused by decomposition and sulfurization of metal-organic framework were confirmed through electrochemical and physical adsorption characterization.

The controlling the phase is essential for enhanced oxygen and hydrogen evolution catalytic performance since catalytic performance differs to depending on the phase when various phases of the transition metal compound exist.

From the investigation of the electrochemical characterization of the MOF-driven CoS₂ electrode, the electrocatalytic performance of water splitting was high due to the kinetically favorable porous structure. Furthermore, the possibility of bifunctional electrocatalyst was confirmed with a full-cell system.

CHAPTER 8

Conclusion

8.1. Summary of results

The aim of this study is to develop a methodology that can be simply doped and precisely control the phase of transition metal compounds through thermodynamic consideration, which is used as the electrodes for the electrochemical water splitting. First, Doping the heteroatom in transition metal compounds is critical to the performance of the water oxidation electrocatalysts because it controls the intrinsic conductivity of electrocatalysts, which corresponds to the charge transfer and catalytic activity. However, heteroatom, especially boron, required a high temperature to dope transition metal compounds. Second, controlling the phase of transition metal compounds is critical to the performance of most water splitting electrocatalysts since catalytic activity differs depending on the its phase.

First, for the fabrication of boron doped nickel iron layered double hydroxide with electrochemical oxidation electrocatalyst for water oxidation, hydrothermal condition is optimized to enhanced catalytic performance through atomic ratio of nickel and iron. By adding an appropriate proportion of iron precursor, an electrocatalyst with improved

Chapter 8: Conclusion

performance compared to only nickel precursor was synthesized according to the previous reports. After the hydrothermal step, the simple boronization was conducted. Efficient OER electrocatalyst of hierarchically designed structure to facilitate charge transfer is suggested using gaseous boronization. It was conducted through annealing of NiFe LDH and boron source. The boronization should be easy to synthesize, in order to applying to mass production. The boronization was performed more simply through boron source with a relatively low boiling point. Next, after the boronization, formation of boron doped NiFe LDH, electrochemical oxidation is performed for improvement of active sites, which is applicable to large-scale because *in-situ* conversion with all electrochemical cell configurations in the same state. The boron doped NiFe LDH with electrochemical oxidation confirmed that oxyhydroxides were formed on the surface. This electrochemical oxidation step was designed by thermodynamic consideration through Pourbaix diagram. In additions, the kinetics change of electrochemical oxidation according to the difference in current density was verified. The hierarchical structure that consists of boron doped NiFe LDH with electrochemical oxidation is developed to the OER electrocatalysts for water splitting. Therefore, the electrocatalyst of designed structure achieved an overpotential of 229 mV at 10 mA cm^{-2} , which confirmed that it was approximately 140 and 85 mV lower than Ir and pristine NiFe LDH under the same conditions, respectively.

Second, for the fabrication of metal-organic framework-driven cobalt disulfide for efficient bifunctional electrocatalyst, the porous structure, such as nanopores, and controlling the phase are effectively formed by the sulfur vapor pressure controlled sulfurization. The performance of the synthesized transition metal sulfide electrocatalyst was confirmed to be high by maximizing the exposure of the active sites without addition of other materials. The synthesized catalyst showed extremely porous structure, which for improve performance by facilitating gas emission. Furthermore, calculation

Chapter 8: Conclusion

based on thermodynamics was applied to reduce trial & error, which is unique approach unlike conventional catalyst synthesis. It is possible to find the synthetic condition for fabricating the target phase that are predicted to have the most suitable electrocatalytic activity. In this work, metal-organic framework was used for extremely porous CoS₂ synthesis. By annealing the MOF with sulfur at predictive condition, organic linkers were removed and mono-phase CoS₂ was synthesized. Not only that, this methodology is variously applicable to all types of MOFs. Our synthesized material shows highly open structure and one of the most excellent catalytic performance among mono-phase CoS₂ electrocatalysts, whose overpotentials of the oxygen evolution, hydrogen evolution, and overall water splitting under the operating conditions were 298 mV, -196 mV, and 1.65 V, respectively at 10 mA cm⁻².

It is confident that the simple doping, structural, and phase controlled methodology in this work will give a new direction for water splitting system, which has the advantage of possible to apply variously as well. Therefore, it is expected that this work has the potential as an advanced research tool exploring the group of materials exhibiting potential for achieving performance enhancement.

8.2. Future works and suggested research

First, for the electrocatalysts of water oxidation, the transition metal borides have been reported. The transition metal borides are known to have a high intrinsic conductivity, and accordingly, charge transfer resistance is reported to be relatively lower than other transition metal compounds including oxide. However, fabrication of transition metal boride requires a higher temperature than boron doping, and is generally difficult. Therefore, it is necessary to find suitable boron based precursor and relative low temperature process conditions by design through thermodynamic calculation.

Here, we have currently developed the NiB₂ fabrication at low temperatures, and process parameters are being optimized. The structure for proposing the optimum water oxidation catalyst performance through combination with transition metal boride and electrochemical oxidation is under development. Furthermore, it will be proved by density function theory (DFT).

Second, for the electrocatalysts of water oxidation, the sulfur vacancy-induced cobalt disulfide is being studied. In order to develop an efficient water oxidation electrocatalyst, as mentioned continuously in this work, it should be accompanied by intrinsic conductivity. By artificially creating sulfur vacancy, it is possible to improve the intrinsic conductivity of cobalt disulfide. The overall summary of this concept is shown in Figure 8.1. After synthesizing the MOF-driven CoS₂ used in this work as shown in top of Figure 8.1, sulfur vacancy can be formed through CO gas having high reactivity in bottom of Figure 8.1.

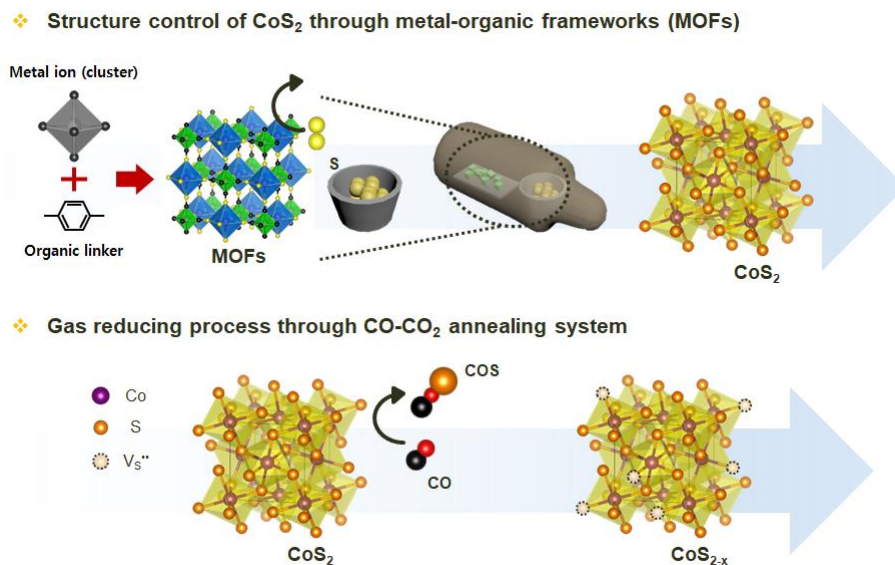


Figure 8.1 Schematic diagram of sulfur vacancy induced cobalt disulfide.

CO combines with sulfur to form COS gas, which leads to vacancies in the sulfur sites. Reduction annealing through a gas with high reduction reactivity such as CO, H₂ has already been confirmed through MoS₂ in our group, and could be applicable to oxide and chalcogenide groups as a whole. In addition, this CO annealing is applicable not only to particles, but also to various structures such as nanowire, nanoplate, and film.

According to the initial results, it was confirmed that COS is formed by CO regardless of nanoparticles and nanoplates, and this lead to phase transition or sulfur vacancy. As shown in the XRD results of Figure 8.2, sulfur extraction in MOF-driven CoS₂ occurs according to time, CO concentration, and temperature. Furthermore, similar results are seen in the form of nanoplates for reaction time in Figure 8.3. The FE-SEM and XRD results of the nanoplates are shown in Figure 8.4.

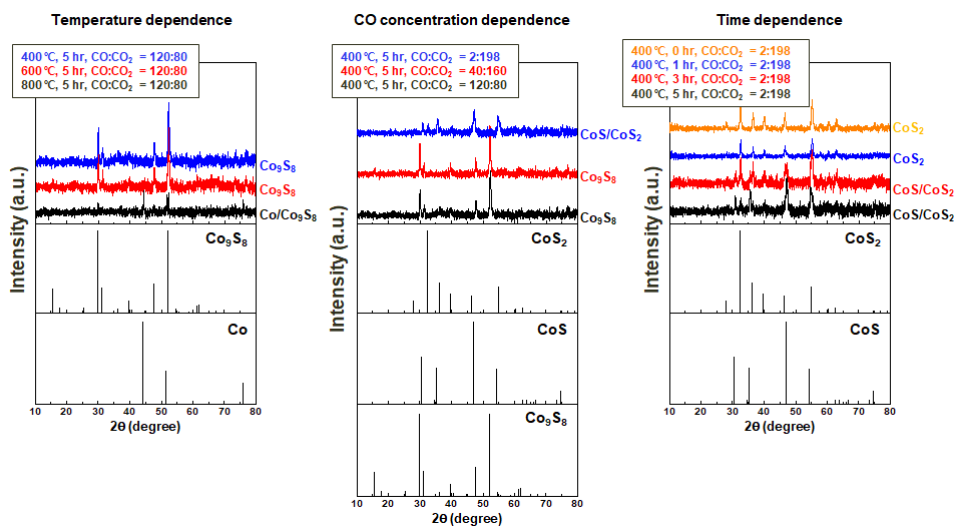


Figure 8.2 XRD analysis of sulfur vacancy induced MOF-driven CoS_2 depending on the reaction temperature, CO concentration, and time.

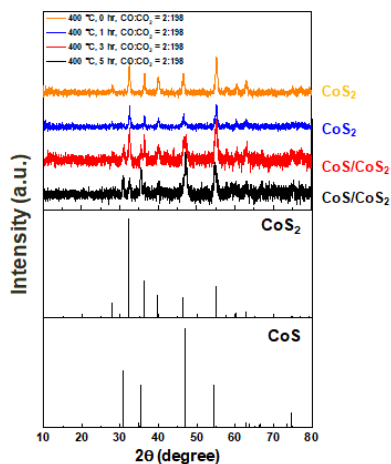


Figure 8.3 XRD analysis of sulfur vacancy induced CoS_2 nanoplates, sulfurized cobalt based nanostructure, depending on the reaction time.

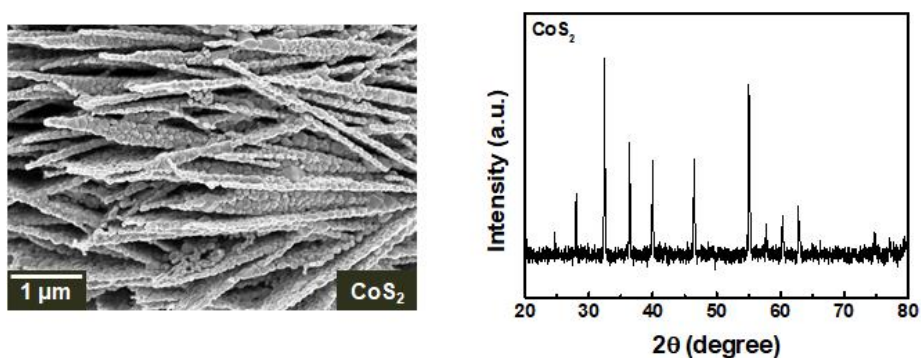


Figure 8.4 FE-SEM and XRD analysis of CoS_2 nanoplates. The CoS_2 nanoplates from thermally sulfurized cobalt hydroxycarbonates through hydrothermal.

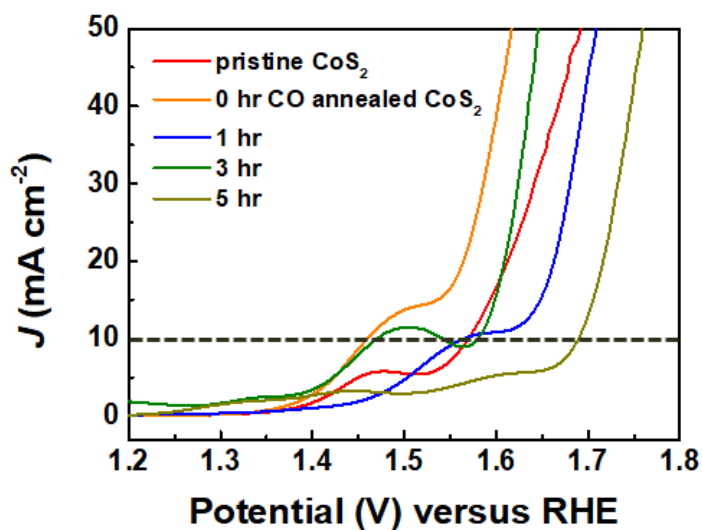


Figure 8.5 Electrochemical characterization of sulfur vacancy induced MOF-driven CoS_2 for water oxidation in 1.0 M KOH. The OER polarization curves through LSV of different CO annealing conditions with a scan rate 5.0 mV s^{-1} .

Chapter 8: Conclusion

Although it is still an initial result that requires optimization, the associated OER performance of sulfur vacancy induced MOF-driven CoS₂ is shown in Figure 8.5. MOF-driven CoS₂, which is estimated to have induced sulfur vacancy, showed the best OER catalyst performance.

Finally, one of the ultimate goal is to apply a membrane electrode assembly (MEA) system for electrochemical water splitting that can be applied in a large-scale than a conventional three-electrode electrochemical cell. As mentioned in Chapter 2, MEA will be implemented through the anion exchange membrane (AEM) system using alkaline electrolyte among MEA cells. The cathode in charge of HER will use MOF-driven CoS₂ with high efficiency in alkaline media, and the anode in charge of OER can use bifunctional electrocatalyst through MOF-driven CoS₂ like cathode. Alternatively, galox-B:NiFe LDH, which has more OER efficiency, can be used. It is expected that the setup of MEA system will show the possibility of mass production of electrochemical water splitting system.

References

- [1] Xia, B.Y., et al., *A metal–organic framework-derived bifunctional oxygen electrocatalyst*. *Nature Energy*, 2016. **1**(1).
- [2] Tahir, M., et al., *Electrocatalytic oxygen evolution reaction for energy conversion and storage: A comprehensive review*. *Nano Energy*, 2017. **37**: p. 136-157.
- [3] Ganesan, P., A. Sivanantham, and S. Shanmugam, *CoS₂–TiO₂ hybrid nanostructures: efficient and durable bifunctional electrocatalysts for alkaline electrolyte membrane water electrolyzers*. *Journal of Materials Chemistry A*, 2018. **6**(3): p. 1075-1085.
- [4] Yan, Y., et al., *A review on noble-metal-free bifunctional heterogeneous catalysts for overall electrochemical water splitting*. *Journal of Materials Chemistry A*, 2016. **4**(45): p. 17587-17603.
- [5] McCrory, C.C., et al., *Benchmarking hydrogen evolving reaction and oxygen evolving reaction electrocatalysts for solar water splitting devices*. *J Am Chem Soc*, 2015. **137**(13): p. 4347-57.
- [6] Yang, Y., et al., *Highly Active Trimetallic NiFeCr Layered Double Hydroxide Electrocatalysts for Oxygen Evolution Reaction*. *Advanced Energy Materials*, 2018. **8**(15): p. 1703189.
- [7] Ahn, I.K., et al., *Metal-organic Framework-driven Porous Cobalt Disulfide Nanoparticles Fabricated by Gaseous Sulfurization as Bifunctional Electrocatalysts for Overall Water Splitting*. *Sci Rep*, 2019. **9**(1): p. 19539.

- [8] Lu, Z., et al., *Three-dimensional NiFe layered double hydroxide film for high-efficiency oxygen evolution reaction*. Chem Commun (Camb), 2014. **50**(49): p. 6479-82.
- [9] Suen, N.T., et al., *Electrocatalysis for the oxygen evolution reaction: recent development and future perspectives*. Chem Soc Rev, 2017. **46**(2): p. 337-365.
- [10] Pei, C., et al., *Electrochemical oxygen evolution reaction efficiently catalyzed by a novel porous iron-cobalt-fluoride nanocube easily derived from 3-dimensional Prussian blue analogue*. Journal of Power Sources, 2019. **424**: p. 131-137.
- [11] Swesi, A.T., et al., *Textured NiSe₂ Film: Bifunctional Electrocatalyst for Full Water Splitting at Remarkably Low Overpotential with High Energy Efficiency*. Sci Rep, 2017. **7**(1): p. 2401.
- [12] Song, H.J., et al., *3D Architectures of Quaternary Co-Ni-S-P/Graphene Hybrids as Highly Active and Stable Bifunctional Electrocatalysts for Overall Water Splitting*. Advanced Energy Materials, 2018. **8**(33): p. 1802319.
- [13] Kim, J.-Y., et al., *Predictive fabrication of Ni phosphide embedded in carbon nanofibers as active and stable electrocatalysts*. Journal of Materials Chemistry A, 2019. **7**(13): p. 7451-7458.
- [14] Caban-Acevedo, M., et al., *Efficient hydrogen evolution catalysis using ternary pyrite-type cobalt phosphosulphide*. Nat Mater, 2015. **14**(12): p. 1245-51.

- [15] Zheng, M., et al., *In Situ Grown Pristine Cobalt Sulfide as Bifunctional Photocatalyst for Hydrogen and Oxygen Evolution*. *Advanced Functional Materials*, 2017. **27**(11): p. 1605846.
- [16] Sivanantham, A., P. Ganesan, and S. Shanmugam, *Hierarchical NiCo₂S₄Nanowire Arrays Supported on Ni Foam: An Efficient and Durable Bifunctional Electrocatalyst for Oxygen and Hydrogen Evolution Reactions*. *Advanced Functional Materials*, 2016. **26**(26): p. 4661-4672.
- [17] Park, H., et al., *Water Splitting Exceeding 17% Solar-to-Hydrogen Conversion Efficiency Using Solution-Processed Ni-Based Electrocatalysts and Perovskite/Si Tandem Solar Cell*. *ACS Appl Mater Interfaces*, 2019. **11**(37): p. 33835-33843.
- [18] Tachibana, Y., L. Vayssieres, and J.R. Durrant, *Artificial photosynthesis for solar water-splitting*. *Nature Photonics*, 2012. **6**(8): p. 511-518.
- [19] Osterloh, F.E. and B.A. Parkinson, *Recent developments in solar water-splitting photocatalysis*. *MRS Bulletin*, 2011. **36**(1): p. 17-22.
- [20] Smith, R.D., et al., *Water oxidation catalysis: electrocatalytic response to metal stoichiometry in amorphous metal oxide films containing iron, cobalt, and nickel*. *J Am Chem Soc*, 2013. **135**(31): p. 11580-6.
- [21] Trotochaud, L., et al., *Nickel-iron oxyhydroxide oxygen-evolution electrocatalysts: the role of intentional and incidental iron incorporation*. *J Am Chem Soc*, 2014. **136**(18): p. 6744-53.
- [22] Murthy, A.P., J. Madhavan, and K. Murugan, *Recent advances in hydrogen evolution reaction catalysts on carbon/carbon-based supports in acid media*. *Journal of Power Sources*, 2018. **398**: p. 9-26.

- [23] Zhang, Q., et al., *Self-Interconnected Porous Networks of NiCo Disulfide as Efficient Bifunctional Electrocatalysts for Overall Water Splitting*. ACS Appl Mater Interfaces, 2018. **10**(33): p. 27723-27733.
- [24] Lim, S.Y., et al., *Chemically Deposited Amorphous Zn-Doped NiFeOxHy for Enhanced Water Oxidation*. ACS Catalysis, 2019. **10**(1): p. 235-244.
- [25] Seo, H., et al., *Water Oxidation Mechanism for 3d Transition Metal Oxide Catalysts under Neutral Condition*. Journal of the Korean Ceramic Society, 2017. **54**(1): p. 1-8.
- [26] Cai, Z., et al., *Recent advances in layered double hydroxide electrocatalysts for the oxygen evolution reaction*. Journal of Materials Chemistry A, 2019. **7**(10): p. 5069-5089.
- [27] Diaz-Morales, O., et al., *Guidelines for the Rational Design of Ni-Based Double Hydroxide Electrocatalysts for the Oxygen Evolution Reaction*. ACS Catalysis, 2015. **5**(9): p. 5380-5387.
- [28] Seh, Z.W., et al., *Combining theory and experiment in electrocatalysis: Insights into materials design*. Science, 2017. **355**(6321).
- [29] Gong, M., et al., *An advanced Ni-Fe layered double hydroxide electrocatalyst for water oxidation*. J Am Chem Soc, 2013. **135**(23): p. 8452-5.
- [30] Hou, Y., et al., *Vertically oriented cobalt selenide/NiFe layered-double-hydroxide nanosheets supported on exfoliated graphene foil: an efficient 3D electrode for overall water splitting*. Energy & Environmental Science, 2016. **9**(2): p. 478-483.

- [31] Hunter, B.M., et al., *Effect of interlayer anions on [NiFe]-LDH nanosheet water oxidation activity*. Energy & Environmental Science, 2016. **9**(5): p. 1734-1743.
- [32] Hao, J., et al., *Nitrogen doped NiS₂ nanoarrays with enhanced electrocatalytic activity for water oxidation*. Journal of Materials Chemistry A, 2017. **5**(34): p. 17811-17816.
- [33] Zhang, Y., et al., *Cobalt-molybdenum nanosheet arrays as highly efficient and stable earth-abundant electrocatalysts for overall water splitting*. Nano Energy, 2018. **45**: p. 448-455.
- [34] Zheng, X., et al., *Controllable synthesis of nickel sulfide nanocatalysts and their phase-dependent performance for overall water splitting*. Nanoscale, 2019. **11**(12): p. 5646-5654.
- [35] Li, Y., et al., *Recent Advances on Water-Splitting Electrocatalysis Mediated by Noble-Metal-Based Nanostructured Materials*. Advanced Energy Materials, 2020. **10**(11): p. 1903120.
- [36] Reier, T., M. Oezaslan, and P. Strasser, *Electrocatalytic Oxygen Evolution Reaction (OER) on Ru, Ir, and Pt Catalysts: A Comparative Study of Nanoparticles and Bulk Materials*. ACS Catalysis, 2012. **2**(8): p. 1765-1772.
- [37] Posevins, D., Y. Qiu, and J.E. Backvall, *Highly Diastereoselective Palladium-Catalyzed Oxidative Carbocyclization of Enallenes Assisted by a Weakly Coordinating Hydroxyl Group*. J Am Chem Soc, 2018. **140**(9): p. 3210-3214.
- [38] Park, J., et al., *Hemi-core@frame AuCu@IrNi nanocrystals as active and durable bifunctional catalysts for the water splitting reaction in acidic media*. Nanoscale Horizons, 2019. **4**(3): p. 727-734.

- [39] Roger, I., M.A. Shipman, and M.D. Symes, *Earth-abundant catalysts for electrochemical and photoelectrochemical water splitting*. Nature Reviews Chemistry, 2017. **1**(1).
- [40] Lingzheng Bu, et al., *Biaxiallystrained PtPb/Ptcore/shell nanoplateboosts oxygen reduction catalysis*. Science, 2016. **354**.
- [41] Fan, G., et al., *Catalytic applications of layered double hydroxides: recent advances and perspectives*. Chem Soc Rev, 2014. **43**(20): p. 7040-66.
- [42] Shahraei, A., et al., *On the role of hydroxide species in sulphur- and nitrogen-doped cobalt-based carbon catalysts for the oxygen evolution reaction*. Journal of Materials Chemistry A, 2018. **6**(44): p. 22310-22319.
- [43] Cao, L.-M., et al., *Template-directed synthesis of sulphur doped NiCoFe layered double hydroxide porous nanosheets with enhanced electrocatalytic activity for the oxygen evolution reaction*. Journal of Materials Chemistry A, 2018. **6**(7): p. 3224-3230.
- [44] Lu, Q. and F. Jiao, *Electrochemical CO₂ reduction: Electrocatalyst, reaction mechanism, and process engineering*. Nano Energy, 2016. **29**: p. 439-456.
- [45] Wan, Y., J. Xu, and R. Lv, *Heterogeneous electrocatalysts design for nitrogen reduction reaction under ambient conditions*. Materials Today, 2019. **27**: p. 69-90.
- [46] Gao, R., et al., *An amorphous LiO₂-based Li-O₂ battery with low overpotential and high rate capability*. Nano Energy, 2017. **41**: p. 535-542.
- [47] Xue, X., et al., *One-step synthesis of nickel–iron layered double hydroxides with tungstate acid anions via flash nano-precipitation for the oxygen evolution reaction*. Sustainable Energy & Fuels, 2019. **3**(1): p. 237-244.

- [48] Faber, M.S., et al., *Earth-Abundant Metal Pyrites (FeS₂, CoS₂, NiS₂, and Their Alloys) for Highly Efficient Hydrogen Evolution and Polysulfide Reduction Electrocatalysis*. J Phys Chem C Nanomater Interfaces, 2014. **118**(37): p. 21347-21356.
- [49] Zhang, N., et al., *Sulfur encapsulation by MOF-derived CoS₂ embedded in carbon hosts for high-performance Li-S batteries*. Journal of Materials Chemistry A, 2019. **7**(37): p. 21128-21139.
- [50] Xie, J., et al., *Self-assembly of CoS₂/graphene nanoarchitecture by a facile one-pot route and its improved electrochemical Li-storage properties*. Nano Energy, 2013. **2**(1): p. 49-56.
- [51] Yang, J., et al., *Highly efficient oxygen evolution from CoS₂/CNT nanocomposites via a one-step electrochemical deposition and dissolution method*. Nanoscale, 2017. **9**(20): p. 6886-6894.
- [52] Ma, D., et al., *Highly active nanostructured CoS₂/CoS heterojunction electrocatalysts for aqueous polysulfide/iodide redox flow batteries*. Nat Commun, 2019. **10**(1): p. 3367.
- [53] Zou, X., A. Goswami, and T. Asefa, *Efficient noble metal-free (electro)catalysis of water and alcohol oxidations by zinc-cobalt layered double hydroxide*. J Am Chem Soc, 2013. **135**(46): p. 17242-5.
- [54] Yang, Y., et al., *A facile method to synthesize boron-doped Ni/Fe alloy nano-chains as electrocatalyst for water oxidation*. Journal of Power Sources, 2017. **349**: p. 68-74.
- [55] Song, F. and X. Hu, *Exfoliation of layered double hydroxides for enhanced oxygen evolution catalysis*. Nat Commun, 2014. **5**: p. 4477.

- [56] Hong, J.S., et al., *Nickel-Doping Effect on Mn₃O₄ Nanoparticles for Electrochemical Water Oxidation under Neutral Condition*. *Small Methods*, 2020. **4**(3): p. 1900733.
- [57] Cacciamani, G., et al., *The Fe–Ni system: Thermodynamic modelling assisted by atomistic calculations*. *Intermetallics*, 2010. **18**(6): p. 1148-1162.
- [58] Louie, M.W. and A.T. Bell, *An investigation of thin-film Ni-Fe oxide catalysts for the electrochemical evolution of oxygen*. *J Am Chem Soc*, 2013. **135**(33): p. 12329-37.
- [59] Guo, F., et al., *High-performance oxygen evolution electrocatalysis by boronized metal sheets with self-functionalized surfaces*. *Energy & Environmental Science*, 2019. **12**(2): p. 684-692.
- [60] Li, J., et al., *In situ structural evolution of a nickel boride catalyst: synergistic geometric and electronic optimization for the oxygen evolution reaction*. *Journal of Materials Chemistry A*, 2019. **7**(10): p. 5288-5294.
- [61] Masa, J., et al., *Ultrathin High Surface Area Nickel Boride (Ni_xB) Nanosheets as Highly Efficient Electrocatalyst for Oxygen Evolution*. *Advanced Energy Materials*, 2017. **7**(17): p. 1700381.
- [62] Li, W., et al., *The oxygen evolution reaction enabled by transition metal phosphide and chalcogenide pre-catalysts with dynamic changes*. *Chem Commun (Camb)*, 2019. **55**(60): p. 8744-8763.
- [63] Zhang, J., et al., *Single-Atom Au/NiFe Layered Double Hydroxide Electrocatalyst: Probing the Origin of Activity for Oxygen Evolution Reaction*. *J Am Chem Soc*, 2018. **140**(11): p. 3876-3879.

- [64] Kwak, I.H., et al., *CoSe(2) and NiSe(2) Nanocrystals as Superior Bifunctional Catalysts for Electrochemical and Photoelectrochemical Water Splitting*. ACS Appl Mater Interfaces, 2016. **8**(8): p. 5327-34.
- [65] Xin, W., et al., *NiS₂ nanodotted carnation-like CoS₂ for enhanced electrocatalytic water splitting*. Chem Commun (Camb), 2019. **55**(26): p. 3781-3784.
- [66] Wang, D., et al., *In Situ Preparation of Mo₂C Nanoparticles Embedded in Ketjenblack Carbon as Highly Efficient Electrocatalysts for Hydrogen Evolution*. ACS Sustainable Chemistry & Engineering, 2017. **6**(1): p. 983-990.
- [67] Zhang, H., et al., *A metallic CoS₂ nanopyramid array grown on 3D carbon fiber paper as an excellent electrocatalyst for hydrogen evolution*. Journal of Materials Chemistry A, 2015. **3**(12): p. 6306-6310.
- [68] Xiang, Z., et al., *Multiscale simulation and modelling of adsorptive processes for energy gas storage and carbon dioxide capture in porous coordination frameworks*. Energy & Environmental Science, 2010. **3**(10): p. 1469.
- [69] Masset, P.J. and R.A. Guidotti, *Thermal activated ("thermal") battery technology*. Journal of Power Sources, 2008. **178**(1): p. 456-466.
- [70] Li, Z., et al., *Pyrite FeS₂/C nanoparticles as an efficient bi-functional catalyst for overall water splitting*. Dalton Trans, 2018. **47**(42): p. 14917-14923.
- [71] Liu, H., et al., *Electronic Structure Reconfiguration toward Pyrite NiS₂ via Engineered Heteroatom Defect Boosting Overall Water Splitting*. ACS Nano, 2017. **11**(11): p. 11574-11583.

- [72] Faber, M.S., et al., *High-performance electrocatalysis using metallic cobalt pyrite (CoS(2)) micro- and nanostructures*. J Am Chem Soc, 2014. **136**(28): p. 10053-61.
- [73] Guan, C., et al., *Metal-organic framework derived hollow CoS₂ nanotube arrays: an efficient bifunctional electrocatalyst for overall water splitting*. Nanoscale Horiz., 2017. **2**(6): p. 342-348.
- [74] Hu, C., L. Zhang, and J. Gong, *Recent progress made in the mechanism comprehension and design of electrocatalysts for alkaline water splitting*. Energy & Environmental Science, 2019. **12**(9): p. 2620-2645.
- [75] Marini, S., et al., *Advanced alkaline water electrolysis*. Electrochimica Acta, 2012. **82**: p. 384-391.
- [76] Song, F., et al., *Transition Metal Oxides as Electrocatalysts for the Oxygen Evolution Reaction in Alkaline Solutions: An Application-Inspired Renaissance*. J Am Chem Soc, 2018. **140**(25): p. 7748-7759.
- [77] Ma, Z., et al., *Reaction mechanism for oxygen evolution on RuO₂, IrO₂, and RuO₂@IrO₂ core-shell nanocatalysts*. Journal of Electroanalytical Chemistry, 2018. **819**: p. 296-305.
- [78] Dau, H., et al., *The Mechanism of Water Oxidation: From Electrolysis via Homogeneous to Biological Catalysis*. ChemCatChem, 2010. **2**(7): p. 724-761.
- [79] R. Gómez, et al., *Hydrogen Evolution on Pt Single Crystal Surfaces. Effects of Irreversibly Adsorbed Bismuth and Antimony on Hydrogen Adsorption and Evolution on Pt(100)*. J. Phys. Chem., 1993. **97**: p. 4769-4776.

- [80] Skulason, E., et al., *Density functional theory calculations for the hydrogen evolution reaction in an electrochemical double layer on the Pt(111) electrode*. *Phys Chem Chem Phys*, 2007. **9**(25): p. 3241-50.
- [81] Wenchao Sheng, Hubert A. Gasteiger, and a.Y. Shao-Horn, *Hydrogen Oxidation and Evolution Reaction Kinetics on Platinum: Acid vs Alkaline Electrolytes*. *Journal of The Electrochemical Society*, 2010. **157**(11): p. B1529-B1536.
- [82] Nenad M. Markovic, et al., *Hydrogen electrochemistry on platinum low-index single-crystal surfaces in alkaline solution*. *J. Chem. Soc., Faraday Trans.*, 1996. **92**(20): p. 3719-3725.
- [83] Zeng, M. and Y. Li, *Recent advances in heterogeneous electrocatalysts for the hydrogen evolution reaction*. *Journal of Materials Chemistry A*, 2015. **3**(29): p. 14942-14962.
- [84] Wang, Y., et al., *Recent Progress on Layered Double Hydroxides and Their Derivatives for Electrocatalytic Water Splitting*. *Adv Sci (Weinh)*, 2018. **5**(8): p. 1800064.
- [85] Rossmeisl, J., A. Logadottir, and J.K. Nørskov, *Electrolysis of water on (oxidized) metal surfaces*. *Chemical Physics*, 2005. **319**(1-3): p. 178-184.
- [86] Rossmeisl, J., et al., *Electrolysis of water on oxide surfaces*. *Journal of Electroanalytical Chemistry*, 2007. **607**(1-2): p. 83-89.
- [87] Liang, H., et al., *Hydrothermal continuous flow synthesis and exfoliation of NiCo layered double hydroxide nanosheets for enhanced oxygen evolution catalysis*. *Nano Lett*, 2015. **15**(2): p. 1421-7.
- [88] Hua, Y., et al., *Hierarchical porous CoS₂ microboxes for efficient oxygen evolution reaction*. *Electrochimica Acta*, 2018. **278**: p. 219-225.

- [89] Han, X., et al., *Ultrafine Pt Nanoparticle-Decorated Pyrite-Type CoS₂ Nanosheet Arrays Coated on Carbon Cloth as a Bifunctional Electrode for Overall Water Splitting*. *Advanced Energy Materials*, 2018. **8**(24): p. 1800935.
- [90] Sivanantham, A., et al., *A Stable Graphitic, Nanocarbon-Encapsulated, Cobalt-Rich Core-Shell Electrocatalyst as an Oxygen Electrode in a Water Electrolyzer*. *Advanced Energy Materials*, 2018. **8**(14): p. 1702838.
- [91] Chu, H., et al., *Impact of morphology on the oxygen evolution reaction of 3D hollow Cobalt-Molybdenum Nitride*. *Applied Catalysis B: Environmental*, 2019. **255**: p. 117744.
- [92] He, P., X.Y. Yu, and X.W. Lou, *Carbon-Incorporated Nickel-Cobalt Mixed Metal Phosphide Nanoboxes with Enhanced Electrocatalytic Activity for Oxygen Evolution*. *Angew Chem Int Ed Engl*, 2017. **56**(14): p. 3897-3900.
- [93] Xue, Z.-H., et al., *Janus Co/CoP Nanoparticles as Efficient Mott-Schottky Electrocatalysts for Overall Water Splitting in Wide pH Range*. *Advanced Energy Materials*, 2017. **7**(12): p. 1602355.
- [94] Mai, H.D., V.C.T. Le, and H. Yoo, *Effective Fabrication and Electrochemical Oxygen Evolution Reaction Activity of Gold Multipod Nanoparticle Core-Cobalt Sulfide Shell Nanohybrids*. *ACS Applied Nano Materials*, 2019. **2**(2): p. 678-688.
- [95] Fang, G., et al., *Metal Organic Framework-Templated Synthesis of Bimetallic Selenides with Rich Phase Boundaries for Sodium-Ion Storage and Oxygen Evolution Reaction*. *ACS Nano*, 2019. **13**(5): p. 5635-5645.

- [96] Tang, Y., et al., *Cobalt and nitrogen codoped ultrathin porous carbon nanosheets as bifunctional electrocatalysts for oxygen reduction and evolution*. Carbon, 2019. **141**: p. 704-711.
- [97] Wu, H., et al., *Topotactic Engineering of Ultrathin 2D Nonlayered Nickel Selenides for Full Water Electrolysis*. Advanced Energy Materials, 2018. **8**(14): p. 1702704.
- [98] Fang, L., et al., *Tuning Unique Peapod-Like $\text{Co}(\text{S}_x\text{Se}_{1-x})_2$ Nanoparticles for Efficient Overall Water Splitting*. Advanced Functional Materials, 2017. **27**(24): p. 1701008.
- [99] Lu, X. and C. Zhao, *Electrodeposition of hierarchically structured three-dimensional nickel-iron electrodes for efficient oxygen evolution at high current densities*. Nat Commun, 2015. **6**: p. 6616.
- [100] Li, Z., et al., *Fast electrosynthesis of Fe-containing layered double hydroxide arrays toward highly efficient electrocatalytic oxidation reactions*. Chem Sci, 2015. **6**(11): p. 6624-6631.
- [101] Jia, Y., et al., *A Heterostructure Coupling of Exfoliated Ni-Fe Hydroxide Nanosheet and Defective Graphene as a Bifunctional Electrocatalyst for Overall Water Splitting*. Adv Mater, 2017. **29**(17).
- [102] Dang, L., et al., *Direct Synthesis and Anion Exchange of Noncarbonate-Intercalated NiFe-Layered Double Hydroxides and the Influence on Electrocatalysis*. Chemistry of Materials, 2018. **30**(13): p. 4321-4330.
- [103] Zhu, J., et al., *Recent Advances in Electrocatalytic Hydrogen Evolution Using Nanoparticles*. Chem Rev, 2020. **120**(2): p. 851-918.

- [104] Mahmood, N., et al., *Electrocatalysts for Hydrogen Evolution in Alkaline Electrolytes: Mechanisms, Challenges, and Prospective Solutions*. Adv Sci (Weinh), 2018. **5**(2): p. 1700464.
- [105] PARSONS, R., *THE RATE OF ELECTROLYTIC HYDROGEN EVOLUTION AND THE HEAT OF ADSORPTION OF HYDROGEN* Transactions of the Faraday Society, 1958. **54**: p. 1053-1063.
- [106] Wang, J., et al., *Integrated Three-Dimensional Carbon Paper/Carbon Tubes/Cobalt-Sulfide Sheets as an Efficient Electrode for Overall Water Splitting*. ACS Nano, 2016. **10**(2): p. 2342-8.
- [107] Tian, T., et al., *Surface anion-rich NiS₂ hollow microspheres derived from metal–organic frameworks as a robust electrocatalyst for the hydrogen evolution reaction*. J. Mater. Chem. A, 2017. **5**(39): p. 20985-20992.
- [108] Yu, J., G. Cheng, and W. Luo, *Ternary nickel–iron sulfide microflowers as a robust electrocatalyst for bifunctional water splitting*. Journal of Materials Chemistry A, 2017. **5**(30): p. 15838-15844.
- [109] Dubal, D.P., et al., *A novel chemical synthesis of Mn₃O₄ thin film and its stepwise conversion into birnessite MnO₂ during super capacitive studies*. Journal of Electroanalytical Chemistry, 2010. **647**(1): p. 60-65.
- [110] Lee, M., et al., *Activation of a Ni electrocatalyst through spontaneous transformation of nickel sulfide to nickel hydroxide in an oxygen evolution reaction*. Applied Catalysis B: Environmental, 2018. **233**: p. 130-135.
- [111] Chi-Chang Hu, Yung-Tai Wu, and a.K.-H. Chang, *Low-Temperature Hydrothermal Synthesis of Mn₃O₄ and MnOOH Single Crystals: Determinant Influence of Oxidants*. Chem. Mater., 2008. **20**: p. 2890–2894.

- [112] A. Kozawa and a.J.F. Yeager, *The Cathodic Reduction Mechanism of Electrolytic Manganese Dioxide in Alkaline Electrolyte* Journal of The Electrochemical Society, 1965. **112**: p. 959-963.
- [113] D. Y. QU, B. E. CONWAY, and L. BAI, *Role of dissolution of Mn(III) species in discharge and recharge of chemically-modified MnO₂ battery cathode materials.* JOURNAL OF APPLIED ELECTROCHEMISTRY 1993. **23**: p. 693-706.
- [114] Xu, X., F. Song, and X. Hu, *A nickel iron diselenide-derived efficient oxygen-evolution catalyst.* Nat Commun, 2016. **7**: p. 12324.
- [115] Lee, J.-H., et al., *Designing thermal and electrochemical oxidation processes for δ -MnO₂ nanofibers for high-performance electrochemical capacitors.* J. Mater. Chem. A, 2014. **2**(20): p. 7197-7204.
- [116] J. N. Broughton and a.M.J. Brett, *Electrochemical Capacitance in Manganese Thin Films with Chevron Microstructure.* Electrochemical and Solid-State Letters, 2002. **5**: p. A279-A282.
- [117] Vincent, I. and D. Bessarabov, *Low cost hydrogen production by anion exchange membrane electrolysis: A review.* Renewable and Sustainable Energy Reviews, 2018. **81**: p. 1690-1704.
- [118] Deng, S., et al., *Hollow TiO₂@Co₉S₈ Core-Branch Arrays as Bifunctional Electrocatalysts for Efficient Oxygen/Hydrogen Production.* Adv Sci (Weinh), 2018. **5**(3): p. 1700772.
- [119] Xiao, C., et al., *Bifunctional Porous NiFe/NiCo₂O₄/Ni Foam Electrodes with Triple Hierarchy and Double Synergies for Efficient Whole Cell Water Splitting.* Advanced Functional Materials, 2016. **26**(20): p. 3515-3523.

- [120] Dinh, K.N., et al., *Ultrathin Porous NiFeV Ternary Layer Hydroxide Nanosheets as a Highly Efficient Bifunctional Electrocatalyst for Overall Water Splitting*. *Small*, 2018. **14**(8).
- [121] Liu, H., et al., *The effects of Al substitution and partial dissolution on ultrathin NiFeAl ternary layered double hydroxide nanosheets for oxygen evolution reaction in alkaline solution*. *Nano Energy*, 2017. **35**: p. 350-357.
- [122] Cao, X., et al., *Phase Exploration and Identification of Multinary Transition-Metal Selenides as High-Efficiency Oxygen Evolution Electrocatalysts through Combinatorial Electrodeposition*. *ACS Catalysis*, 2018. **8**(9): p. 8273-8289.
- [123] Long, X., et al., *Co intake mediated formation of ultrathin nanosheets of transition metal LDH-an advanced electrocatalyst for oxygen evolution reaction*. *Chem Commun (Camb)*, 2015. **51**(6): p. 1120-3.
- [124] Lu, Z., et al., *Ternary NiFeMn layered double hydroxides as highly-efficient oxygen evolution catalysts*. *Chem Commun (Camb)*, 2016. **52**(5): p. 908-11.
- [125] Tan, Z., et al., *An in situ vapour phase hydrothermal surface doping approach for fabrication of high performance Co₃O₄ electrocatalysts with an exceptionally high S-doped active surface*. *Chem Commun (Camb)*, 2015. **51**(26): p. 5695-7.
- [126] Xu, W., et al., *Sulphur-doped Co₃O₄ nanowires as an advanced negative electrode for high-energy asymmetric supercapacitors*. *Journal of Materials Chemistry A*, 2016. **4**(28): p. 10779-10785.
- [127] Yang, T.-Y., et al., *An iron oxide photoanode with hierarchical nanostructure for efficient water oxidation*. *J. Mater. Chem. A*, 2014. **2**(7): p. 2297-2305.

- [128] Yang, T.Y., et al., *A new hematite photoanode doping strategy for solar water splitting: oxygen vacancy generation*. *Phys Chem Chem Phys*, 2013. **15**(6): p. 2117-24.
- [129] Bediako, D.K., et al., *Structure-activity correlations in a nickel-borate oxygen evolution catalyst*. *J Am Chem Soc*, 2012. **134**(15): p. 6801-9.
- [130] Jin, S., *Are Metal Chalcogenides, Nitrides, and Phosphides Oxygen Evolution Catalysts or Bifunctional Catalysts?* *ACS Energy Letters*, 2017. **2**(8): p. 1937-1938.
- [131] Stern, L.-A., et al., *Ni₂P as a Janus catalyst for water splitting: the oxygen evolution activity of Ni₂P nanoparticles*. *Energy & Environmental Science*, 2015. **8**(8): p. 2347-2351.
- [132] Chen, W., et al., *In Situ Electrochemically Derived Nanoporous Oxides from Transition Metal Dichalcogenides for Active Oxygen Evolution Catalysts*. *Nano Lett*, 2016. **16**(12): p. 7588-7596.
- [133] Wang, X., et al., *Bifunctional Nickel Phosphide Nanocatalysts Supported on Carbon Fiber Paper for Highly Efficient and Stable Overall Water Splitting*. *Advanced Functional Materials*, 2016. **26**(23): p. 4067-4077.
- [134] Wang, X., et al., *Fast fabrication of self-supported porous nickel phosphide foam for efficient, durable oxygen evolution and overall water splitting*. *Journal of Materials Chemistry A*, 2016. **4**(15): p. 5639-5646.
- [135] Chen, W., et al., *In Situ Electrochemical Oxidation Tuning of Transition Metal Disulfides to Oxides for Enhanced Water Oxidation*. *ACS Cent Sci*, 2015. **1**(5): p. 244-51.

- [136] Andrew D. Cross, et al., *Chronoamperometric Versus Galvanostatic Preparation of Manganese Oxides for Electrochemical Capacitors*. Journal of The Electrochemical Society, 2011. **158**(10): p. A1160-A1165.
- [137] Masa, J. and W. Schuhmann, *The Role of Non-Metallic and Metalloid Elements on the Electrocatalytic Activity of Cobalt and Nickel Catalysts for the Oxygen Evolution Reaction*. ChemCatChem, 2019. **11**(24): p. 5842-5854.
- [138] Asrofi, M., et al., *Effect of duration of sonication during gelatinization on properties of tapioca starch water hyacinth fiber biocomposite*. Int J Biol Macromol, 2018. **108**: p. 167-176.
- [139] Drenchev, N.L., et al., *In situ FTIR Spectroscopy as a Tool for Investigation of Gas/Solid Interaction: Water-Enhanced CO₂ Adsorption in UiO-66 Metal-Organic Framework*. J Vis Exp, 2020(156).
- [140] Iliev, M.N., et al., *Monitoring B-site ordering and strain relaxation in NiFe₂O₄ epitaxial films by polarized Raman spectroscopy*. Physical Review B, 2011. **83**(1).
- [141] Romanos, J., et al., *Infrared study of boron-carbon chemical bonds in boron-doped activated carbon*. Carbon, 2013. **54**: p. 208-214.
- [142] Han, H., et al., *Electronically Double-Layered Metal Boride Hollow Nanoprism as an Excellent and Robust Water Oxidation Electrocatalysts*. Advanced Energy Materials, 2019. **9**(13): p. 1803799.
- [143] Ahn, I.K., et al., *Improved Battery Performance of Nanocrystalline Si Anodes Utilized by Radio Frequency (RF) Sputtered Multifunctional Amorphous Si Coating Layers*. ACS Appl Mater Interfaces, 2018. **10**(3): p. 2242-2248.

- [144] Lee, J.-H., et al., *The effect of energetically coated ZrO_x on enhanced electrochemical performances of Li(Ni_{1/3}Co_{1/3}Mn_{1/3})O₂ cathodes using modified radio frequency (RF) sputtering*. Journal of Materials Chemistry A, 2015. **3**(24): p. 12982-12991.
- [145] Matsoso, B.J., et al., *Synthesis and characterization of boron carbon oxynitride films with tunable composition using methane, boric acid and ammonia*. New Journal of Chemistry, 2017. **41**(17): p. 9497-9504.
- [146] Deng, H., et al., *Laser induced MoS₂/carbon hybrids for hydrogen evolution reaction catalysts*. Journal of Materials Chemistry A, 2016. **4**(18): p. 6824-6830.
- [147] Benck, J.D., et al., *Amorphous Molybdenum Sulfide Catalysts for Electrochemical Hydrogen Production: Insights into the Origin of their Catalytic Activity*. ACS Catalysis, 2012. **2**(9): p. 1916-1923.
- [148] You, B., et al., *High-Performance Overall Water Splitting Electrocatalysts Derived from Cobalt-Based Metal–Organic Frameworks*. Chemistry of Materials, 2015. **27**(22): p. 7636-7642.
- [149] Lu, Y., et al., *Prussian blue: a new framework of electrode materials for sodium batteries*. Chem Commun (Camb), 2012. **48**(52): p. 6544-6.
- [150] Middy, S., et al., *Synthesis of Nanocrystalline FeS₂ with Increased Band Gap for Solar Energy Harvesting*. Journal of Materials Science & Technology, 2014. **30**(8): p. 770-775.
- [151] T. A. BITHER, et al., *Transition Metal Pyrite Dichalcogenides. High-Pressure Synthesis and Correlation of Properties*. Inorganic Chemistry, 1968. **7**: p. 2208-2220.

- [152] Ouyang, C., X. Wang, and S. Wang, *Phosphorus-doped CoS₂ nanosheet arrays as ultra-efficient electrocatalysts for the hydrogen evolution reaction*. Chem Commun (Camb), 2015. **51**(75): p. 14160-3.
- [153] Wang, Y., et al., *Phase-controlled synthesis of cobalt sulfides for lithium ion batteries*. ACS Appl Mater Interfaces, 2012. **4**(8): p. 4246-50.
- [154] Zhou, J., et al., *MOF Template-Directed Fabrication of Hierarchically Structured Electrocatalysts for Efficient Oxygen Evolution Reaction*. Advanced Energy Materials, 2017. **7**(12): p. 1602643.
- [155] Feng, L.L., et al., *Carbon-armored Co₉S₈ nanoparticles as all-pH efficient and durable H₂-evolving electrocatalysts*. ACS Appl Mater Interfaces, 2015. **7**(1): p. 980-8.
- [156] Zhang, H., et al., *Facile preparation of Prussian blue analogue Co₃[Co(CN)₆]₂ with fine-tuning color transition temperature as thermochromic material*. CrystEngComm, 2017. **19**(15): p. 2057-2064.
- [157] Hu, L., et al., *Foamlike porous spinel Mn_(x)Co_(3-x)O₄ material derived from Mn₃[Co(CN)₆]₂nH₂O nanocubes: a highly efficient anode material for lithium batteries*. Chemistry, 2012. **18**(47): p. 15049-56.
- [158] Zhang, L., et al., *Rational Design of High-Performance DeNO_x Catalysts Based on Mn_xCo_{3-x}O₄ Nanocages Derived from Metal–Organic Frameworks*. ACS Catalysis, 2014. **4**(6): p. 1753-1763.
- [159] Wang, X.-F., et al., *Prussian Blue analogue derived porous NiFe₂O₄ nanocubes for low-concentration acetone sensing at low working temperature*. Chemical Engineering Journal, 2018. **338**: p. 504-512.

- [160] Ren, J., et al., *CoS₂ hollow nanocubes derived from Co-Co Prussian blue analogue: High-performance electrode materials for supercapacitors*. Journal of Electroanalytical Chemistry, 2019. **836**: p. 30-37.
- [161] Peng, S., et al., *Hollow nanospheres constructed by CoS₂ nanosheets with a nitrogen-doped-carbon coating for energy-storage and photocatalysis*. ChemSusChem, 2014. **7**(8): p. 2212-20.
- [162] Qiu, W., et al., *A self-standing and flexible electrode of yolk-shell CoS₂ spheres encapsulated with nitrogen-doped graphene for high-performance lithium-ion batteries*. Chemistry, 2015. **21**(11): p. 4359-67.
- [163] Lv, X., et al., *Hollow mesoporous NiCo₂O₄ nanocages as efficient electrocatalysts for oxygen evolution reaction*. Dalton Trans, 2015. **44**(9): p. 4148-54.
- [164] Hu, C., et al., *Synergism of Geometric Construction and Electronic Regulation: 3D Se-(NiCo)_{S_x}/(OH)_x Nanosheets for Highly Efficient Overall Water Splitting*. Adv Mater, 2018. **30**(12): p. e1705538.
- [165] Jervis, R., et al., *Hydrogen Oxidation on PdIr/C Catalysts in Alkaline Media*. Journal of The Electrochemical Society, 2014. **161**(4): p. F458-463.
- [166] Oh. S.M., *Electrochemistry*, FREEACADEMY, 2010, ISBN: 9788973388264 (오승모 저, 전기화학, 자유아카데미, 2010)
- [167] A.J. Bard and L.R.Faulkner, *Electrochemical methods: fundamentals and applications*, Wiley, 1980.
- [168] Dumesic, J. et al., *Handbook of heterogeneous catalysis*; Wiley: Wienheim, 2008, p1445.
- [169] G.K.Sweitzer and L.L. Pesterfield, *The Aqueous Chemistry of the Elements*, Oxford University Press, 2010.

- [170] Khalili. A., *Effective Boronizing Process for Age Hardening for Age Hardened Inconel 718*, The University of Western Ontario, Thesis for the degree in Master of Engineering Science, 2017.

요약(국문초록)

지난 수십 년 동안 화석 연료를 대체하고자 지속 가능한 에너지에 대한 연구가 지속적으로 증가하고 있으며, 그 중 수소는 가장 유망한 대체 에너지원 중 하나이다. 수소 생산을 위한 기술에는 다양한 방법이 있으나, 그 중 물분해는 수소 생산에 있어서 가장 유망한 기술 중 하나로 알려져 있다. 현재, 물분해를 위한 전기 촉매는 대개 백금, 이리듐과 같은 귀금속이 많이 사용되는데, 귀금속 계열의 비용 문제 등으로 인해 이를 비귀금속 기반의 전이 금속 화합물로 대체하고자 하는 연구가 보고되고 있다. 전이 금속 화합물은 귀금속과 비교하여 저렴한 비용과 귀금속과 비교할만한 성능 구현이 가능함에 따라 물분해 촉매 뿐만 아니라, 이산화탄소 환원, 질소 환원 촉매, 리튬-공기 전지 등과 같은 전기 화학 촉매 및 소자 시스템의 유망한 촉매 및 전극 물질 중 하나로 연구되고 있다. 그러나 전이 금속 화합물 기반 전기 촉매는 대량 생산을 위한 대규모 적용을 가능케 하기 위해서는 전기 촉매 성능의 개선이 여전히 필요하다. 수소 에너지 생성을 위한 물분해 시스템은 크게 산소 발생 반응과 수소 발생 반응 전기 촉매의 전극으로 구성되어 있다. 현재 수소 발생 반응과 비교할 때 산소 발생 반응은 많은 전자가 관여된 반응으로 인해 상대적으로 느린 반응 속도를 보이게 되고 이로 인해 물분해 성능 개선에 큰 방해가 되고 있다. 따라서, 산소 발생 반응은 전체 물분해 시스템의 성능을 개선하기 위한 주요 반응이라 볼 수 있다. 또한, 산소 발생 반응 조건 하에서 전이 금속 화합물 기반 전기 촉매의 제한된 전하 전달은 비효율적인 산소 발생 반응을 초래하고, 전기 촉매의 성능은 활성 부위의 노출 또는 변형 제어에 크게 의존한다.

본 학위논문의 목적은 효율적인 물분해를 위한 전이 금속 화합물 기반 전기 촉매의 구조적 설계에 관한 것으로, 열역학적으로 고려된 공정 조건과 정밀하게 제어된 활물질의 상 및 구조에 관한 전기 촉매 설계의 지침을 제공하는 것이다.

먼저 효율적인 산소 발생 반응을 위한 나노구조를 갖는 전기화학적 산화를 거친 이중 원소가 도핑된 니켈-철 층상 이중 수산화물 (NiFe LDH) 전기 촉매는 수열 합성과 이중 원소 도핑 과정, 열역학적으로 프로그래밍된 전기화학적 산화 공정을 통해 제작되었다. 이중 원소인 붕소 도핑의 목적은 NiFe LDH의 상대적으로 열악한 전하 전달과 낮은 전도성을 극복하고 이로 인한 촉매 활성을 높이는 것이다. 지금까지 붕소 도핑 혹은 전이 금속 붕화물 형성을 위한 붕소화 과정은 붕소 자체의 높은 비점과 용점으로 인해 제한되어 고온을 초래했다. 따라서, 본 연구에서 진행된 붕소화 과정은 붕소가 아닌 붕소 기반 전구체를 공급원으로 사용하여 기상 상태의 붕소화를 비교적 낮은 온도에서 진행하였으며, 이는 보다 간단한 공정으로, 붕소 도핑된 NiFe LDH를 제조하여 전하 전달 저항이 개선된 높은 산소 발생 반응 성능을 달성하였다. 또한, 활성화 과정을 통한 붕소 도핑된 NiFe LDH는 전기화학적 산화 과정을 통해 붕소 도핑된 NiFe LDH 내의 옥시수산화물의 비율을 성공적으로 증가시켰다. 이러한 전기화학적 산화 과정을 거친 붕소 도핑된 NiFe LDH는 도핑된 붕소로 인해 활성 부위를 개선시킨다고 알려져 있다. 본 연구에서 제조된 전기화학적 산화 과정을 거친 붕소 도핑된 NiFe LDH는 10 mA cm^{-2} 의 전류 밀도에 도달하기 위해 229 mV 의 우수한 산소 발생 반응 성능을 필요로 하며, 이는 같은 조건에서 귀금속인 이리듐보다 약 140 mV 낮고, 공정 과정을 거치지 않은 NiFe LDH보다 86 mV 낮은 것을 확인하였다.

다음으로, 산소 및 수소 발생 반응이 모두 가능하고 효율적인 전체 물분해를 위한 상이 제어된 계층적 다공성 구조를 가진 코발트 황화물 기반 전기 촉매를 개발하였다. 코발트 황화물은 다양한 상을 갖지만, 열역학 계산에 기초한 예측 합성을 통한 황의 비율에 따라 코발트 황화물의 상을 성공적으로 제어하였다. 활성 부위의 노출을 위한 고 다공성 코발트 이황화물 (CoS_2) 나노 입자는 적절한 양의 황과 금속-유기 골격체 중 하나인 코발트 프러시안 블루 아날로그의 비를 제어함으로써 합성되었다. 새롭게 설계된 금속-유기 골격체 기반 CoS_2 전기 촉매는 약 4 nm 의 나

노기공을 갖는 다공성 구조이며, 약 30 nm의 크기의 균일한 입자 크기를 갖는 것을 확인하였다. 이러한 구조로 인해 $915.6 \text{ m}^2 \text{ g}^{-1}$ 의 넓은 비표면적을 갖게 되고, 활성 부위의 노출도를 높일 수 있었다. 따라서, 합성된 전기 촉매는 효율적인 산소 및 수소 발생 반응 성능을 10 mA cm^{-2} 의 전류 밀도에서 각각 298 mV, -196 mV의 낮은 과전압을 통해 확인했으며, 지속적인 가스 발생에도 불구하고, 10 mA cm^{-2} 에서 안정적인 산소 및 수소 발생 반응을 나타냈다. 이러한 우수한 활성은 실제 상용화에 가까운 2전극의 전체 셀 시스템에서 2기능성 전기 촉매 특성을 통해 10 mA cm^{-2} 전류 밀도에서 1.65 V의 과전압을 나타내는 것으로 확인하였다.

본 연구는 전이 금속 화합물의 상과 구조를 열역학적으로 정밀하게 제어하는 방법론을 이해하는 데에 유용한 정보를 제공할 수 있으며, 물분해를 위한 전이 금속 화합물 기반 전기 촉매의 성능을 향상시키는 다양한 설계 및 방법론에 대해 제공한다.

표제어: 물분해, 수전해, 전이금속 화합물, 니켈-철 층상이중수산화물, 금속-유기 골격체, 코발트 이황화물, 열역학 계산, 상 제어

학 번: 2014-22522

CURRICULUM VITAE

In-Kyoung Ahn

EDUCATION

- 2014 ~2020 **Seoul National University, South Korea**
Seoul, Korea
Integrated course of master's and the doctor's
Department of Materials Science and Engineering
Research on structural design of transition metal compounds based
electrocatalysts for water splitting
Advisor: Young-Chang Joo, Professor
- 2009~2013 **Yonsei University, South Korea** Seoul, Korea
B.S., Department of Materials science and Engineering

RESEARCH EXPERIENCES

- **Department of Materials Science and Engineering, Seoul National University**
Advisor: Young-Chang Joo
- ✓ Electrochemical properties of transition metal compounds based electrocatalyst
 - Investigation of electrocatalytic activity and stability of cathode and anode for water splitting

- Electrochemical impedance spectroscopy for identification of equivalent circuit model, such as charge transfer resistance, of electrocatalysts
- Investigation of gas chromatography to analyze the gas product
- ✓ Electrochemical properties of silicon based electrodes
 - Identification of charge and mass transport in electrodes for Li-ion batteries
 - Development of particle coating method for enhancing the performance of anode materials
 - Sputtering process for the electrode design
 - Interfacial engineering method
 - Theoretical analysis on the lithiation mechanism in silicon based electrodes
- ✓ Synthesis of nanostructured transition metal compound based electrocatalysts
 - Electrospinning process for cobalt compound
 - Hydrothermal process for transition metal LDH
 - Optimization of activity by controlling the ratio of metal precursor
 - Precipitation process for metal-organic framework
 - Uniform distribution of nanoparticle size
 - Combination of transition metal
- ✓ Designing the formation of transition metal compounds through thermal treatment
 - Thermodynamic calculation for each condition of transition metal sulfide
 - Product prediction through calculation of Gibbs free energy
 - Current density control for electrochemical oxidation through Pourbaix diagram

AWARDS AND HONORS

December 2017 **Outstanding Presentation award,**

2017 International Conference on Engineering Innovation, 2017. 12. 8.,
Seoul National University, Korea

PROFESSIONAL ACTIVITIES

Sept. 2017 ~ Aug. 2020 **Mandatory Military Service**

Technical Research Personnel

PUBLICATIONS

- **In-Kyoung Ahn**, Young-Joo Lee, Sekwon Na, So-Yeon Lee, Dae-Hyun Nam, Ji-Hoon Lee*, and Young-Chang Joo*, “Improved Battery Performance of Nanocrystalline Si Anodes Utilized by Radio Frequency (RF) Sputtered Multifunctional Amorphous Si Coating Layers”, *ACS Applied Materials & Interfaces*, **10**, (2018)
- **In-Kyoung Ahn**, Wonhyo Joo, Ji-Hoon Lee, Hyoung Gyun Kim, So-Yeon Lee, Youngran Jung, Ji-Yong Kim, Gi-Baek Lee, Miyoung Kim, and Young-Chang Joo*, “Metal-organic Framework-driven Porous Cobalt Disulfide Nanoparticles Fabricated by Gaseous Sulfurization as Bifunctional Electrocatalysts for Overall Water Splitting”, *Scientific Reports*, **9**, 19539, (2019)
- **In-Kyoung Ahn**, So-Yeon Lee, Hyoung Gyun Kim, Miyoung Kim, and Young-Chang Joo*, “Electrochemical Oxidation of Boron-Doped Nickel-

Iron Layered Double Hydroxide for Facile Charge Transfer in Oxygen Evolution Electrocatalysts”, *in preparation*

- **In-Kyoung Ahn**[†], Deokgi Hong[†], Gun-Do Lee*, and Young-Chang Joo*, “Electrochemical Oxidized Nickel Iron Boride Nanostructure as Efficient Oxygen Evolution Electrocatalysts”, *in preparation*
- Ji-Yong Kim, Hwanyeol Park, Wonhyo Joo, Dae-Hyun Nam, Sungwoo Lee, Hyoung Gyun Kim, **In-Kyoung Ahn**, Ho-Young Kang, Gi-Baek Lee, In-ho Jung, Mi-Young Kim, Gun-Do Lee and Young-Chang Joo*, “Predictive fabrication of Ni phosphide embedded in carbon nanofibers as active and stable electrocatalysts”, *Journal of Materials Chemistry A*, **7**, (2019)
- Dae-Hyun Nam, Ho-Young Kang, Jun-Hyun Jo, Byung Kyu Kim, Sekwon Na, Uk Sim, **In-Kyoung Ahn**, Kyung-Woo Yi, Ki Tae Nam, and Young-Chang Joo, “Controlled Molybdenum Disulfide Assembly inside Carbon Nanofiber by Boudouard Reaction Inspired Selective Carbon Oxidation”, *Advanced Materials*, 1605327, (2017)
- Dae-Hyun Nam¹, Ji-Yong Kim¹, Sungwoo Kang¹, Wonhyo Joo, Seung-Yong Lee, Hongmin Seo, Hyoung Gyun Kim, **In-Kyoung Ahn**, Gi-Baek Lee, Minjeong Choi, Eunsoo Cho, Miyoung Kim, Ki Tae Nam, Seungwu Han, and Young-Chang Joo*, “Anion Extraction-Induced Polymorph Control of Transition Metal Dichalcogenides”, *Nano Letters*, **19**, (2019)

PRESENTATIONS IN INTERNATIONAL CONFERENCES

Oral Presentations

- **In-Kyoung Ahn**, Ji-Hoon Lee, Sekwon Na, Dae-Hyun Nam, Ho-Young Kang, and Young-Chang Joo*, “A Core/Shell Structure of Crystalline/Amorphous Si Fabricated by RF Sputtering for Enabling Mass Production as Anodes of High Cycling Retention Li-ion batteries”, Materials Research Society (2016 MRS spring meeting), Phoenix, AZ, USA.
- **In-Kyoung Ahn**, Ji-Hoon Lee, Sekwon Na, Dae-Hyun Nam, Ho-Young Kang, and Young-Chang Joo*, “A Core/Shell Structure of Crystalline/Amorphous Si Fabricated by RF Sputtering for Enabling Mass Production as Anodes of High Cycling Retention Li-ion batteries”, *NANO KOREA 2016 Symposium*, Ilsan, Korea
- **In-Kyoung Ahn**, Young-Joo Lee, Sekwon Na, So-Yeon Lee, Dae-Hyun Nam, Ji-Hoon Lee*, and Young-Chang Joo*, “Hierarchically-designed Amorphous Si Layer on Nano-crystalline Si Particle of Homo-structure for Mass production of Advanced Li-ion Batteries”, *International Conference on Engineering Innovation 2017*, Seoul, Korea
- **In-Kyoung Ahn**, Wonhyo Joo, Ho-Young Kang, Gi-Baek Lee, Ji-Yong Kim, and Young-Chang Joo*, “Porous Cobalt Disulfide Nanoparticles through Metal-Organic Frameworks as Efficient Electrocatalysts for Overall Water Splitting”, International Conference Electronic Materials and Nanotechnology for Green Environment (*ENGE 2018*), Jeju, Korea

Poster Presentations

- **In-Kyoung Ahn**, Young-Joo Lee, Sekwon Na, So-Yeon Lee, Dae-Hyun Nam, Ji-Hoon Lee*, and Young-Chang Joo*, “Improved Battery Performance of Nanocrystalline Si Anode Utilized by Radio Frequency Sputtered Multifunctional Amorphous Si Coating Layers”, *Kinetic Phenomena and Nanoscale Materials* (2018), Seoul, Korea

PATENT

- **In-Kyoung Ahn**, Minisha Mehta, Sung-gyu Kang, Heung Nam Han, In-Suk Choi, and Young-Chang Joo, “METHOD OF FORMING MICROSTRUCTURE AND NANOSTRUCTURE USING METAL ASSISTED CHEMICAL ETCHING”, Korea patent (1020180165955)
- **In-Kyoung Ahn**, and Young-Chang Joo, “Method for manufacturing transition metal sulfide using Metal Organic Frameworks and porous transition metal sulfide manufactured thereby”, Korea patent (1020190110221)
- **In-Kyoung Ahn**, and Young-Chang Joo, “Method for manufacturing cobalt sulfide with sulfur vacancy defect and cobalt sulfide manufactured thereby”, Korea patent (1020190126879)

R & D PROJECTS

- “Development of multi-dimensional and multi-phase programmed metal compounds / carbon materials through nano metallurgy”, Creative Materials Discovery Program funded by Ministry of Science and ICT (MSIT, KOREA), 2017. 9. ~ 2020. 8.
- “Strategy of Materials Research for Sustainable Future”, funded by Ministry of Science, ICT and Future Planning (KOREA), 2015. 12. ~ 2016. 1.
- “Development of highly reliable electrode materials for the implementation of next-generation cross-point memory devices”, funded by SAMSUNG ELECTRONICS (KOREA), 2017. 9. ~ 2020. 06.
- “Research on highly reliable Cu interconnects for next-generation logic devices under 10 nm”, funded by SAMSUNG ELECTRONICS (KOREA), 2014. 09. ~ 2017. 09.
- “Ionic biotransistor based on hydrogel”, funded by SAMSUNG ELECTRONICS (KOREA), 2014. 12. ~ 2018. 11.
- “Development of non-toxic nanoparticles of core-shell structure”, funded by Korea Research Institute of Standards and Science (KRISS, KOREA), 2016. 2. ~ 2018. 1.